Università degli Studi di Genova

FACOLTÁ DI SCIENZE MATEMATICHE FISICHE E NATURALI

DIpartimento Per lo studio del TErritorio e delle sue RISorse (DIPTERIS) - Dottorato di Ricerca Geofisica, XV ciclo

Aerosol extinction coefficient profile retrieval procedure for satellite measurements in multiple scattering atmosphere

Stefano Corradini

Relatori:
Prof. **Renato Santangelo**
Prof. **Rodolfo Guzzi**

Correlatore:
Dott. **Walter Di Nicolantonio**

Bologna, Marzo 2004

Contents

1 Introduction **11**

1.1 Aerosol Influence in Earth Radiation Budget 13

1.2 The Aerosol Profile Retrieval Problem 15

1.2.1 State of the Art for Aerosol Profile Retrieval 18

1.3 Aim of the thesis 21

1.4 Organization of dissertation 23

2 SCIAMACHY **25**

2.1 SCanning Imaging Absorption spectroMeter for Atmospheric CartograpHY - SCIAMACHY 25

2.2 Atmospheric windows wavelengths selection for SCIAMACHY spectral range 30

3 LInearized Discrete Ordinate Radiative Transfer (LIDORT) **35**

3.1 Introduction 35

3.2 Outline of Radiative Transfer Equation (RTE) solution in UV-VIS-NIR spectral range 37

3.2.1 Summarizing of Intensity computation user input . . . 43

3.3 *weighting function* computation 44

3.3.1 Consideration on the *Parameter Normalized Weighting Functions* and *aerosol extinction coefficient* 46

3.4 Principal corrections for the accuracy improvements 46

3.4.1 Delta-N method 46

3.4.2 Nakajima-Tanaka procedure 48

4 The Optimal Estimation inversion technique 49

4.1 Introduction to the Optimal Estimation inversion theory . . . 49

4.2 The Inverse Problem 50

4.2.1 State and Measurements vectors 50

4.2.2 Forward Model and Linearization 51

4.2.3 Statistical description of experimental errors 52

4.3 Error analysis 55

4.3.1 Retrieval noise 55

4.3.2 Smoothing Error 56

4.3.3 Forward Model Parameter Error 57

4.3.4 Forward Model Error 58

4.4 Measurement Information theory 58

4.4.1 Degrees of freedom 58

4.4.2 Shannon information content 59

4.5 Inversion iterative Method 60

4.5.1 Gauss-Newton Method 60

5 Forward Model development, validation and inversion procedure implementation 63

5.1 AerLIDORT Atmospheric Optical Properties 63

5.1.1 Molecules 64

5.1.2 Aerosol 69

5.1.3 Surface Albedo 72

5.1.4 AerLIDORT implementation subroutines 72

5.1.5 Input for Weighting Function computation 74

5.2 AerLIDORT Validation 78

5.2.1 SCIATRAN RTM 79

5.2.2 Characteristics of simulations for TOA Intensity and Weighting Functions validations 79

5.3 Implementation of iterative inversion procedure 90

6 Test case: SCIAMACHY nadir measurements. Setting Parameters **93**

6.1 Input for Optimal Estimation inversion procedure and Error Assessment . . . 93

6.1.1 *State Vector* and *A-priori correlation* matrix . . . 93

6.1.2 *Measurement Vector* and *Measurement correlation* matrix . . . 98

6.1.3 Forward model parameters error (S_b) setting . . . 99

6.1.4 Forward model error setting . . . 102

6.2 Sensitivity Study . . . 102

6.3 Characteristics of simulations . . . 103

7 Test case: SCIAMACHY nadir measurements. *Aerosol extinction coefficient* profile retrieval Atmospheric windows wavelengths and Oxygen A-band comparison **105**

7.1 A-priori analysis . . . 105

7.1.1 *Maritime* test . . . 105

7.1.2 *Desertic* test . . . 108

7.1.3 Information content of higher spectral resolution in the Oxygen A-band . . . 110

7.1.4 A-priori analysis using both atmospheric windows and Oxygen A-band wavelengths . . . 111

7.2 *Maritime* and *Desertic* test retrieval for Oxygen A-band . . . 113

7.3 Sensitivity and error assessment in Oxygen A-band for *maritime* test . . . 114

7.3.1 Solar Zenith Angle and Surface albedo sensitivity . . . 115

7.3.2 Forward Model errors and Forward Model parameters errors . . . 116

8 Conclusion **121**

8.1 Problem and Procedure 121
8.2 Results 122
8.3 Outlook and future work 126

References **126**

Acknowledgements **141**

List of Figures

1.1 Schematic representation of the Earth energy balance. 14

1.2 Estimated magnitudes and uncertainties of different contributions to radiative forcing of climate [source: *IPCC 2001*]. The level of scientific understanding is only qualitative: H=high, L=Low, VL=Very Low.. 16

1.3 Cloudy sky TOA and surface diurnally averaged shortwave dust forcind as a function of surface albedo r_s for different assumed dust layer altitudes. [*Liao and Seinfeld, 1998*] 17

1.4 Top: altitude from which the majority of the backscattered radiance is coming considering the GOME spectral resolution [Koppers et al., 1998]. White = maximum backscattering, black = null backscattering. Bottom: oxygen A-band simulated TOA reflectance at GOME spectral resolution 19

2.1 GOME and SCIAMACHY spectral range and atmospheric species detected. 26

2.2 Nadir view of SCIAMACHY. [graphics by *S. Noël*] 27

2.3 Occultations view of SCIAMACHY. [graphics by *S. Noël*] 28

2.4 Limb view of SCIAMACHY. [graphics by *S. Noël*] 29

2.5 Limb-Nadir measurements matching view of SCIAMACHY. [graphics by *S. Noël*] 30

2.6 Left plate: simulated SCIAMACHY TOA reflectance spectra with and without gas absorption for SCIAMACHY channels 2. Right plate: percentage TOA reflectance difference between spectra with and without gas absorption in atmospheric window in channels 2 and wavelengths selection. 32

2.7 Left plate: simulated SCIAMACHY TOA reflectance spectra with and without gas absorption for SCIAMACHY channels 3. Right plate: percentage TOA reflectance difference between spectra with and without gas absorption in atmospheric window in channel 3 and wavelengths selection. 32

2.8 Top plate: simulated SCIAMACHY TOA reflectance spectra with and without gas absorption for SCIAMACHY channels 4. Bottom plates: percentage TOA reflectance difference between spectra with and without gas absorption in atmospheric window in channel 4 and wavelengths selection. 33

2.9 Left plate: simulated SCIAMACHY TOA reflectance spectra with and without gas absorption for SCIAMACHY channels 5. Right plate: percentage TOA reflectance difference between spectra with and without gas absorption in atmospheric window in channel 5 and wavelengths selection. 33

2.10 Top left plate: simulated SCIAMACHY TOA reflectance spectra with and without gas absorption in atmospheric window in channel 6. Top right plate and bottom plates: percentage TOA reflectance difference between spectra with and without gas absorption in atmospheric window in channel 6 and wavelengths selection. 34

5.1 Comparison between Mie phase functions for different aerosol classes, at 500 nm. 70

5.2 Comparison between Mie phase function and Henyey-Greenstein phase function, for maritime aerosol at 500 nm; in figure is also shown the scattering angle range for nadir sounding (100 - 180 degrees). 71

5.3 Spectral albedo for different surfaces (CADAPA reference). 73

5.4 Spectral albedo for different surfaces in the oxygen $A-band$ spectral range. 74

5.5 SCIAMACHY slit functions around 762 nm. 75

5.6 Standard MODTRAN aerosol extinction coefficient profile at 550 nm (surface visibility = 23 km, AOT = 0.3315). 81

5.7 SCIATRAN TOA reflectance spectra and AerLIDORT reflectance for selected wavelengths in atmospheric windows. 82

5.8 TOA Reflectance for oxygen $a-band$; spectral resolution = 0.05 nm. 83

5.9 TOA Reflectance for oxygen $a-band$; convolution with SCIAMACHY slit function. 84

5.10 Percentage relative differences and histogram of the relative differences between SCIATRAN and AerLIDORT TOA Reflectance, considering a spectral resolution of 0.05 nm. 85

5.11 Percentage relative differences and histogram of the relative differences between SCIATRAN and AerLIDORT TOA Reflectance convoluted with SCIAMACHY slit function. 86

5.12 *weighting functions* computed by AerLIDORT for different atmospheric parameters. 88

5.13 550 nm phase function before and after the Legendre Polynomials perturbation. 89

5.14 Inversion iterative procedure scheme. 90

6.1 June, July and August (JJA) mean aerosol extinction coefficient profiles and percentage standard deviation for cloudless atmosphere in no-cirrus (NC) and Saharan dust (SD) conditions [*Gobbi et al., 2003*]. 96

6.2 Aerosol extinction coefficient profile parametrization for *maritime case* and *desertic case*. 97

6.3 Aerosol extinction coefficient profile standard deviation parametrization for textitmaritime case and *desertic case*. 98

6.4 True *Aerosol extinction coefficient* profiles for *maritime* and *desert* cases. 98

6.5 Percentage relative standard deviation for P, T and Rayleigh scattering. 101

7.1 *Weighting functions*, *averaging kernels* and *retrieval error* for atmospheric windows and oxygen A-band *maritime* case retrieval. The averaging kernel curves are labeled with the middle layers altitude in kilometers. 107

7.2 A-priori profile weighting function and averaging kernel for *desertic* test retrieval, using atmospheric windows and oxygen wavelengths. The averaging kernel curves are labeled with the middle layers altitude in kilometers. 109

7.3 Aerosol single scattering albedo for the *maritime* and *desertic* classes in UV-VIS-NIR spectral range and focused into oxygen A-band. 110

7.4 Weighting functions, averaging kernels and retrieval error for 0.05nm spectral resolution in oxygen A-band for *maritime* and *desertic* tests. The averaging kernel curves are labeled with the middle layers altitude in kilometers. 112

7.5 Aerosol extinction coefficient profile retrieval for *maritime* and *desertic* tests in oxygen A-band. 113

7.6 TOA reflectance retrieved for *maritime* and *desertic* test in oxygen A-band. 114
7.7 Degrees of freedom and Entropy variation varying the solar zenith angle, for *maritime* test in oxygen A-band. The averaging kernel curves are labeled with the middle layers altitude in kilometers. . . 115
7.8 Averaging kernels considering Sea and Vegetation surface. 116
7.9 Forward model errors on aerosol extinction coefficient profile accuracy (the left picture is the same as right and has been plotted to evidentiate the errors induced by 6, 8 and 12 stream approximations). 117
7.10 Forward model parameters error on aerosol extinction coefficient profile accuracy 118
7.11 Mie and Henyey-Greenstein phase functions plotted in satellite nadir viewing scattering angles range. 119

Chapter 1

Introduction

Atmospheric aerosols affect the Earth radiation balance by scattering and absorbing solar radiation (direct effect), and by modifying the micro-physical properties of clouds (indirect effect). Many authors have analyzed the influence of aerosol on the radiative balance [among them *Charlson and Heintzeberg, 1995; Haywood and Shine, 1995; Russell and Heintzenberg, 2000; Haywood and Boucher, 2000*]. The interaction between aerosols and incoming solar radiation may explain the differences between satellite observed and model-simulated clear-sky albedo [*Haywood et al. 1999*]. The radiative forcing induced by direct and indirect aerosol effects is one of the largest uncertainties still open in climate studies [*IPCC, 2001*]. Moreover, aerosol loading has high spatial and temporal variability. To better understand and reduce the uncertainties due to aerosols we need to study aerosol optical properties, aerosol loading, aerosol vertical distribution and their variability over the globe. Such uncountable has to come from different instruments, hopefully covering a time range as large as possible. The retrieval of global distribution of aerosol optical properties, its variation and seasonal trends, can be achieved only by using satellite measurements. However, satellite aerosol retrieval requires a very careful separation of weak aerosol signals from disturbing effects associated with radiometric and calibration errors of sensor, inaccurate assumptions on the retrieval algorithm, atmospheric gas absorption, surface reflectance effect and cloud contamination.

Many "passive" satellite instruments (that are instruments that collects the radiation backscattered or emitted from the atmosphere and ground) has been used to retrieve the aerosol optical properties i.e. the Advanced Very High Resolution Radiometer (AVHRR) [*Mishenko et al., 1999*], Total Ozone Mapping Spectrometer (TOMS) [Torres et al., 1998, 2002], MODerate resolution Imaging Spectroradiometer (MODIS) [Martonchik et al., 1997, 2002; Kaufman et al., 1997], Multi-angle Imaging SpectroRadiometer (MISR) [*Diner et al. 2002*] and Global Ozone Monitoring Experiment (GOME) [*Burrows et al.,1997; Torricella et al., 1999*] for global aerosol mapping and the Stratospheric Aerosol and Gas Experiment (SAGE I, II and III) [*Ackerman et al., 1989; Thomason et al., 2003; Bingen et al., 2004 (1) and (2)*] for stratospheric aerosol profile detection. Also a new generation of "active" systems based on Lidar technology (the retrieval is caring out analyzing the backscattering radiation induced by a laser impulse shoot in the atmosphere) will provide a global set of aerosol data including the atmospheric profile (see for example CALIPSO [*http://www-calipso.larc.nasa.gov*] and Earthcare [*http://www.esa.int*] experiments).

Ground-based measurements are strongly request to improve and validate the satellite aerosol retrieval. Recently many comprehensive regional experiments in clean and polluted environments has been done [*Kaufman et al. 1998, Gobbi et al., 2000, 2003; Di Sarra, 2001; Ramanathan et al. 2001 (2)*] and AERONET network has been created. The AErosol RObotoc NETwork (AERONET, *http://aeronet.gsfc.nasa.gov; Holben et al., 2001*) is a federation of ground based sun-photometers; the network goal is to provide globally distributed observations of aerosol optical properties in geographically different aerosol regimes.

The retrieval methods for "passive" systems, developed to obtain an aerosol characterization, are based on relationships existing between the upwelling visible and near-infrared radiances and the Aerosol Optical Thickness (AOT) over low albedo surface (typically oceans) for different aerosol type and as-

sumed vertical distribution. Earlier monospectral methods based on single wavelength measurements were soon superseded by multi-channel algorithms. The rationale for the multi-channel approach is that each channel contains some unique information about the scattering process in the atmosphere. Multi-spectral algorithms use inter-relationships between radiance measured in different spectral channels. Connections between radiances at different wavelengths are established when the radiative properties of aerosol and molecules and the reflectance properties of the underlying surface are prescribed. In any practical application using measured radiances, this information may not be available and thus the application result of the method will yield radiatively equivalent quantities. Typically over land surfaces the aerosol retrieval is performed with less accuracy. In case of particular land surface (for example sand or snow), the surface reflectance in the visible spectral range gives the aerosols retrieval very critical because the surface spectral signature overlaps the aerosol spectral signature. Some exercises have been proposed by different authors [*King et al., 1999, Martonchiket al. 1997, Kaufman et al. 1997, Von Hoyningen Huene et al. 2003*]. Up to now aerosol operational retrieval has been made with good accuracy over sea water that is black beyond the red wavelengths while it has a small but not negligible reflectance in the visible where the reflectance increases in the presence of sea roughness and white-caps.

1.1 Aerosol Influence in Earth Radiation Budget

During the last century, the Earth surface temperature increases of 0.6 degrees, reaching the highest level in the millennium [*IPCC 2001*]. This rapid temperature change is attribute to a shift of less than 1% [*Ramanathan, 2001 (1)*] in the energy balance between absorption and reflection of incoming solar radiation and emission of thermal radiation from the Earth system. Figure (1.1) shows a schematic representation of the radiation balance of the

Earth-atmosphere system.

Among the different agents of climate change, anthropogenic greenhouse

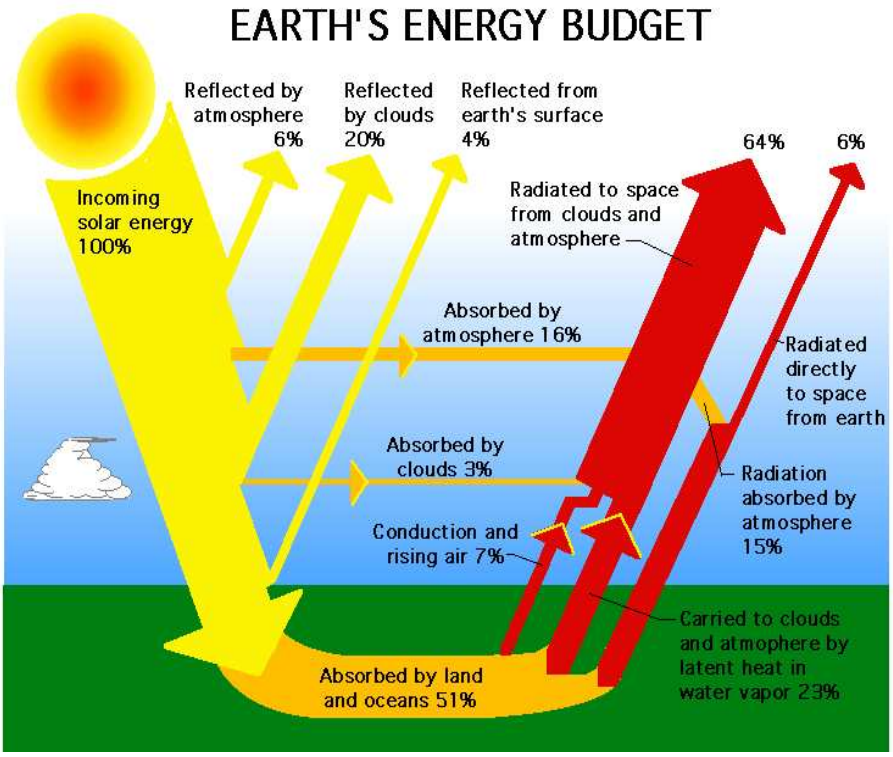

Figure 1.1: Schematic representation of the Earth energy balance.

gases and aerosols have the larger roles [*IPCC 2001*]. Whereas greenhouse gases reduce the emission of thermal radiation to space, thereby warming the surface, aerosol mainly reflect and absorb solar radiation (direct effect) and modify cloud properties (indirect effect), cooling the surface [*King et al 1999, Kaufman et al. 2002*]. Greenhouse gases, such as carbon dioxide and methane, have a lifetime which is up to 100 years in the atmosphere and a rather homogeneous distribution around the globe; this is in contrast to the heterogeneous spatial and temporal distribution of tropospheric aerosols [*IPCC 2001, Ramanathan 2001, Andrae 1986*]. In fact the aerosols lifetime in the atmosphere is at most of a few days, heterogeneous patterns of radiative forcing are generated, with large variations in optical thickness and radiative forcing of the order of tens of Watts per square meter on a regional

scale [*Christopher et al., 1996*]. These variations give rise to the 12 Wm^{-2} forcing on a global scale.

The effect of greenhouse gases on the energy budget occurs everywhere around the globe. Aerosols have both regional and global impacts on the energy budget, requiring frequent global measurements tried to elaborate models that provide realistic representations of the atmospheric aerosols [*Andrae 1986, Charlson 1992, Kiehl 1993*]. In the future, the greenhouse gas warming is expected to dominate due to the much longer presence of gases in the atmosphere ($10 - 100$ years) than that of aerosol particles (7 days).

As Figure (1.2) shows, until now, aerosols represent one of the greatest areas of uncertainty regarding climate change, both on global and regional scales. Scientists don't fully understand the magnitude of their influence on climate and which, of the emission products, exerts the greater net effect on regional and global climate: the mainly cooling influence of aerosols and clouds, or the warming influence of the greenhouse gases. Because both types of emission products change rapidly through time and space, they are difficult to observe and characterize.

Aerosol effects on climate differ from those of greenhouse gases in two additional ways. Because most aerosols are highly reflective, they raise our planet albedo, thereby cooling the surface and effectively offsetting greenhouse gas warming anywhere from 25 to 50%. However, aerosols containing black graphitic and tarry carbon particles (present in smoke and urban haze) are dark and therefore strongly absorb incoming sunlight. The effects of this type of aerosols are twofold, both warming the atmosphere and cooling the surface before a redistribution of the energy occurs in the column.

1.2 The Aerosol Profile Retrieval Problem

The problem of the aerosol influence magnitude on climate is further complicated by the aerosol altitude distribution.

With the exception of large volcanic eruption, capable to inject aerosol into

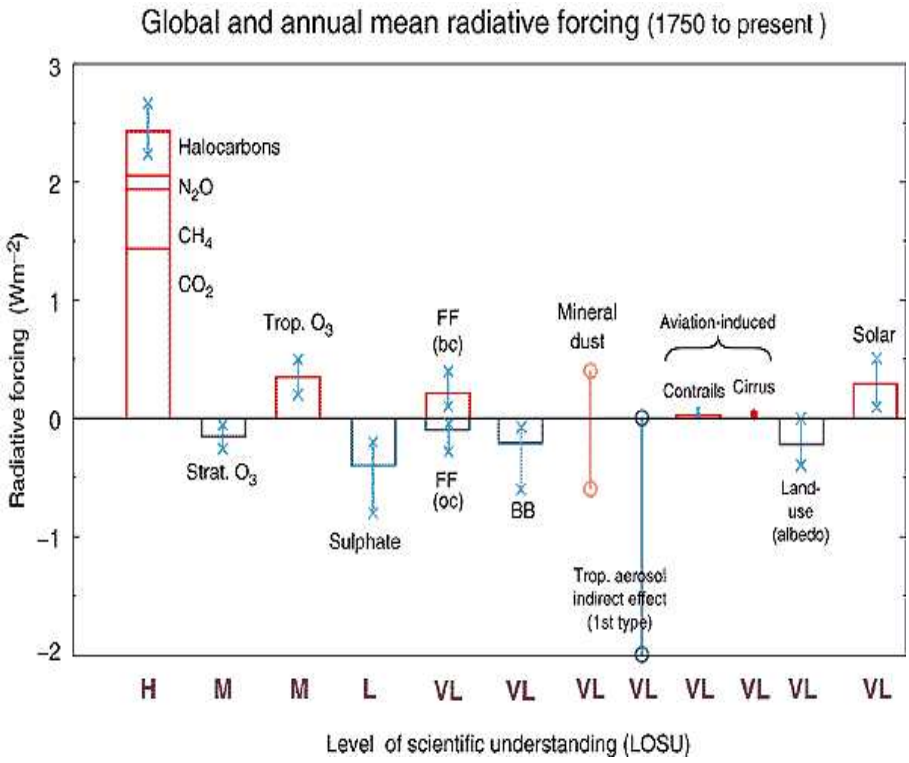

Figure 1.2: Estimated magnitudes and uncertainties of different contributions to radiative forcing of climate [source: *IPCC 2001*]. The level of scientific understanding is only qualitative: H=high, L=Low, VL=Very Low..

the stratosphere [see *Hansen at al., 1992*], the aerosol effects take place mainly within and above the planetary boundary layer (PBL). The PBL is the region where the most of the atmospheric aerosol is located [e.g. *Jaenicke, 1992*]. At the same time, it is well established that large amounts of mineral dust from arid regions of the Earth [e.g. *Prospero et al., 2000; Gobbi et al., 2000; Sassen, 2002*] and transported over thousands of kilometers [e.g. *Duce et al., 1980; Prospero et al., 1983; Moulin et al., 1998*]. Different authors has been shown that its presence in the atmosphere can either lead to a cooling or warming effect, depending on properties on single scattering albedo, altitude of the layer and surface albedo. In fact, when reaching the middle and upper troposphere, the desert dust leads to a warming on the planet, i.e. it has an opposite effect with respect to non-absorbing aerosol (see Figure (1.3)) [e.g. *Hansen et al., 1997; Liao and Seinfeld, 1998*]. Such a variable

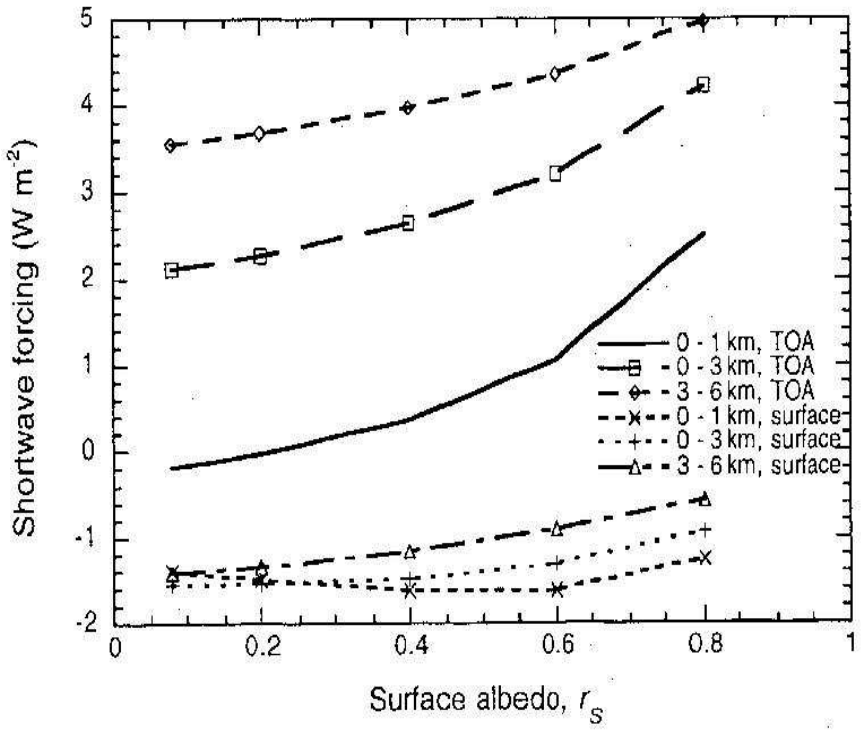

Figure 1.3: Cloudy sky TOA and surface diurnally averaged shortwave dust forcind as a function of surface albedo r_s for different assumed dust layer altitudes. [*Liao and Seinfeld, 1998*]

height-dependent distribution explains why a large part of the indetermination in forecasting the aerosol radiative impacts derives from differences in the aerosol vertical profile employed in models [e.g. *Perner et al., 2001*]. Desert dust particle, for example, represent a large fraction (of order $30 - 50\%$) of the naturally occurring tropospheric aerosol, seconds only to maritime ones [e.g. *Charlson and Heintzenberg, 1995*]. Knowledge of the altitude properties of desert dust aerosol is rather poor and this lack of knowledge represent a major uncertainty in determining the effects that these particle have on climate.

Determining the altitude distribution of aerosol is also very important in all studies concerning the heterogeneous processing of gases in the atmosphere. The knowledge of vertically resolved aerosol properties is of interest in the field of passive satellite radiometry for trace gas detection. In this case the

vertical distribution of the aerosol particles is known to strongly influence the accuracy of retrieved trace gases [e.g. *Spurr, 2000*].

Until now the our knowledge about height-resolved aerosol properties over long-term periods is still rather poor. Data is mostly limited to localized observations [e.g. *Hofman, 1993; Balis et al., 2000, Sakai at al., 2000; Schneider and Eixmann, 2002; De Tomasi and Perrone, 2003*]. More of the observations refer to limited portion of the troposphere [e.g. *Kent et al., 1991; Matthias and Bosenberg, 2002; Del Guasta, 2002*] or to case studies [e.g. *Grasso et al., 2000; Murayama et al., 2001; Muller et al., 2003*]. Moreover the "active" satellite systems, based on Lidar technology, as CALIPSO and Eartcare are not nowadays operational.

1.2.1 State of the Art for Aerosol Profile Retrieval

The retrieval of aerosol profile is a difficult problem to solve for two main reasons: the lack of the narrow absorbing signature spectrum (as for molecular species) and the technical difficulties that results from the nonlinear relationship between the observable parameter (i.e. the TOA intensity) and the unknown quantity (i.e. the aerosol vertical profile).

The aerosol profile retrieval has been faced both using the so-called atmospheric windows and oxygen A-band wavelengths.

The atmospheric windows wavelengths are generally used for the aerosol retrieval to avoid the molecular influence; in this case a wide spectral range is needed to take advantage of the different optical properties at different wavelengths.

Oxygen A-band absorption ranges from zero to saturation, as function of wavelength and spectral resolution of measurements. As consequence, at the middle of the band, where the absorption is high, the reflected signal that reaches the satellite originates only from the upper part of the atmosphere, whereas at other wavelengths the role of reflection from lower layers in the signal becomes increasingly more pronounced with the decrease of absorption

coefficient. The top and bottom plate of Figure (1.4) show respectively the altitude from which the most of backscattering radiance is coming at satellite, considering GOME spectral resolution (about 0.2 nm), and the oxygen A-band reflectance spectrum at the same spectral resolution. The maximum

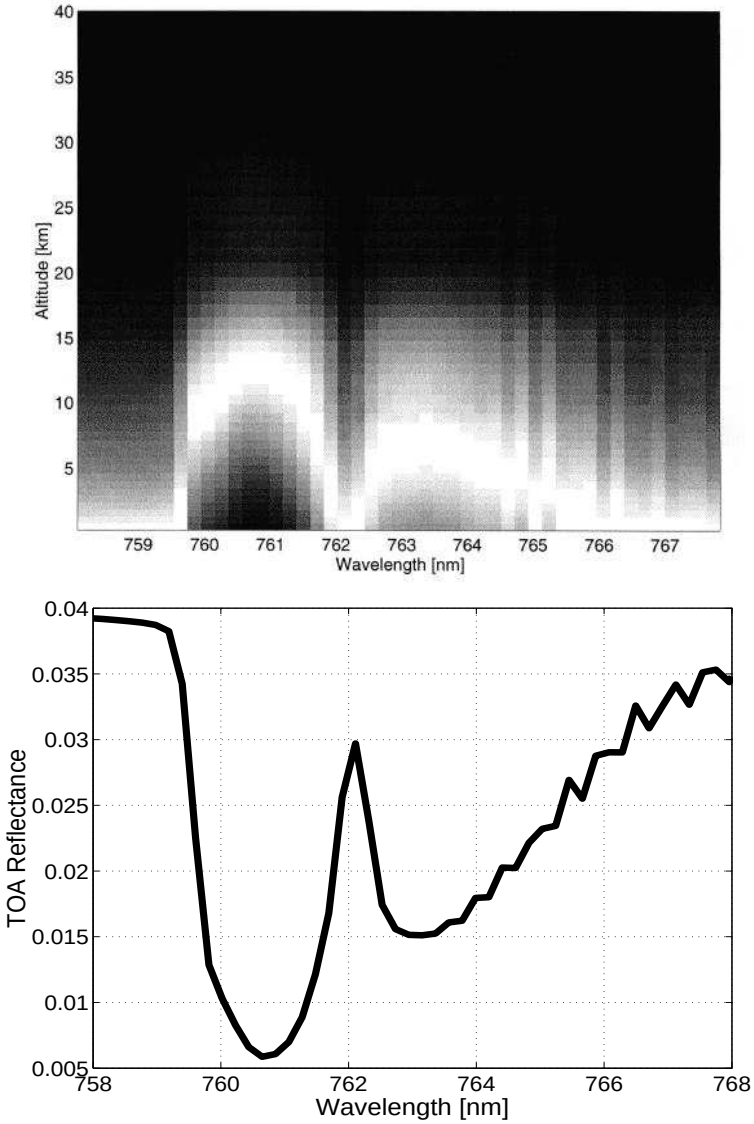

Figure 1.4: Top: altitude from which the majority of the backscattered radiance is coming considering the GOME spectral resolution [Koppers et al., 1998]. White = maximum backscattering, black = null backscattering. Bottom: oxygen A-band simulated TOA reflectance at GOME spectral resolution

of backscattering altitude coincides with the maximum of oxygen absorption.

Otherwise in proximity of the band tails the maximum of backscattering radiance is coming from the ground. Considering that the oxygen concentration profile is known, information about the aerosol profile distribution can be obtained with adequate modeling of such property.
A brief summary of works that faced the aerosol extinction profile retrieval problem either in the atmospheric windows or in the oxygen A-band follows.

Gabella, Guzzi, Kisselev and Perona **[1997]**
Authors studied the possibility to retrieve the aerosol extinction coefficient profile variation by considering atmospheric window wavelengths and nadir/quasi-nadir viewing satellite simulated measurements. The study has been done inverting the resulting linear relationship between the observable parameter (TOA radiance) and the unknown (aerosol extinction coefficient profile), by considering single scattering approach (i.e. for low Aerosol Optical Thickness (AOT)) and totally absorbing low boundary (null surface albedo). The analysis indicates that the retrieval gives satisfactory results in the lower atmosphere, while the variations in the stratosphere are retrieved with a lesser degree of accuracy and results strongly dependent on the a-priori aerosol extinction coefficient profile shape.

O'Brien **[1997]**
Using again the single scattering theory, O'Brien studied the possibility to use the space-based oxygen A-band measurements for the aerosol retrieval. He was able to demonstrate how measurements associated with varying degrees of oxygen absorption could distinguish the effects of aerosol and surface scatter. As the amount of oxygen absorption increases, the relative contribution of the aerosol scatter increases allowing for the detection of the effects of aerosol. Additionally, the relative effects of aerosol scattering, compared to the surface, increases with increasing oxygen optical depth.

Koppers, Murtagh and Jansson **[1998]**

The retrieval of both aerosol optical thickness and surface albedo is caring out for GOME instrument, considering the oxygen A-band spectral range and single scattering model. The inversion has been done using the Optimal estimation inversion theory.

Gabella, Kisselev and Perona **[1999]**

In this second work of Gabella et al., the retrieval of aerosol extinction coefficient profile variation is made using oxygen A-band wavelengths with and without atmospheric window wavelengths, for nadir and quasi-nadir viewing satellite configuration, considering single scattering approach and totally absorbing bottom boundary. Results shows an improvement accuracy in the retrieval when the oxygen A-band wavelengths are used respect to the retrieval made only using the atmospheric window wavelengths. The use of both oxygen and atmospheric windows wavelengths gives better results only for aerosol profile retrieval in stratosphere.

Heidinger and Stephens **[1999]**

The paper shows the possibility to use the reflectance spectra measured by a satellite platform in the oxygen A-band to retrieve clouds optical and physical properties as optical depth and phase function, vertical profile information include cloud top pressure, pressure thickness and surface albedo. This study is very interesting because it shows the feasibility of a limited amount of vertical profiling retrieval considering cloud layers. The multiple-scattering approach has been considered and the inversion technique, used for the retrieval and error assessment, is based on Optimal Estimation.

1.3 Aim of the thesis

As shown before there is a clear need to monitor and investigate the global distribution of atmospheric aerosol profile from passive remote sensing in-

struments, in particular taking into account the multiple scattering processes occurring in the atmosphere.

The aim of this work is to develop a multiple scattering inversion procedure for the *aerosol extinction coefficient* profile retrieval and error assessment for nadir and multi-angle passive remote sensing instruments. The procedure will be applied for the tropospheric aerosol extinction coefficient profile retrieval from SCIAMACHY nadir simulated measurements using atmospheric windows and oxygen A-band wavelengths. Also the contemporary use of atmospheric windows and oxygen A-band wavelengths will be discussed. SCIAMACHY simulated measurement has been used because, due to calibration real data procedure problems, until now SCIAMACHY data are not available.

The multiple scattering inversion procedure is composed by a *forward model* and an inversion method. The *forward model* developed (see Chapter (5)) is based on LIDORT code (see Chapter (3)) and must be able not only to reproduce the TOA intensity, as seen by the remote sensing instruments, but also to compute the *weighting function* for the retrieval parameter (in this case the *aerosol extinction coefficient*) and the *weighting functions* of all the other atmospheric parameters for which a complete error assessment is needed.

The inversion procedure for the retrieval, the sensitivity study and complete error assessment is based on Optimal Estimation (see Chapter (4)).

The multiple scattering inversion procedure has been applied to SCIAMACHY (see Chapter (2)) for two main reasons: the first one is its wide spectral range that permits the use of both atmospheric windows and oxygen A-band wavelengths; the second one is the possibility, very useful for the atmospheric species profile retrieval, to match the limb and nadir measurements. In particular, during the Oxford summer school in April 2003, in a final report work [*Corradini, De Smedt, Soebiyanta and Frankenberg,* 2003],

the SCIARAYS RTM [*Kaiser 2000, 2002; Kaiser et al., 2003*] has been used to demonstrate the possibility to retrieve the aerosol extinction coefficient profile in stratosphere using SCIAMACHY limb measurements. The SCIAMACHY limb measurements permits the retrieval from, approximately, $40-50$ to $8-10$ km (step about 3 km); if the nadir measurements study will reveal the possibility to retrieve the tropospheric profile, the aerosol profile retrieval of the intere atmosphere will become a real possibility.

1.4 Organization of dissertation

The thesis is structured in 8 Chapters included the Introduction:

Chapter 2: in this Chapter will be briefly described the main SCIAMACHY characteristics and will be identified the most transparent region of the spectrum measured by the instrument, in which the gaseous influences are negligible. The atmospheric windows wavelengths selected will be used for the retrieval test in Chapter (7).

Chapter 3: the LIDORT radiative transfer code, used as kernel of the *forward model* developed in Chapter (5), for the solution of the radiative transfer equation, will be described. Its main characteristics will be shown for the intensity and weighting function computation.

Chapter 4: here the Optimal Estimation inversion technique used for the retrieval, the sensitivity and the error assessment study is presented. The iterative inversion method and the information content and error assessment procedures, will be implemented together with the *forward model* developed in Chapter (5), to constitute the instrument used in this work to study the effectiveness of the aerosol extinction coefficient profile retrieval from satellite measurements.

Chapter 5: this Chapter regards the *forward model* development, its validation and the iterative inversion procedure implementation. All the input atmospheric process due to molecules and aerosol and the main implemented subroutines for the Top Of Atmosphere *intensity* and *weighting functions* computation, will be described in details. In particular the validation has been focused on the SCIAMACHY atmospheric windows wavelengths and oxygen A-band spectral range, used for the *aerosol extinction coefficient* retrieval.

Chapter 6: here will be set all the parameters needed for the *aerosol extinction coefficient* tropospheric profiles retrieval test and error assessment considering SCIAMACHY nadir simulated measurements.

Chapter 7: a complete a-priori analysis has been execute for the *aerosol extinction coefficient* profile retrieval and error assessment for SCIAMACHY nadir configuration, considering atmospheric windows and oxygen A-band wavelengths. For each test, two aerosol profile configuration, representative of maritime and desertic aerosol situations, has been considered.

Chapter 8: the conclusion of the work will be presented.

Chapter 2

SCIAMACHY

In the following the main characteristics of SCIAMACHY instrument will be described.
Using MODTRAN and SCIATRAN Radiative Transfer Model (RTM) will be identified the most transparent region of the SCIAMACHY spectrum measured (i.e. the spectral regions where the gaseous influences are negligible) to selected the relative atmospheric window wavelengths.

2.1 SCanning Imaging Absorption spectroMeter for Atmospheric CartograpHY - SCIAMACHY

SCIAMACHY [*Bovesmann et al.,* 1999] is one of the instruments among the ESA satellite ENVISAT [*URL http://envisat.esa.int*], launched on March 2002. ENVISAT fly on a sun-synchronous polar orbit with 10 a.m. descending node and carry a large range of instruments for probing Earth. SCIAMACHY is an imaging spectrometer whose primary mission objective is to perform global measurements of trace gases (O_2, NO_2, $OClO$, BrO, SO_2, $HCHO$, H_2O, CH_4, H_2O, CH_4, CO_2, CO and N_2O) in the troposphere and stratosphere. The solar radiation transmitted, backscattered and reflected from the atmosphere is recorded at relatively high resolution (0.2 μm to 0.5 μm) from the ultraviolet, through the visible to the near infrared, over the

range 240 nm to 1700 nm, and in selected regions between 2.0 μm and 2.4 μm (see Table (2.1)). In Table (2.1) are also shown the instrument slit function types.The large wavelength range is also ideally suited for the detection of clouds and aerosols. SCIAMACHY is an evolute version of GOME, which has been flying on ERS2 since 21 April 1995. Its channels cover the same wavelength range in the UV/Vis (240 nm to 790 nm) as the first four SCIAMACHY channels. In Figure (2.1) has been shown the comparison between the GOME and SCIAMACHY spectral range and the new molecules that can be detected by SCIAMACHY thanks to the new IR channels. The

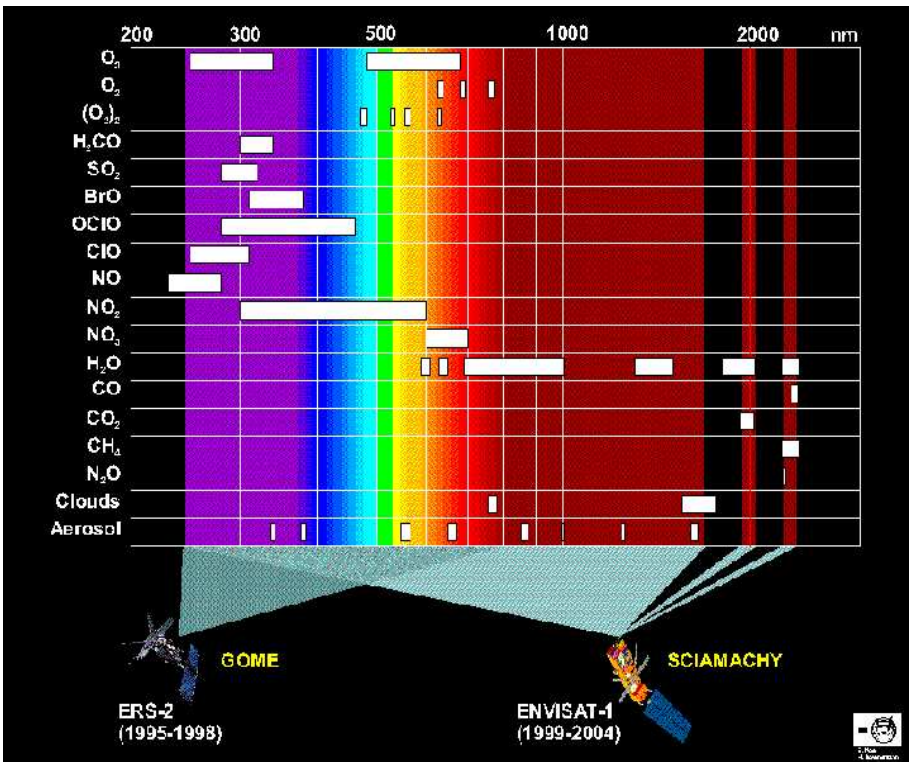

Figure 2.1: GOME and SCIAMACHY spectral range and atmospheric species detected.

UV-VIS-NIR spectral range has the advantage that hight signal/noise ratios can be achieved due to the relatively high energy of the photons and the large intensity of the solar radiation; the disadvantage is that the night-side cannot be observed. SCIAMACHY has three different viewing geometries: nadir, limb, and sun/moon occultations which yield total column values as

SCIAMACHY channel	*Spectral range (nm)*	*Resolution (nm)*	*Slit Function*
1	240 – 314	0.24	Single Hyperbolic
2	309 – 405	0.26	Single Hyperbolic
3	394 – 620	0.44	Single Hyperbolic
4	604 – 805	0.48	Single Hyperbolic
5	785 – 1050	0.54	Single Hyperbolic
6	1000 – 1750	1.48	Gaussian
7	1940 – 2040	0.22	Voigt
8	2265 – 2380	0.26	Voigt

Table 2.1: SCIAMACHY spectral range, resolution, slit function type and relative FWHM.

well as distribution profiles in the stratosphere and the troposphere for trace gases and aerosols.

- *nadir measurement mode*

  The instrument is facing straightly downward to measure the radiance from underneath the satellite (see Figure (2.2)). Thus solar radiation,

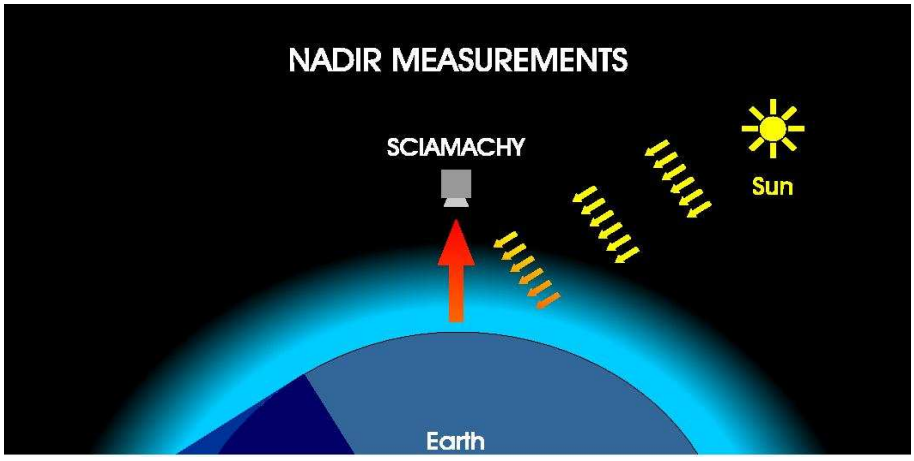

Figure 2.2: Nadir view of SCIAMACHY. [graphics by *S. Noël*]

which has been scattered in the atmosphere and/or reflected on the surface, is recorded. These measurements are performed on the whole day-side of Earth. In nadir mode, the nadir mirror scans across the satellite track and returns to its original position for the next scan.

Each scan covers an area on the ground of approximately 30 km along track and 960 km across track. A better resolution of 60 km across track will be achieved for the important constituents O_3, NO_2, H_2O, and aerosols in mid and high latitudes. The seven broad-band polarization measurement devices (PMDs) will even perform with 15 km resolution across track for cloud characterization.

The global coverage can be achieved in three days as Envisat is flying in a sun-synchronous polar orbit and Earth is rotating underneath.

- *occultations measurement mode*

  The instrument is tracking the sun (or the moon) during its rise or set behind Earth (see Figure (2.3)). Thus mainly directly transmitted solar (or lunar) radiation is recorded for different tangent altitudes. Occultations measurements yield highly accurate information on the vertical structure of the atmosphere, but they have a bad horizontal resolution owing to the averaging over long paths. They are not suitable to obtain measurements with global coverage since only one sunrise can be measured per satellite orbit.

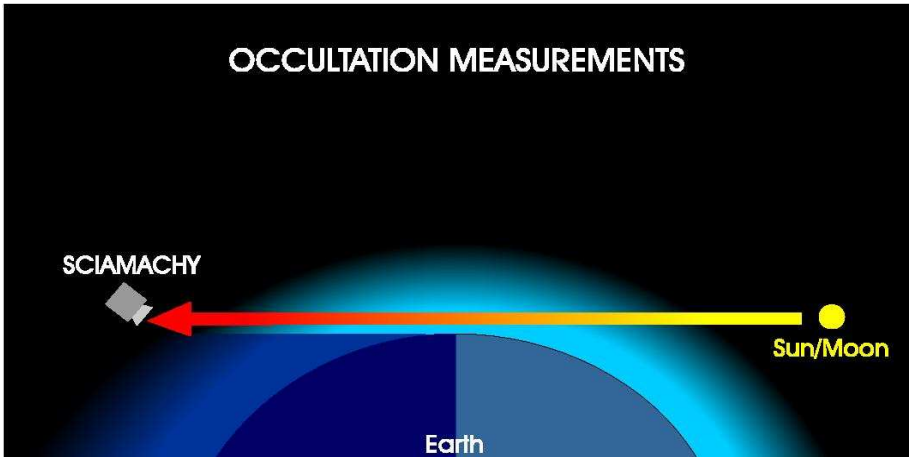

Figure 2.3: Occultations view of SCIAMACHY. [graphics by *S. Noël*]

- *limb measurement mode*

  The limb measurement mode of SCIAMACHY is a combination of the

nadir and occultations geometries (see Figure (2.4)). The instrument

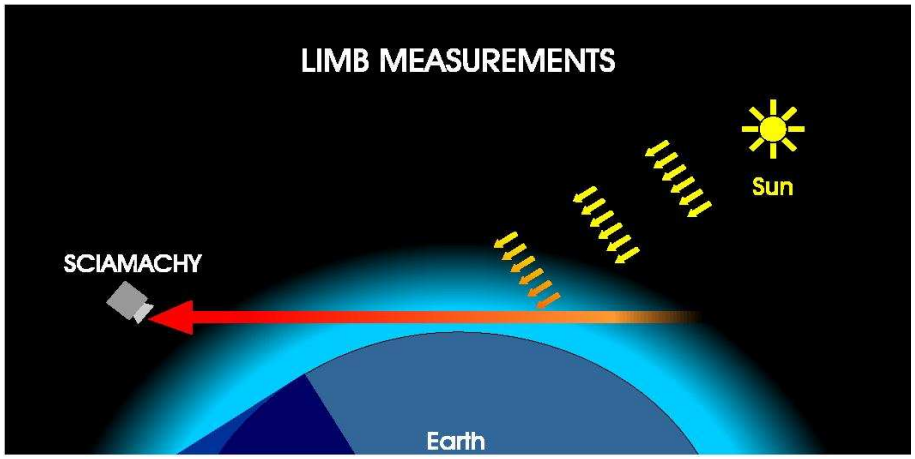

Figure 2.4: Limb view of SCIAMACHY. [graphics by *S. Noël*]

is scanning the Earth's limb like in occultations mode, while the sun is illuminating the atmosphere from above like in nadir mode. Thus atmospheric radiance spectra can be obtained for different tangent altitudes at any location on Earth's day-side. Starting with approximately zero tangent height, a horizontal scan of 960 km at the tangent point is performed. Then the tangent height is stepped up by 3 km and another horizontal scan back is done. This procedure is repeated, until typically 34 horizontal scans with tangent heights between 0 and 100 km are obtained. The horizontal resolution across track is limited by the IFOV and the number of readouts during the horizontal scan. With typically four readouts, a value of roughly 240 km will be achieved. It can by no means be improved to 110 km or less. The horizontal resolution along track is determined by the nearly horizontal paths with lengths of the order of several, say four, hundred kilometers.

- *limb-nadir matching*

  A specialty of SCIAMACHY is depicted in Figure (2.5): The timeline of operations is designed in a way that each limb measurement is followed after 7 minutes by a nadir measurement of the same atmospheric

volume. Since the stratospheric profile of a trace gas is determined from the limb measurement, the stratospheric column is known. Subtracting this from the total column, which is measured in nadir, yields the tropospheric column. Therefore SCIAMACHY is capable of measurements of the troposphere. Future advanced retrieval algorithms will exploit SCIAMACHY's limb-nadir matching even more efficiently by retrieving from the matching limb and nadir measurements simultaneously, i.e., in a tomographic fashion. This approach is expected to yield improved tropospheric parameters as well as vertically and horizontally resolved parameter fields.

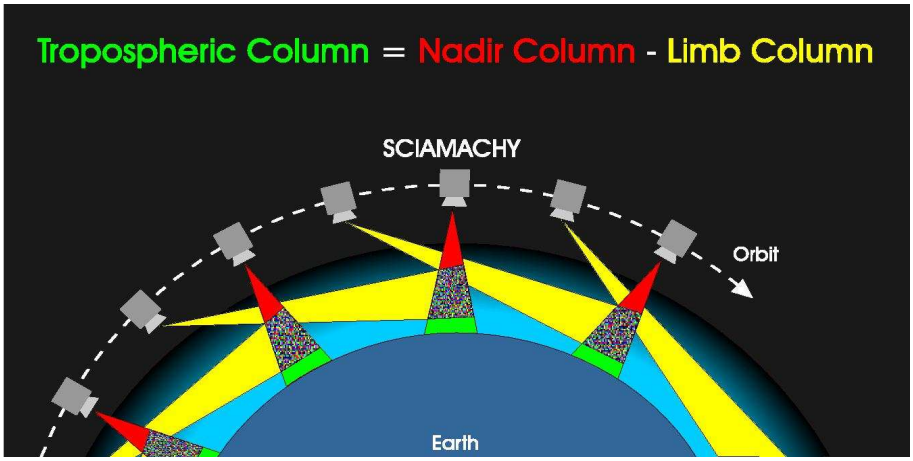

Figure 2.5: Limb-Nadir measurements matching view of SCIAMACHY. [graphics by *S. Noël*]

2.2 Atmospheric windows wavelengths selection for SCIAMACHY spectral range

The aim of this Paragraph is to identify the most transparent region of the spectrum measured by SCIAMACHY, in which it is possible retrieve the aerosol without gaseous corrections.

In order to select the proper wavelengths has been analyzed the solar spectrum in the SCIAMACHY spectral range. The choice has been done analyzing both the atmospheric TOA *transmittance* computed using MODTRAN

3 (v1.5) Radiative Transfer Model (RTM) [*Anderson et al., 1995*] and the percentage difference between the SCIAMACHY simulated spectrum computed with and without gas absorption, using SCIATRAN RTM [*Rozanov et al.,* 1997, see Paragraph (5.2.1)]. The *transmittance* computation were car-

SCIAMACHY channel	*Lower* λ (nm)	*Upper* λ (nm)
$2-3$	350	434
4	751	758
4	775	786
5	855	878
$5-6$	1020	1067
6	1242	1250
6	1553	1569
6	1588	1596
6	1620	1627

Table 2.2: The most transparent windows in the atmosphere and the relative SCIAMACHY channels. The selection has been carried out using MODTRAN 3 at maximum resolution, with a *transmittance* threshold of 0.996.

ried out with MODTRAN considering its maximum spectral resolution and in absence of aerosol and molecular scattering. A *transmittance* threshold $t \geq 0.996$ and a window width ≥ 3 nm was selected to reduce the impact of the weak bands of the gases and the effect of the band tails. The selection was referred to the 8 SCIAMACHY channels. In Table (2.2) are shows the most transparent atmospheric windows find and the relative SCIAMACHY channels.

The SCIATRAN simulation has been done to select the wavelengths, into the atmospheric windows, for which the percentage difference between the spectra computed with and without gas absorption is less than 1%. Taking into account the SCIAMACHY high spectral resolution and to minimize the error due to the instrument spectral calibration, the reflectance associated by a considered atmospheric windows wavelength (λ), is computed as the mean reflectance of the wavelengths comprised between $(\lambda - \delta/2)$ and $(\lambda + \delta/2)$. So, the wavelengths selected are those for which around $\pm\delta/2$ the percentage

reflectance difference is less than 1%. The choice of parameter δ has been done in order to consider about 9 wavelengths for each λ selected. Taking into account that the SCIAMACHY spectral resolution is variable, also δ will depend on the channel considered. In Figures (2.6), (2.7), (2.8), (2.9) and (2.10) are shown the SCIAMACHY TOA reflectance spectra with and without gas absorption, the percentage difference between the two spectra with the selected wavelengths and the parameter δ.

In Table (2.3) are summarized the wavelengths choice for the aerosol

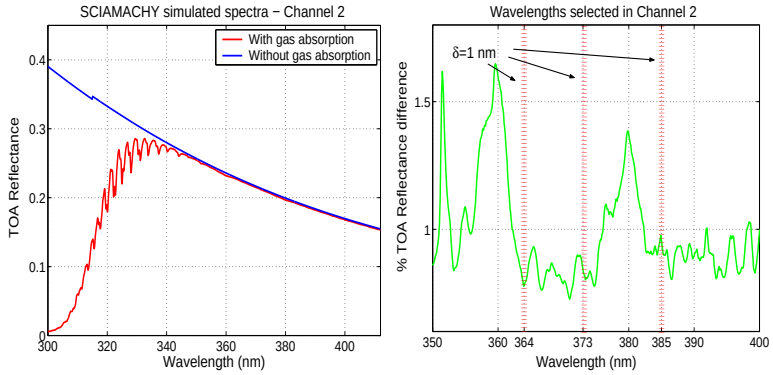

Figure 2.6: Left plate: simulated SCIAMACHY TOA reflectance spectra with and without gas absorption for SCIAMACHY channels 2. Right plate: percentage TOA reflectance difference between spectra with and without gas absorption in atmospheric window in channels 2 and wavelengths selection.

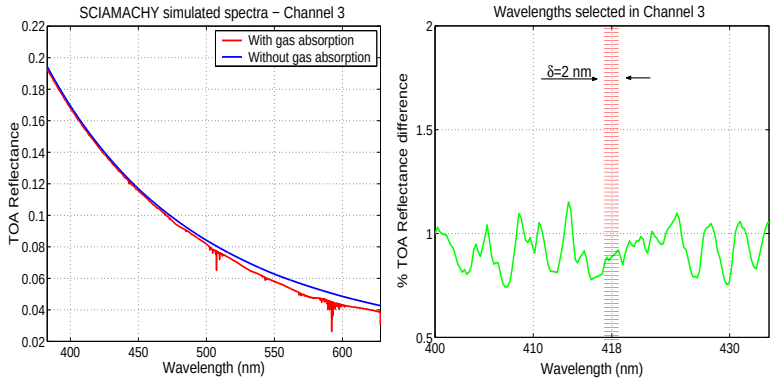

Figure 2.7: Left plate: simulated SCIAMACHY TOA reflectance spectra with and without gas absorption for SCIAMACHY channels 3. Right plate: percentage TOA reflectance difference between spectra with and without gas absorption in atmospheric window in channel 3 and wavelengths selection.

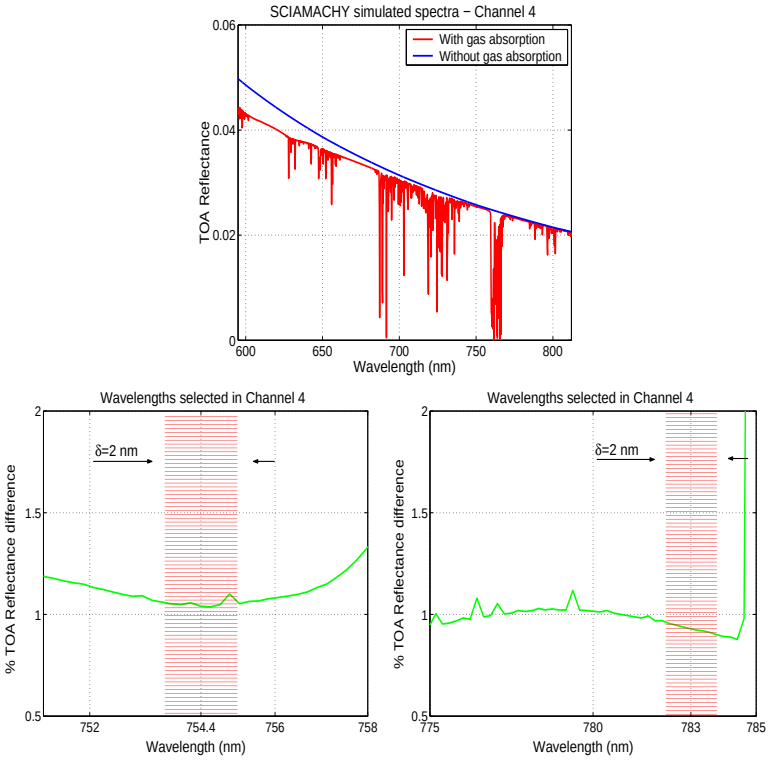

Figure 2.8: Top plate: simulated SCIAMACHY TOA reflectance spectra with and without gas absorption for SCIAMACHY channels 4. Bottom plates: percentage TOA reflectance difference between spectra with and without gas absorption in atmospheric window in channel 4 and wavelengths selection.

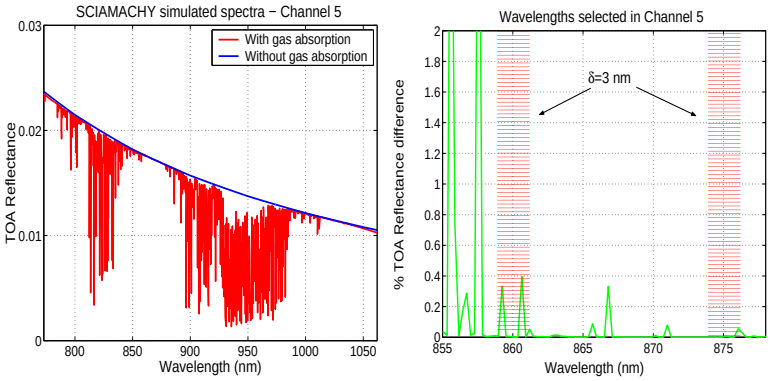

Figure 2.9: Left plate: simulated SCIAMACHY TOA reflectance spectra with and without gas absorption for SCIAMACHY channels 5. Right plate: percentage TOA reflectance difference between spectra with and without gas absorption in atmospheric window in channel 5 and wavelengths selection.

retrieval into the atmospheric windows and the relative SCIAMACHY channels.

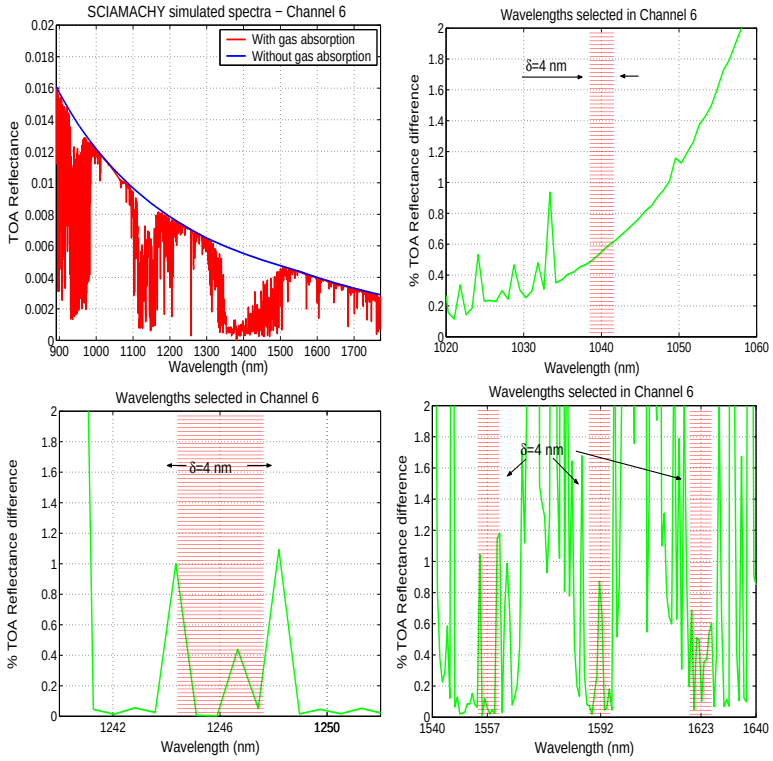

Figure 2.10: Top left plate: simulated SCIAMACHY TOA reflectance spectra with and without gas absorption in atmospheric window in channel 6. Top right plate and bottom plates: percentage TOA reflectance difference between spectra with and without gas absorption in atmospheric window in channel 6 and wavelengths selection.

SCIAMACHY channel	Wavelengths selected
2	364, 373, 385
3	418
4	754.4, 783
5	860, 875
6	1040, 1246, 1557, 1592, 1623

Table 2.3: Atmospheric windows SCIAMACHY wavelengths selected for the aerosol retrieval.

Chapter 3

LInearized Discrete Ordinate Radiative Transfer (LIDORT)

In this Chapter the LIDORT radiative transfer code, used as kernel for the *forward model* development (see Chapter (5)), will be described. Starting from the radiative transfer equation, its main characteristics, for the intensity and *weighting functions* computation, will be shown. Finally a summary of the intensity and *weighting functions* user input variables will be given.

3.1 Introduction

LIDORT [*Spurr, 2001*] is a radiative transfer (RT) tool based on the discrete ordinate approach [*Chandrasekhar, 1940*] for the solution of the radiative transfer equation. Like DISORT (DIScrete Ordinate Radiative Transfer) [*Stamnes et al., 1988; Thomas and Stamnes, 1999*], the discrete ordinate approach involves the use of a numerical quadrature scheme to approximate the integral over polar directions in dealing with multiple scattering source term. The quadrature used is a double-Gauss scheme defined separately for up-welling and down-welling radiance. The principal corrections, used for the solution of radiative transfer equation, are the delta-M scaling procedure [*Wiscombe, 1977*] (see Par. (3.4.1)) and the Nakajima-Tanaka single scatter correction [*Nakajima and Tanaka, 1988*] (see Par. (3.4.2)).
The main characteristic of LIDORT is the ability to generate analytical

weighting functions (linearization, denote the process of differentiation) and intensity fields at the same time with only just one called. The traditionally weighting function determination is based on finite difference estimation [*see GOMETRAN RTM, Rozanov et al., 1997, 1998, 2000; SCIATRAN RTM, Buchwitz et al., 1998*]; this procedure need repeated RTM calls that produce a very expensive computer resource. Another problem is the accuracy, linked by the arbitrary choice of the perturbation (see Paragraph (5.2.2.2)).
Both *weighting functions* and intensity fields can be generated anywhere in the atmosphere, for upwelling and down-welling directions, for arbitrary optical depths and streams angles.
The inhomogeneous atmosphere is composed of a number of homogeneous horizontal layers. The radiation field depend on a single vertical coordinate (the vertical optical depth τ or the altitude) and the two directional variables μ (cosine of the polar angle) and ϕ (azimuth angle with respect to a given direction). The simplest stratification assumes a plane-parallel RT medium that neglect any sphericity due to the Earth curvature. To allow for curvature effect, the simplest approach assumes that the attenuation of the direct solar beam is computed in a spherical-shell atmosphere, but that line-of-sight attenuation and all scattering events continue to be treated for a plane-parallel medium. This is the so-called *pseudo-spherical approximation*. The advantage of this approximation is that the power and speed of the plane-parallel scattering formalism can be retain without the need to call a greatly more complex and time-consuming full-spherical radiative transfer model. It has been shown [*Dahlback, 1991; Caudill, 1997*] that the pseudo-spherical treatment is adequate for solar zenith angles up to 90° provided the line-of-sight is reasonably close ($\simeq$ 20 - 25° or less) to the nadir. LIDORT also consider the sphericity correction for line-of-sight viewing some distance from the nadir; attenuation in these directions is also treated for a curved stratified atmosphere, and the radiation field is integrated along the line-of-sight direction instead of the nadir direction assumed for the ordinary

pseudo-spherical calculation.

Scattering is treated as non-conservative (the process results in partial absorption of the light energy) and coherent (after scattering the wave frequency don't change) . The Rotational Raman scattering is modeled to first order and no polarization is considered.

LIDORT has the capability to deliver *weighting functions* with respect to layer atmospheric variables, surface albedo and emission. The aerosol *weighting functions* are computed not only with respect to the amount or degree of aerosol scattering and attenuation, but also with respect to quantities such as the asymmetry parameter which affect the angular distribution of scattering.

Like DISORT, LIDORT is a subroutine called from a user defined environment. For any given application, the user must construct an atmospheric preparation module to set up the necessary inputs required by the model, the most important being the vertical optical depths, layer single scattering albedo and phase functions, along with their sensitivities, to the atmospheric parameters for which *weighting functions* must be computed.

In the following has been presented an outline of the radiative transfer equation solution for the intensity (Par. (3.2)) and *weighting function* computation (Par. (3.3)), the principal approximation considered (Par. (3.4)) and an overview of the user inputs needed for *forward model* development (Paragraph (3.2.1)).

In Chapter 4 will be described in detail the user inputs for the development of the *forward model* used in the thesis.

3.2 Outline of Radiative Transfer Equation (RTE) solution in UV-VIS-NIR spectral range

In this section will be briefly shown the *discrete-ordinate* method for the solution of the RTE in UV-VIS-NIR spectral range as used in LIDORT code. For more details see *Spurr* [2001] and *Thomas-Stamnes* [1999].

Following the Lamber-Beer law, the Radiative Transfer Equation (RTE) for layer p can be written as:

$$\mu \frac{dI(\tau, \mu, \phi)}{d\tau} = I(\tau, \mu, \phi) - J_p(\tau, \mu, \phi) \tag{3.1}$$

where:

τ is the optical depth;

$\mu = cos(\theta)$, where θ is zenith angle of the reflected radiation;

ϕ is the azimuth angle of the reflected radiation;

$I(\tau, \mu, \phi)$ is the diffuse radiance in direction (μ, ϕ) at optical depth τ;

$J_p(\tau, \mu, \phi)$ is the source function of layer p.

Ignore thermal emission from the surface, the source function becomes:

$$J_p(\tau, \mu, \phi) = \frac{\omega_p}{4\pi} \int_{-1}^{1} d\mu' \int_{0}^{2\pi} d\phi' p_p(\mu, \phi; \mu', \phi') I(\tau, \mu', \phi') + \\ + \frac{\omega_p}{4\pi} p_p(\mu, \phi; -\mu_0, \phi_0) F_p e^{-\lambda_p \tau} \tag{3.2}$$

where:

ω_p is the total single scattering albedo;

$p_p(\mu, \phi; \mu', \phi') = p_p(\mu_s)$ is the phase function for scattering, $\mu' (= cos(\theta'))$, ϕ' are the directions of the photons before the scattering and μ_s is the scattering angle ($\mu_s = \mu'\mu + \sqrt{1-\mu'^2}\sqrt{1-\mu^2} cos(\phi' - \phi)$);

$(-\mu_0, \phi_0)$ is the solar beam direction entering in the atmosphere, $\mu_0 = cos(\theta_0)$, θ_0 is the Solar Zenith Angle (SZA), and ϕ_0 is the Solar Azimuth Angle (SAA);

$F_p \equiv F_0$ (the solar irradiance at Top Of Atmosphere (TOA)) and $\lambda_p = \frac{1}{\mu_0}$ for the plane-parallel case. In the pseudo-spherical treatment, F_p and λ_p are adjusted to account for the reduced path of the direct beam.

Expanding the diffuse radiance in Fourier cosine series and the phase function in Legendre polynomials:

$$I(\tau,\mu,\phi) = \sum_{m=0}^{2N-1} I^m(\tau,\mu)\cos m(\phi_0-\phi) \tag{3.3}$$

$$p_p(\mu_s) = \sum_{l=0}^{2N-1} (2l+1)\chi_{l,p}P_l(\mu_s) \tag{3.4}$$

where:

$(2l+1)$ is the $l-th$ Legendre coefficient;

$P_l(\mu_s)$ is the $l-th$ Legendre polynomials [the first four are: $P_0(\mu_s)=1$, $P_1(\mu_s)=\mu_s$, $P_2(\mu_s)=\frac{1}{2}(3\mu_s^2-1)$, $P_3(\mu_s)=\frac{1}{2}(5\mu_s^3-3\mu_s)$];

$\chi_{l,p}$ is the $l-th$ Legendre moment of the layer p, given by:

$$\chi_{l,p} = \frac{1}{2}\int_{-1}^{1} P_l(\mu_s)p_p(\mu_s)d\mu_s \tag{3.5}$$

It is common to denote the first moment χ_1 as g; its represent the degree of asymmetry of the angular scattering and is therefore called the $asymmetry factor$. If $g=0$ the scattering is isotropic, if $g=-1$ the scattering is complete back and if $g=1$ is complete forward.

An important property of the phase function is the normalization, i.e. the integral of the phase function over the solid angle (the scattering probability) must be one:

$$\frac{1}{4\pi}\int_{\Omega} p_p(\mu_s)d\Omega = 1 \tag{3.6}$$

where Ω is the solid angle. It can be shown that the result of the integral in (3.6) is the first Legendre moment:

$$\frac{1}{4\pi}\int_{\Omega} p_p(\mu_s)d\Omega = \chi_0 \tag{3.7}$$

so, to satisfy the normalization property, the first phase function Legendre moment must always be set to one.

Considering the *Addition Theorem for Spherical Harmonics* the expansion of the phase function is simplifying:

$$P_l(\mu_s) = P_l(\mu')P_l(\mu) + 2\sum_{m=1}^{l} \Lambda_l^m(\mu')\Lambda_l^m(\mu)\cos m(\phi'-\phi) \tag{3.8}$$

where $\Lambda_l^m(\mu)$ are the *normalized associated Legendre polynomial* defined by:

$$\Lambda_l^m(\mu) \equiv \sqrt{\frac{(l-m)!}{(l+m)!}} P_l^m(\mu) \tag{3.9}$$

where $P_l^m(\mu)$ is the *associated Legendre polynomial*.
Substituting the equation (3.8) into the (3.4) we obtain:

$$p_p(\mu_s) = \sum_{m=0}^{2N-1} p^m(\mu', \mu) cos(m(\phi' - \phi)) \tag{3.10}$$

where:

$$p^m(\mu', \mu) = (2 - \delta_{0m}) \sum_{l=m}^{2N-1} (2l+1) \chi_{l,p} \Lambda_l^m(\mu') \Lambda_l^m(\mu) \tag{3.11}$$

Substituting the equation (3.10) and (3.3) into (3.1) we obtain $2N$ coupled equations for each successive Fourier components $m = 0, \ldots, 2N-1$:

$$\mu \frac{dI_m}{d\tau} = dI_m - \frac{1}{2} \int_{-1}^{1} D_p^m(\mu, \mu') I_m(\tau, \mu) d\mu' - Q_p^m(\mu) F_p e^{-\lambda_p \tau} \tag{3.12}$$

where:

$$D_p^m(\mu, \mu) = \frac{1}{2} \sum_{l=m}^{2N-1} \omega_p \chi_l(\tau) \Lambda_l^m(\mu) \Lambda_l^m(\mu') \tag{3.13}$$

$$Q_p^m(\mu) = \frac{1}{2\pi} (2 - \delta_{m0}) D_p^m(\mu, -\mu_0) \tag{3.14}$$

In the interest of clarity, in the following, we'll omit the Fourier superscripts m and the layer index p.
One of the approximated techniques capable of approaching the exact solution as closely as desired is the *discrete ordinate method*. In the N^{th}-order *discrete ordinate approximation*, the integral in (3.12) is approximated by a summation using Gauss-Legendre quadrature over the two half space separately. This technique transform the pair of coupled integro-differential equations into a system of coupled differential equations. Each quadrature has N points, with abscissae μ_i and weights a_i for $i = 1, \ldots, N$ in the positive half-space, and corresponding values $\mu_{-i} = -\mu_i$ and $a_{-i} = a_i$ in the other half space. The double of the quadrature points number ($2N$) is called

STREAMS number.

Using the Gauss-Legendre quadrature and defining $M_i^+ = I_i^+ I_i^-$ and $M_i^- = I_i^- I_i^-$, with $I_i^\pm = I(\tau, \pm\mu_i)$, we can separate the (3.12) in two parts:

$$\frac{dM_i^+}{d\tau} = -\sum_{j=1}^{N}(\xi_{ij} - \eta_{ij})M_j^- - \frac{1}{\mu_i}(Q_i^+ - Q_i^-)Fe^{-\lambda\tau} \tag{3.15}$$

$$\frac{dM_i^-}{d\tau} = -\sum_{j=1}^{N}(\xi_{ij} + \eta_{ij})M_j^+ - \frac{1}{\mu_i}(Q_i^+ + Q_i^-)Fe^{-\lambda\tau} \tag{3.16}$$

where $Q_i^\pm = Q(\pm\mu_i)$ and:

$$\xi_{ij} = \frac{1}{\mu_i}(a_i D_{ij}^+ - \delta_{ij}) \tag{3.17}$$

$$\eta_{ij} = \frac{1}{\mu_i} a_i D_{ij}^- \tag{3.18}$$

with $D_{ij}^\pm = D(\mu_i, \pm\mu_j)$.

A single equation for M_i^- can be obtained from (3.15) and (3.16):

$$\frac{d^2M_i^-}{d\tau^2} = \sum_{j=1}^{N}\Gamma_{ij}M_j^- + d_i Fe^{-\lambda\tau} \tag{3.19}$$

where:

$\Gamma_{ij} = \sum_{k=1}^{N}(\xi_{ik} + \eta ik)(\xi_{ik} - \eta ik)$;

$d_i = \frac{1}{\mu_i}\lambda(Q_i^+ + Q_i^-) + \frac{1}{\mu_i}\sum_{j=1}^{N}(\xi_{ik} + \eta ik)(Q_i^+ - Q_i^-)$.

The general solution to (3.19) may be written:

$$M_i^- = \tilde{M_i^-} + W_i^- Fe^{-\lambda\tau} \tag{3.20}$$

with $\tilde{M_i^-}$ the general solution to the homogeneous part of (3.20). The latter admits solutions of the form $\tilde{M_i^-} = Y_j^- e^{-k\tau}$, and this leads to the eigenproblem:

$$\sum_{j=1}^{N}\Gamma_{ij}Y_j^- = \gamma Y_i^- \tag{3.21}$$

where $\gamma = k^2$. Denote the N eigenvectors and eigenvalues of this system (3.21) as Y_{ij}^-, γ_j, $j = 1, \ldots N$.

The inhomogeneous or particular part of the solution can be found by substitution of (3.20) into (3.19):

$$\lambda^2 W_i^- = \sum_{j=1}^{N} \Gamma_{ij} W_j^- + d_i \tag{3.22}$$

and solving for W_i^-.

Bringing the two part together, the general solution to (3.19) is then:

$$M_i^- = \sum_{j=1}^{N} [\tilde{L}_j^+ Y_{ij}^- e^{-k_j \tau} + \tilde{L}_j^- Y_{ij}^- e^{+k_j \tau}] + W_i^- F e^{-\lambda \tau} \tag{3.23}$$

where $\tilde{L}_j^+$ and $\tilde{L}_j^-$ are the $2N$ constants of integration, and $k_j = +\sqrt{\gamma_j}$. Insert equation (3.23) into (3.15) we obtain:

$$M_i^+ = \sum_{j=1}^{N} [\tilde{L}_j^+ Y_{ij}^+ e^{-k_j \tau} - \tilde{L}_j^- Y_{ij}^- e^{+k_j \tau}] + W_i^+ F e^{-\lambda \tau} \tag{3.24}$$

with:

$$Y_{ij}^+ = \frac{1}{k_j} \sum_{k=1}^{N} (\xi_{ik} - \eta_{ik}) Y_{kj}^- \tag{3.25}$$

$$W_i^+ = \frac{1}{\lambda} \sum_{j=1}^{N} (\xi_{ij} - \eta_{ij}) W_j^- + \frac{1}{\lambda \mu_i} (Q_i^+ - Q_i^-) \tag{3.26}$$

Returning to I^+ and I^- and reintroducing the Fourier and layer indices, the solution for a Fourier component of the radiance at the polar Gaussian angles for any optical depth in a specific layer p becomes:

$$I_p^m(\tau, \mu_i) = \sum_{j=1}^{N} [L_{j,p}^+ X_{ij,p}^+ e^{-k_{j,p}(\tau - \tau_{p-1})} + L_{j,p}^- X_{ij,p}^- e^{-k_{j,p}(\tau_p - \tau)}] + Z_{i,p} F_p e^{-\lambda_p \tau} \tag{3.27}$$

$\forall i \in [\pm 1, \ldots \pm N]$; $L_{j,p}^+$ and $L_{j,p}^-$ are integration constants and:

$$X_{ij,p}^+ = \frac{1}{2} (Y_{ij,p}^+ + Y_{ij,p}^-) \tag{3.28}$$

$$X_{ij,p}^- = \frac{1}{2} (Y_{ij,p}^+ - Y_{ij,p}^-) \tag{3.29}$$

$$X^{+}_{ij,p} = \frac{1}{2}(W^{+}_{i,p} + W^{-}_{i,p}) \tag{3.30}$$

The integration constants follow from a set of boundary conditions:

1) the downward diffuse radiation at the top of the atmosphere (TOA) is zero in the absence of thermal emission sources;

2) at each intermediate layer boundary, the radiance is continuous in all polar (elevation) and azimuthal directions;

3) the upwelling radiance at the bottom of the atmosphere is a known function of the incident down-welling radiance, the dependence being expressed in terms of the reflectance property of the surface.

In the next Paragraph will be summarize the user input atmospheric properties for each layer that must be set to compute the intensity.

3.2.1 Summarizing of Intensity computation user input

In this Paragraph will be summarized the user input parameters needed for the TOA intensity computation; the computation for each term will be described in details in the next Chapter.

The wavelength index will be omitted for clarity.

Total optical thickness (τ_p):

$$\tau_p = \epsilon_p(z_p - z_{p-1}) = (\epsilon^{Ray}_p + \epsilon^{Aer}_p)(z_p - z_{p-1}) \tag{3.31}$$

where:

ϵ_p is the *total extinction coefficient* of layer p

$\epsilon^{Ray}_p = \sigma^{Ray}_p + \alpha^{Ray}_p$ is the *Rayleigh extinction coefficient*, σ^{Ray}_p is the *molecular scattering coefficient* and α^{Ray}_p is the *molecular absorbing coefficient*;

ϵ^{Aer}_p is the *aerosol extinction coefficient*.

Total single scattering albedo (ω_p):

$$\omega_p = \omega^{Ray}_p + \omega^{Aer}_p = \frac{\sigma^{Ray}_p}{\epsilon_p} + \frac{\sigma^{Aer}_p}{\epsilon_p} \tag{3.32}$$

where:
ω_p^{Ray} is the *Rayleigh single scattering albedo*;
ω_p^{Aer} is the *aerosol single scattering albedo*;
σ_p^{Aer} is the *aerosol scattering coefficient.*
Total phase function (p_p):

$$p_p = (\omega_p^{Ray} p_{R,p} + \omega_p^{Aer} p_{A,p})/\omega_p \tag{3.33}$$

where:
$p_{R,p}$ is the *Rayleigh phase function*;
$p_{A,p}$ is the *aerosol phase function.*

As shown in the previous Paragraph, if the *solar irradiance* (F_0) is giving in input, LIDORT gives in output the TOA *radiance* (I). In many cases of remote sensing retrieval, the TOA *reflectance*, defining by equation (3.34), is used (see for example [*CADAPA, 1998*] for the aerosol retrieval from GOME data):

$$R = \frac{\pi I}{\mu_0 F_0} \tag{3.34}$$

In this case the simulated *reflectance* is obtained setting the *solar irradiance* equal to π/μ_0.
As will be shown in Paragraph (5.1.4), in the forward model has been implemented the possibility to compute both *radiance* and *reflectance.*

3.3 *weighting function* computation

As described before the main characteristics of LIDORT is the ability to generate analytical *weighting functions* with respect to layer atmospheric and surface variables. The computation start with differentiation of the Fourier

sum equation (3.3):

$$\frac{\partial I(0,\mu,\phi)}{\partial \xi_p} = \sum_{m=0}^{2N-1} \frac{\partial I^m(0,\mu)}{\partial \xi_p} \cos m(\phi_0 - \phi) \tag{3.35}$$

where ξ_p is the is the atmospheric variables considered.

The exposition of the analytical determination of derivatives of the TOA intensity with respect to layer parameters x_p is out of the aim of this work (for details see *Spurr* [2001]). It can be shown that the analytic *Parameter Normalized Weighting Function* (*PNWF*) ($K_\xi(p)$) for the different atmospheric parameters is function of:

$$K_\xi(p) = \xi_p \frac{\partial I(0,\mu,\phi)}{\partial \xi_p} = f(\omega_p u_{\xi,p}; e_p v_{\xi,p}; \omega_p \chi_{\xi,p,l}(u_{\xi,p} + z_{\xi,p,l})) \tag{3.36}$$

where:

$$u_{\xi,p} = \sum_s u^s_{\xi,p} \tag{3.37}$$

is the relative variation for *total single scattering albedo* in layer p with respect to variable ξ in that layer. Considering that the species s are molecules and aerosol, the (3.37) becomes:

$$u_{\xi,p} = u^{Ray}_{\xi,p} + u^{Aer}_{\xi,p} = \frac{\xi_p}{\omega^{Ray}_p} \frac{\partial \omega^{Ray}_p}{\partial \xi_p} + \frac{\xi_p}{\omega^{Aer}_p} \frac{\partial \omega^{Aer}_p}{\partial \xi_p}. \tag{3.38}$$

$$v_{\xi,p} = \frac{\xi_p}{e_p} \frac{\partial e_p}{\partial \xi_p} \tag{3.39}$$

is the relative variation for *total extinction* in layer p with respect to variable ξ in that layer.

$$z_{\xi,p,l} = \sum_s z^s_{\xi,p,l} \tag{3.40}$$

is the relative variation in the *l-th phase function moments* ($\chi^s_{\xi,p,l}$) for scatterer s in layer p with respect to variable ξ in that layer. Considering that the species s are molecules and aerosol:

$$z_{\xi,p,l} = z^{Ray}_{\xi,p,l} + z^{Aer}_{\xi,p,l} = \frac{\xi_p}{\chi^{Ray}_{l,p}} \frac{\partial \chi^{Ray}_{l,p}}{\partial \xi_p} + \frac{\xi_p}{\chi^{Aer}_{l,p}} \frac{\partial \chi^{Aer}_{l,p}}{\partial \xi_p}. \tag{3.41}$$

To obtain the *PNWF*, for every variables ξ_p, the above terms must be computed. In Paragraph (5.1.5) will be shown the expression of $u_{\xi,p}$, $v_{\xi,p}$ and

$z_{\xi,p,l}$ for the atmospheric variables used in this work.
The *surface albedo PNWF* is computing automatically from LIDORT code with no particular parameter setting request.

3.3.1 Consideration on the *Parameter Normalized Weighting Functions* and *aerosol extinction coefficient*

Computing the *Parameter Normalized Weighting Function* for an atmospheric parameter (ξ), i.e. multiplying the weighting function for the atmospheric parameter itself (see equation (3.36)), is like computing the *weighting function* on the logarithm of the atmospheric quantity:

$$\frac{\partial I(0,\mu,\phi)}{\partial ln(\xi_p)} = \frac{\partial I(0,\mu,\phi)}{\partial \xi_p}\frac{\partial \xi_p}{\partial ln(\xi_p)} = \xi_p \frac{\partial I(0,\mu,\phi)}{\partial \xi_p} \tag{3.42}$$

The *PNWF* are very useful when the atmospheric quantity to be retrieved vary greatly from the top to the bottom of the atmosphere, like in the case of the *aerosol extinction coefficient* profile (see Paragraph (6.1.1)).

3.4 Principal corrections for the accuracy improvements

3.4.1 Delta-N method

The *discrete ordinate method* used to solve the equation (3.12), approximate the integral term by a finite sum that is usually of the same order ($2N$) as the number of terms necessary to get a good Legendre polynomial representation of the phase function. For the strongly forward-peaked scattering, an accurate expansion of the phase function may require several hundred terms. This may lead to a large system of equations that requires such inordinate amounts of computer storage space and time as to render the solution impractical even on modern computers.
To circumvent this numerical difficulty, scaling transformations have been introduced. The motivation for scaling in this case is to transform a transfer

equation with a strongly peaked phase function into a more tractable problem with a phase function that is much less anisotropic. Considering that the forward scattering peak takes on the resemblance of a Dirac δ function when plotted versus cosine of the scattering angle, this suggest that it would be useful to treat photons scattered within the sharp forward peak as unscattered, and truncate this peak from the phase function. Assuming that the forward-scattering peak can be represented by a Dirac δ function, while the remainder of the phase function is expanded in Legendre polynomials we have:

$$\hat{p}_{p,\delta-N}(\mu_s) = \hat{p}_{p,\delta-N}(\mu', \phi'; \mu, \phi) \tag{3.43}$$

$$= 2f_p\delta(1-\mu_s) + (1-f_p)\sum_{l=0}^{2N-1}(2l+1)\hat{\chi}_{l,p}P_l(\mu_s) \tag{3.44}$$

$$= 4\pi\delta(\mu'-\mu)\delta(\phi'-\phi) + (1-f_p)\sum_{l=0}^{2N-1}(2l+1)\hat{\chi}_{l,p} \tag{3.45}$$

$$\times \sum_{m=0}^{l}\Lambda_l^m(\mu`)\Lambda_l^m(\mu)\cos m(\phi` - \phi) \tag{3.46}$$

where f_p $(0 \leq f_p \leq 1)$ is the *truncation factor* in layer p (dimensionless parameter). As described above this method treat the forward scattering as unscattered; this means that the optical depth and other optical properties will be reduced. It can be shown that [*Levoni et al., 1999*]:

$$\hat{\omega}_p = \omega_p\frac{(1-f_p)}{(1-\omega_p f_p)} \tag{3.47}$$

$$\hat{\tau}_p = \tau_p(1-\omega_p f_p) \tag{3.48}$$

$$\hat{\chi}_{l,p} = \frac{\chi_{l,p} - f_p}{1-f_p} \tag{3.49}$$

where:

$f_p = \chi_{2N,p}$

If $f_p = 0$ we retain the usual Legendre polynomial expansion, $\hat{\chi}_{l,p} \equiv \chi_{l,p}$, $\hat{\tau}_p = \tau_p$ and $\hat{\chi}_{l,p} = \chi_{l,p}$.

3.4.2 Nakajima-Tanaka procedure

The accuracy of the intensity computation is generally improved by the use of the $\delta - M$ except in the forward direction. For more strongly forward-peaked phase function the error incurred becomes unacceptable for practical purposes.

It can be shown that the solution of the radiative transfer equation (3.12) may be written in terms of a contribution due to multiple scattering and a contribution of single scattering. The computation of the single scattering term is likely to be inaccurate with a low number of streams, since a lot of phase function information is lost in the truncation. Considering that it can be shown that is easy to derive the exact solution for the single scattered intensity field, a single scatter correction can be replaced by the exact computation which retains an accurate description of the phase function.

Chapter 4

The Optimal Estimation inversion technique

In this Chapter the Optimal Estimation inversion technique used for the retrieval and error assessment will be described. The information content procedure, the error assessment and the inversion procedure implemented together with the *forward model* (see Chapter (5)) will constitute the procedure used to understand the effectiveness of the aerosol extinction profile retrieval from passive satellite measurements (see Chapter (6)).

4.1 Introduction to the Optimal Estimation inversion theory

When a satellite measurements of Earth's atmosphere is made, the radiation that reach the instrument is a more or less complicated function of atmospheric parameters. Given such parameters, the TOA intensity can be modeled with a Radiative Transfer Model (RTM); the inverse process to obtain the parameters value from the measurements is often more complicated and need a specific inversion theory: "*the inverse problem is the question of finding the best representation of the required parameter given the measurements made, together with any appropriate prior information that may be available about the system and the measuring device.*" *[Rodgers, 2000].* The utilization of the *a-priori* information is the main characteristic of the

Optimal Estimation (*OE*) inversion method, used in this work, where the linear inversion step is based on Bayes' theorem for the determination of the posterior probability density function. The *OE* is able to describe the information content of the measurements, the relationship between the true state of the system and that retrieved using inverse methods and to give an accurate error analysis of many parameters involved in the retrieval.
The following description of the *OE* techniques derive entirely from work of *Rodgers [2000]* and represents only an overview of the principal concepts and quantities. In the second part of the Chapter will be described the parameters setting for the *aerosol extinction coefficient profile* retrieval and error assessment, that represents the aim of work.

4.2 The Inverse Problem

The general inverse problem can be regarded as a question of setting up and solving a set of simultaneous linear or non-linear equations, in the presence of experimental error in some of the parameters (the "measurements"). To examine the information content of the indirect measurements, we will consider the measurement assembled into a vector $\mathbf{y}$, the *measurements vector*, and the unknowns into a *state vector* $\mathbf{x}$, describing the state of the atmosphere. The transformation from the *state vector* space (*state space*) into the *measurements vector* space (*measurements space*), is giving by the *forward model* that describes the physics of the process.

4.2.1 State and Measurements vectors

As described before the quantities to be retrieved can be represented by a state vector $\mathbf{x}$ having n elements:

$$\mathbf{x} = [x_1; x_2; \ldots; x_n] \tag{4.1}$$

In this work the *state vector* is the profile of the *aerosol extinction coefficient* at 550 *nm* and the elements are the *aerosol extinction coefficient* values at

different altitudes.

The quantities measured in order to retrieve $\mathbf{x}$ are the the *measurements vector* $\mathbf{y}$, having m elements:

$$y = [y_1; y_2; \ldots; y_m] \tag{4.2}$$

4.2.2 Forward Model and Linearization

In an ideal case for each *state vector* $\mathbf{x}$ there is a corresponding *measurements vector* $\mathbf{y_I}$ described by a *forward function* $f(\mathbf{x})$:

$$\mathbf{y_I} = f(\mathbf{x}) \tag{4.3}$$

In practice, the detailed physics of the *forward function* is approximate by a *forward model* $\mathbf{F(x)}$ and an experimental error may occur, so the (4.3) becomes:

$$\mathbf{y} = \mathbf{F}(\mathbf{x}) + \epsilon \tag{4.4}$$

where ϵ is the *measurements error* vector, having m elements.

The quantities to be retrieved in most inverse problems are continuous functions, while the measurements are always of discrete quantities. Thus most inverse problems are formally ill-posed or undercostrained. This is simply dealt with by replacing the truly continuous state function, corresponding to an infinite number of parameters with a representation in terms of a finite number of parameters.

For the examination of the information content and the development of an inversion procedure is necessary linearize the forward model about some reference state $\mathbf{x_0}$:

$$\mathbf{y} - \mathbf{F}(\mathbf{x_0}) = \frac{\partial \mathbf{F}(\mathbf{x})}{\partial \mathbf{x}}(\mathbf{x} - \mathbf{x_0}) + \epsilon = \mathbf{K}(\mathbf{x} - \mathbf{x_0}) + \epsilon \tag{4.5}$$

where $\mathbf{K}$ is the *weighting function* matrix of dimension $m \times n$. Each element of $\mathbf{K}$ is the partial derivative of a *forward model* element with respect to a state vector element:

$$\mathbf{K_{i,j}} = \frac{\partial \mathbf{F_i}(\mathbf{x})}{\partial \mathbf{x_j}} \tag{4.6}$$

$$\forall i = 1, \ldots, m$$

$$\forall j = 1, \ldots, n$$

If $m < n$ the problem is undercostrained (or ill-posed) (fewer measures than unknowns); if $m > n$ the problem is overcostrained (more measures than unknowns); if $m = n$ the problem is wellcostrained (number of measures equals to number of unknowns).

4.2.3 Statistical description of experimental errors

All real measurements are subject to uncertainties that are generally described in terms of *probability density functions (pdf)*. The statement that a scalar measurements has a value $\hat{y}$ and an error σ is a shorthand way of saying that our knowledge of the true value of the measured parameter is described by a *pdf* $P(y)$ with expectation value $\hat{y}$ and variance σ^2:

$$\hat{y} = \int yP(y)dy \tag{4.7}$$

$$\sigma^2 = \int (y - \hat{y})^2 P(y)dy \tag{4.8}$$

The probability that y lies in $(y, y + dy)$ is $P(y)dy$.
Considering a Gaussian distribution for the *pdf*:

$$P(y) = \frac{1}{(2\pi)^{1/2}\sigma} exp\left[\frac{1}{2}\left(\frac{y - \hat{y}}{\sigma}\right)^2\right] \tag{4.9}$$

When the measured quantity is a vector $\mathbf{y}$ the mean value is computed element by element. In analogy to (4.7), we obtain:

$$\hat{\mathbf{y}} = \int \mathbf{y}P(\mathbf{y})d\mathbf{y} \tag{4.10}$$

where $P(\mathbf{y})$ is the *pdf* of the vector.
Let $\mathbf{S}$ the covariance matrix, i.e. the multi-dimensional generalization of the variance. Its elements S_{ij} are defined by:

$$S_{ij} = \Gamma\{(y_i - \hat{y_i})(y_j - \hat{y_j})\} = c_{i,j}\sigma_i\sigma_y \tag{4.11}$$

where Γ is the *expected value operator* and the $c_{i,j}$ are the *linear correlation coefficients* between the elements ($c_{i,j} = 1$ for $i = j$ and $c_{i,j} \in [0, 1]$ otherwise). The diagonal elements are the variances of the individual elements of $\mathbf{y}$.

The Gaussian distribution for a vector assume the form:

$$P(\mathbf{y}) = \frac{1}{(2\pi)^{n/2} \mid \mathbf{S_y} \mid^{\mathbf{1/2}}} exp\left\{-\frac{1}{2}(\mathbf{y} - \hat{\mathbf{y}})^T \mathbf{S_y^{-1}} (\mathbf{y} - \hat{\mathbf{y}})\right\} \tag{4.12}$$

where $\mid \mathbf{S_y} \mid$ represents the determinant of $\mathbf{S_y}$ that must be non-singular.

4.2.3.1 Bayesian approach

As described before, the act of measurement map the state into the measurement space according to the forward model (see equation (4.4)). Conversely, a given measurements, could be the result of a mapping from anywhere in the state space. For this reason it's necessary have some prior information about the state, which can be used to constrain the solution. The Bayesian approach is a method able to resolve the noisy inverse problem, in which we have some prior understanding or expectation about some quantity, and want to update the understanding in the light of new information.

Defining:

- $P(\mathbf{x})$ as the *prior pdf* of the state $\mathbf{x}$ ($P(\mathbf{x})d\mathbf{x}$ represents our knowledge of $\mathbf{x}$ before the measurements is made, it's the probability, before the measurements, that $\mathbf{x}$ lies in the multidimensional space ($\mathbf{x}$, $\mathbf{x}$ + d$\mathbf{x}$));
- $P(\mathbf{y})$ as the *prior pdf* of the measurements $\mathbf{y}$;
- $P(\mathbf{y} \mid \mathbf{x})$ as the *conditional pdf* of $\mathbf{y}$ given $\mathbf{x}$ ($P(\mathbf{y} \mid \mathbf{x})d\mathbf{y}$ is the probability that $\mathbf{y}$ lies in ($\mathbf{y}$, $\mathbf{y}$ + d$\mathbf{y}$) when $\mathbf{x}$ has a given value);
- $P(\mathbf{x} \mid \mathbf{y})$ as the *conditional pdf* of $\mathbf{x}$ given $\mathbf{y}$ ($P(\mathbf{x} \mid \mathbf{y})d\mathbf{x}$ is the probability that $\mathbf{x}$ lies in ($\mathbf{x}$, $\mathbf{x}$ + d$\mathbf{x}$) when $\mathbf{y}$ has a given value). This term is called *posterior pdf* and it's the quantity of interests for solving the inverse problem.

It can be shown that:

$$P(\mathbf{x} \mid \mathbf{y}) = \frac{P(\mathbf{y} \mid \mathbf{x})P(\mathbf{x})}{P(\mathbf{y})} \tag{4.13}$$

The equation (4.13) is the Bayes' theorem; it shows that having a *prior* information about the state vector ($P(\mathbf{x})$) and a *forward model* which maps the *state space* into the *measurement space* ($P(\mathbf{y} \mid \mathbf{x})$), the Bayesian theorem provides a formalism to invert this mapping and calculate the *posterior pdf*.

4.2.3.2 The Linear problem solution

Considering a linear problem (linear *forward model*) in which all the *pdf*'s are Gaussian, i.e. applying the equation (4.12) at the different terms of (4.13), the Bayesian theorem gives:

$$-2lnP(\mathbf{x} \mid \mathbf{y}) = (\mathbf{y} - \mathbf{Kx})^{\mathbf{T}}\mathbf{S}_{\epsilon}^{-\mathbf{1}}(\mathbf{y} - \mathbf{Kx}) + (\mathbf{x} - \mathbf{x_a})^{\mathbf{T}}\mathbf{S}_{\mathbf{a}}^{-\mathbf{1}}(\mathbf{x} - \mathbf{x_a}) + \mathbf{c_1} \tag{4.14}$$

where:

$\mathbf{S}_{\epsilon}$ is the *measurement covariance* matrix (the diagonal elements are the variances of $\mathbf{y}$ ($\sigma_{\epsilon}{}^2$));

$\mathbf{x_a}$ is the *a-priori* state vector;

$\mathbf{S_a}$ is the *a-priori covariance* matrix (the diagonal elements are the variances of $\mathbf{x_a}$ ($\sigma_{\mathbf{a}}{}^2$));

$\mathbf{c_1}$ is a constant.

This is a quadratic form in $\mathbf{x}$, so it must be possible to write it as:

$$-2lnP(\mathbf{x} \mid \mathbf{y}) = (\mathbf{x} - \hat{\mathbf{x}})^{\mathbf{T}}\hat{\mathbf{S}}^{-\mathbf{1}}(\mathbf{x} - \hat{\mathbf{x}}) + \mathbf{c_2} \tag{4.15}$$

i.e. the *posterior pdf* is also Gaussian distribution with *expected value* $\hat{\mathbf{x}}$ and covariance $\hat{\mathbf{S}}$. Relating equation (4.14) to equation (4.15) by equating like terms we obtain:

$$\hat{\mathbf{x}} = \mathbf{x_a} + \hat{\mathbf{S}}\mathbf{K}^{\mathbf{T}}\mathbf{S}_{\epsilon}^{-\mathbf{1}}(\mathbf{y} - \mathbf{Kx_a}) \tag{4.16}$$

where:

$\hat{\mathbf{x}}$ is the *expected value* of state vector $\mathbf{x}$;

$\hat{\mathbf{S}}$ is the *posterior covariance* matrix (the diagonal elements are the variances of $\hat{\mathbf{x}}$), giving by:

$$\hat{\mathbf{S}} = (\mathbf{K}^{\mathbf{T}}\mathbf{S}_{\epsilon}^{-\mathbf{1}}\mathbf{K} + \mathbf{S}_{\mathbf{a}}^{-\mathbf{1}})^{-\mathbf{1}} \tag{4.17}$$

As shown in the equations (4.16) and (4.17), the Bayesian solution of the inverse problem is the Gaussian *pdf* of which $\hat{\mathbf{x}}$ is the *expected value* and $\hat{\mathbf{S}}$ the *covariance*.

4.3 Error analysis

For any remote measurement, the quantity measured, $\mathbf{y}$, is some vector valued function $\mathbf{f}$ of the unknown state vector $\mathbf{x}$, and of some other set of parameters $\mathbf{b}$ that we have decided not to include in the state vector. There is also an experimental error term ϵ. Generalizing the equation (4.4) we obtain:

$$\mathbf{y} = \mathbf{f}(\mathbf{x}, \mathbf{b}) + \epsilon \tag{4.18}$$

where the *forward function* $\mathbf{f}$ describes the complete physics of the measurements. The vector of parameters $\mathbf{b}$ comprises those quantities which influence the measurement, are known to some accuracy, but are not intended as quantities to be retrieved. The error term ϵ includes errors from sources such as detector noise, which are not related to the forward function parameters.
Starting from equation (4.18), considering a generic *inverse or retrieval method* $\mathbf{R}$ and taking into account that in the real case the *forward function* is our *forward model*, it can be shown (for details see [*Rodgers, 2000, Chapter* 3]) that the retrieval error has 4 components: *retrieval noise* , *smoothing error*, *forward model parameter error* and *forward model error*. Each component will be described in the following.

4.3.1 Retrieval noise

The *retrieval noise* is the error in the retrieval induced by the uncertainty in the measurements; is defined to be:

$$\epsilon_{\mathbf{m}} = \mathbf{G}\epsilon \tag{4.19}$$

where:
ϵ is the *measurement noise*;

$\mathbf{G}$ is the *gain matrix* that represents the sensitivity of the retrieval ($\mathbf{R}$) to the measurements ($\mathbf{y}$):

$$\mathbf{G} = \partial\mathbf{R}/\partial\mathbf{y} = (\mathbf{K^T S_\epsilon^{-1} K} + \mathbf{S_a^{-1}})^{-1}\mathbf{K^T S_\epsilon^{-1}} \tag{4.20}$$

where $\mathbf{S}_\epsilon$ is the *measurements noise covariance* matrix.
The covariance of the retrieval noise is:

$$\mathbf{S_m} = \mathbf{G S_\epsilon G^T} \tag{4.21}$$

The *retrieval noise* can be considered both systematic or random error.

4.3.2 Smoothing Error

The *smoothing error* represents the way in which the observing system smooth the profile:

$$\epsilon_\mathbf{s} = (\mathbf{A} - \mathbf{I_n})(\mathbf{x} - \mathbf{x_a}) \tag{4.22}$$

where:
$\mathbf{I_n}$ is the unit matrix in *state vector space*;
$\mathbf{x}$ is the true *state vector*;
$\mathbf{A} = \partial\hat{\mathbf{x}}/\partial\mathbf{x} = \mathbf{GK}$, is the sensitivity of the retrieval ($\hat{\mathbf{x}}$) to the true state ($\mathbf{x}$) and is called *averaging kernel* matrix. The rows of $\mathbf{A}$ can be regarded as smoothing functions; in an ideal inverse method, $\mathbf{A}$ would be a unit matrix. In reality, rows of $\mathbf{A}$ are generally peaked functions, peaking at the appropriate level, and with half-width which is a measure of the spatial resolution of the observing system, thus providing a simple characterization of the relationship between the retrieval and the true state. The *averaging kernel* also has an area, which is found to be approximately unity at levels where the retrieval is accurate, and in general can be thought of as a rough measure of the fraction of the retrieval that comes from the data, rather than the *a-priori*.
Since the true state is not known, we must estimate this error contribution using suitable statistics for an ensemble of states. If $\mathbf{x_a}$ and $\mathbf{S_a}$ are the mean

and the covariance of the ensemble, so the *smoothing error covariance* matrix become:

$$\mathbf{S_s} = (\mathbf{A} - \mathbf{I_n})\mathbf{S_a}(\mathbf{A} - \mathbf{I_n})^{\mathbf{T}} \tag{4.23}$$

It is straightforward to show that in the absence of other source of error:

$$\hat{\mathbf{S}} = \mathbf{S_m} + \mathbf{S_s} \tag{4.24}$$

As equation (4.23) shown, to estimate the *smoothing error covariance*, the covariance matrix of a real ensemble of state must be known. It is not enough to simply use ad hoc matrix that has been constructed as a reasonable a priori constrain in the retrieval. If the real covariance is not available, it may be better to abandon the estimation of the smoothing error, and consider the retrieval as an estimate of a smoothed version of the state, rather than an estimate of the complete state.

4.3.3 Forward Model Parameter Error

The *forward model parameter error* is the error in the retrieval due to error in the forward model physical parameters:

$$\epsilon_{\mathbf{f}} = \mathbf{G}\mathbf{K_b}(\mathbf{b} - \hat{\mathbf{b}}) \tag{4.25}$$

where:
$\mathbf{K_b} = \partial\mathbf{F}/\partial\mathbf{b}$ is the weighting function of the parameter $\mathbf{b}$;
$(\mathbf{b} - \hat{\mathbf{b}})$ is the uncertainty of the parameter $\mathbf{b}$.
Assuming that the uncertainties of $\mathbf{b}$ are characterized by Gaussian statistics with error covariance $\mathbf{S_b}$, the *forward model parameter error covariance* matrix becomes:

$$\mathbf{S_f} = \mathbf{G}\mathbf{K_b}\mathbf{S_b}\mathbf{K_b^T}\mathbf{G^T} \tag{4.26}$$

As for *retrieval noise*, the *forward model parameter errors* may contain both systematic or random components.

4.3.4 Forward Model Error

An additional source of error on the profile retrieval arise from approximations made in the forward model itself:

$$\epsilon_{\mathbf{fm}} = \mathbf{G}\boldsymbol{\Delta}\mathbf{F} \tag{4.27}$$

where:
$\boldsymbol{\Delta}\mathbf{F}$ is, for example, the difference between the forward model output using low and high number of streams in the solution of radiative transfer equation. The *forward model errors* are typical case of systematic errors.

4.4 Measurement Information theory

The information theory is a useful instrument to understand, in a simply and fast way, how many independent information can be extract from the measurements and if some measurements are able to improve the knowledge about the quantities that we want to retrieve. This instrument will be used massively in the thesis to understand which is the best configuration (which wavelengths, spectral resolution, geometry, etc.) to obtain the "optimal" state vector with errors as less as possible.

4.4.1 Degrees of freedom

The *Degrees of Freedom for Signal* (*DFS*) represents the number of useful independent quantities there are in a measurements. In other words *DFS* can be interpreted as the number of independent linear combination of the state vector that can be independently retrieved from the measurements.
As shown in equation (4.14), the most probable state in the Gaussian case is the one which minimize:

$$\chi^2 = \epsilon^{\mathbf{T}}\mathbf{S}_{\epsilon}^{-\mathbf{1}}\epsilon + (\mathbf{x} - \mathbf{x_a})^{\mathbf{T}}\mathbf{S}_{\mathbf{a}}^{-\mathbf{1}}(\mathbf{x} - \mathbf{x_a}) \tag{4.28}$$

Equation (4.28) can be divided in two parts, corresponding to the two terms on the right side:

$$d_s = \mathbf{\Gamma}\{(\mathbf{x}-\mathbf{x_a})^{\mathbf{T}}\mathbf{S_a^{-1}}(\mathbf{x}-\mathbf{x_a})\} \tag{4.29}$$

$$d_n = \mathbf{\Gamma}\{\epsilon^{\mathbf{T}}\mathbf{S_\epsilon^{-1}}\epsilon\} \tag{4.30}$$

The equation (4.29) represents first the part of χ^2 attributable to the state vector (*degree of freedom for signal*), while the equation (4.30) is the part of χ^2 attributable to noise (*degree of freedom for noise*).
After some manipulation can be shown [*Rodgers, 2000, Chapter 2*] that:

$$d_s = \sum_{i=1}^{m} \frac{\lambda_i^2}{1+\lambda_i^2} \tag{4.31}$$

where:
λ_i are the *singular values* of $\tilde{K} = S_\epsilon^{-\frac{1}{2}} K S_a^{\frac{1}{2}}$.
If n is the dimension of the state vector, we have $d_s = n$ if the measurements completely determines the state, and $d_s = 0$ if there is no information at all in the measurements.

4.4.2 Shannon information content

The *information content* (H) of a measurement can be defined qualitatively as the factor by which knowledge of a quantity is improved by making the measurements. In the Shannon sense considered here [*Shannon and Weaver, 1949*], it depends on the *entropy* of the probability density function ($S[P(\xi)]$) (which is very closely related to the thermodynamic entropy) defined as follows:

$$S[P(\xi)] = -\int P(\xi) ln(P(\xi)) d\xi \tag{4.32}$$

The *information content* is defined by the difference between the entropy of the *prior covariance* $S(P(\mathbf{x}))$ and the entropy of the *posterior covariance* $S(P(\mathbf{x} \mid \mathbf{y}))$:

$$H = S[P(\mathbf{x})] - S[P(\mathbf{x} \mid \mathbf{y})] \tag{4.33}$$

Considering the Gaussian *pdf* distribution and combining equations (4.32) and (4.33), it can be shown that the information content become:

$$H = \frac{1}{2}\sum_{i=1}^{m} ln(1+\lambda_i^2) \tag{4.34}$$

If $H = 0$ the measurement don't improve the knowledge of the quantity to be retrieved; if $H > 0$ the entropy of the *posterior covariance* is less than the entropy of the *prior covariance*, so after the measurements the system is less chaotic, i.e. the measurements has improve the knowledge of the system.

4.5 Inversion iterative Method

Until now, all the consideration developed has been done considering linear forward models. However, often, in the atmospheric retrieval, the forward models are non-linear, so, is necessary extend the previous consideration to this case, that is also the case of the problem considered in this work. The formalism developed for linear forward model can be extended to yield valid solution for non-linear forward model which behave approximately linearly within the error bounds of the measurements. These forward models are said *moderately non-linear*. The *moderately non-linear* problems are those where the linearization is adequate for the error analysis, but not for finding the solution. The solution must be found numerically and iteratively.

4.5.1 Gauss-Newton Method

The Newtonian iteration is a very useful numerical method for finding the maximum of the *cost function* (see equation (4.14)) if the problem is not too non-linear:

$$\mathbf{x_{i+1}} = \mathbf{x_i} - [\nabla \mathbf{g}(\mathbf{x_i})]^{-\mathbf{1}}\mathbf{g}(\mathbf{x_i}) \tag{4.35}$$

where $g(x_i)$ is the derivative of the *cost function*.
Considering the equation (4.14) and substituting its prime and second derivative to equation (4.35) we obtain:

$$\mathbf{x_{i+1}} = \mathbf{x_a} + (\mathbf{K_i^T S_\epsilon^{-1} K_i} + \mathbf{S_a^{-1}})^{-\mathbf{1}}\mathbf{K_i^T S_\epsilon^{-1}}[\mathbf{y} - \mathbf{y_i} + \mathbf{K_i}(\mathbf{x_i} - \mathbf{x_a})] \tag{4.36}$$

where

$\mathbf{K_i}$ is the weighting function for the $i-th$ iteration;

$\mathbf{y_i} = \mathbf{F}(\mathbf{x_i})$ is the simulated measurements for the $i-th$ iteration.

For $i = 0$, $\mathbf{x_0} \equiv \mathbf{x_a}$.

The iteration process end when a particular convergence criteria is satisfied.

See Paragraph (5.3) for detail about the convergence criteria adopted.

Chapter 5

Forward Model development, validation and inversion procedure implementation

As mentioned in Chapter (2), the *forward model* developed (called AerLIDORT) is based on LIDORT code for the solution of the radiative transfer equation. In the first part of this Chapter will be described all the user defined atmospheric process (Paragraph (5.2.2.1)) and the principal implemented subroutines (Paragraph (5.1.4)) for the TOA *intensity* and *weighting functions* computations. The second part of the Chapter (Paragraph (5.2)) will concern the *forward model* validation using SCIATRAN RTM. The third part will concern the iterative inversion procedure development.

5.1 AerLIDORT Atmospheric Optical Properties

In the *forward model* has been implemented the possibility to set a user defined numbers of layers and thickness. For each layer, temperature, pressure, molecular and aerosol optical properties (see Paragraph 5.1.1 and 5.1.2, respectively) are introduced. The spectral albedo for different surfaces is considered lambertian (see Paragraph 5.1.3).
In the model the aerosol stratification has been introduced, i.e. the possibility

to put different aerosol classes at different altitudes has been implemented. In the following is shown the procedures to compute the optical properties of molecules and aerosol for each atmospheric layer.

5.1.1 Molecules

As shown in Paragraph (3.2.1) the molecular atmospheric input to introduce in LIDORT code are:
molecular extinction coefficients ($e^{Ray}_{p,\lambda}$):

$$e^{Ray}_{p,\lambda} = \alpha_{p,\lambda} + \sigma^{Ray}_{p,\lambda} \tag{5.1}$$

where:
$\alpha_{p,\lambda}$ is the *molecular absorption coefficient*;
$\sigma^{Ray}_{p,\lambda}$ is the *molecular scattering coefficient*.
molecular single scattering albedo ($\omega^{Ray}_{s,p,\lambda}$):

$$\omega^{Ray}_{p,\lambda} = \frac{\sigma^{Ray}_{p,\lambda}}{e_{p,\lambda}} \tag{5.2}$$

where:
$e_{p,\lambda}$ is the *total extinction coefficient*.
molecular phase function ($p_{R,p}$).
In the following each term will be described separately.

5.1.1.1 Absorption

The absorbing molecule introduced into the model is the oxygen ($A-band$, from 755 to 775 nm). The *molecular absorption coefficients* is computed, for each layer, giving the *cross section* and the *volume mixing ratio* ($\Phi_{o_2,p}$) extract from SCIATRAN RTM databases [*Rozanov et al.,* 1997]; for definition:

$$\Phi_{o_2,p} = \frac{P_{o_2,p}}{P_p} 10^6 \tag{5.3}$$

where:
$P_{o_2,p}$ is the partial pressure of the oxygen in layer p;

P_p is the layer p total pressure.

Considering the gas state equation, after straightforward manipulation, the (5.3) becomes:

$$\Phi_{o_2,p} = \rho_{o_2,p}\frac{10^6 RT_p}{\Upsilon_{o_2,p}P_p} \tag{5.4}$$

then:

$$\rho_{o_2,p} = \frac{\Phi_{o_2,p}\Upsilon_{o_2,p}P_p}{10^6 RT_p} \tag{5.5}$$

where:

$\rho_{o_2,p}$ $[g/m^3]$ is the molecular density of oxygen in layer p;

R is the Universal gas constant $(= 8.319 \cdot 10^4[\frac{mbar \cdot cm^3}{K \cdot mol}])$;

T_p [K]is the temperature of layer p;

$\Upsilon_{o_2,p}$ is the molecular weight of oxygen in layer p.

The *molecular absorption coefficient* $(\alpha^{Ray}_{o_2,p})$ is giving by:

$$\alpha_{o_2,p,\lambda} = \alpha^{abs}_{o_2,p,\lambda}\rho_{o_2,p} \tag{5.6}$$

where $\alpha^{abs}_{o_2,p,\lambda}$ $([cm^2/molecules])$ is the *specific absorption cross sections* of oxygen in layer p. The oxygen (*A-band*) *specific absorption cross sections* database, introduced in the model, has been extract from the ESFT (Exponential Sum Fitting of Transmission (ESFT) technique) SCIATRAN database [*Buchwitz et al., 1998*]. The database contains the cross section values from 755.025 to 775.025 nm, step 0.05 nm, for 10 pressure values (0.01, 1, 10, 100, 300, 500, 700, 900, 1000, 1050 hPa) and 5 temperature values (160, 210, 250, 275, 300, 330 K); the *specific absorption cross sections* for layer p, with temperature T_p and pressure P_p, is computed by bi-linear interpolation.

Substituting the (5.5) into the (5.6), and after some manipulations, the *molecular absorption coefficient* $[km^{-1}]$ becomes:

$$\alpha_{o_2,p,\lambda} = \frac{\alpha^{abs}_{o_2,p,\lambda}\Phi_{o_2,p}P_p A}{RT_p}0.1 \tag{5.7}$$

where:

A is the Avogadro number $(6.023 \cdot 10^{23}\ molecules/mol)$.

5.1.1.2 Rayleigh scattering

The *Rayleigh scattering cross section* (σ_λ^{scatt}) is giving by (see, for example [$Kondratyev, 1969$]):

$$\sigma_\lambda^{scatt}(\lambda) = \frac{32\pi^3(n-1)^2}{3N_0^2\lambda^4} \tag{5.8}$$

where:

n is the *refractive index*;

N_0 is the *Loschmidt's number* ($= 2.686763 \cdot 10^{19}\ cm^{-3}$).

To take into account the molecules anisotropy, the *depolarization factor* has been considered. The scattering of light by anisotropic molecules was treated for the first time by Cabannes [1921] who showed that for 90° *scattering angle* the anisotropic molecules scatter more light than isotropic, giving the same *refractive index*. In 1923 King [1923] introduced the correction for total scattering:

$$F_\lambda = \frac{(6+3d_\lambda)}{6-7d_\lambda} \tag{5.9}$$

where:

F_λ is the *King correction factor*;

$d_\lambda = [(I_\parallel^{(s)}(\lambda))/(I_\perp^{(s)}(\lambda))]_{\theta_s=90^\circ}$ is the *depolarization factor*, $I_\parallel^{(s)}(\lambda)$ and $I_\perp^{(s)}(\lambda)$ are, respectively, the horizontal and vertical polarized components of scattered light and θ_s is the *scattering angle*.

Taking into account the *King factor*, the *Rayleigh scattering cross section* becomes:

$$\sigma_\lambda^{scatt*} = \frac{32\pi^3(n-1)^2F_\lambda}{3N_0^2\lambda^4} \tag{5.10}$$

The *Rayleigh cross section* shown in equation 5.10 is reproduced to 0.3% rms (worst case 0.5%) over the full 0.2 - 1 μm range by the expression [*Chance,* 1997]:

$$\sigma_\lambda^{scatt*} = \frac{3.993 \cdot 10^{-4}\beta^4}{1 - 1.069 \cdot 10^{-2}\beta^2 - 6.681 \cdot 10^{-5}\beta^4} \tag{5.11}$$

where $\beta(\mu m^{-1}) = \frac{1}{\lambda(\mu m)}$ and $[\sigma^{scatt*}] = cm^2$.

The *Rayleigh scattering coefficients* for each layer (σ_p^{Ray}, $[km^{-1}]$) is computed

by multiplying the *scattering cross section* and the layer *air density* (ρ_p^{air}) (see [Bodhaine, 1999]):

$$\sigma_{p,\lambda}^{Ray} = 10^5 \sigma_\lambda^{scatt*} \rho_p^{air} \tag{5.12}$$

where:
$\rho_p^{air} = (P_p A)/(RT_p)$ $[molecules/cm^3]$ and 10^5 is the conversion factor from cm^{-1} to km^{-1}.

5.1.1.3 Rayleigh Phase Function

The scattering of light by molecules is similar to that of an induced dipolar oscillator. The classical model, that fit observations quite well, considers the (unpolarized) incident wave to induce a motion of the bound electrons, which is in phase with the wave. Its interaction with an unpolarized wave results in the molecule extracting energy from the wave and then re-radiating it in all directions. Taking into account the anisotropy of molecules, also the angular distribution of Rayleigh scattered light is influenced. An accurate formula was proposed by Chandrasekhar [1960]:

$$p_{Ray,\lambda}(\mu_s) = \frac{3}{4(1+2\gamma)}[(1+3\gamma) + (1-\gamma)\mu_s^2] \tag{5.13}$$

where: $\gamma = (d_\lambda)/(2-d_\lambda)$.
Considering the equation (5.13) and (3.5) it is possible compute the *Legendre moments* of the *phase function*:

$$\chi_{0,\lambda} = \frac{1}{2}\int_{-1}^{1} P_0(\mu_s) p_{Ray,\lambda}(\mu_s) d\mu_s \tag{5.14}$$

$$= \frac{1}{2}\int_{-1}^{1} \frac{3}{4(1+2\gamma)}[(1+3\gamma) + (1-\gamma)\mu_s^2] d\mu_s = 1 \tag{5.15}$$

$$\chi_{1,\lambda} = \frac{1}{2}\int_{-1}^{1} P_1(\mu_s) p_{Ray,\lambda}(\mu_s) d\mu_s \tag{5.16}$$

$$= \frac{1}{2}\int_{-1}^{1} \mu_s \frac{3}{4(1+2\gamma)}[(1+3\gamma)+(1-\gamma)\mu_s^2]d\mu_s = 0 \tag{5.17}$$

$$\chi_{2,\lambda} = \frac{1}{2}\int_{-1}^{1} P_2(\mu_s) p_{Ray,\lambda}(\mu_s) d\mu_s \tag{5.18}$$

$$= \frac{1}{2}\int_{-1}^{1} \frac{1}{2}(3\mu_s^2 - 1)\frac{3}{4(1+2\gamma)}[(1+3\gamma)+(1-\gamma)\mu_s^2]d\mu_s \tag{5.19}$$

$$= \frac{1}{10}\frac{(1-\gamma)}{(1+2\gamma)} = \frac{1}{5}\frac{(1-d_\lambda)}{(2+d_\lambda))} \tag{5.20}$$

where $P_l(\mu_s)$, for $l = 0, 1, 2$, are the *Legendre polynomials*.
It could be shown that $\forall\ l \geq 2$, $\chi_{l,\lambda} = 0$.
Applying the equation (3.4) the Rayleigh phase function becomes:

$$p_{Ray,\lambda}(\mu_s) = 1 + \frac{(1-d_\lambda))}{(2+d_\lambda))} P_2(\mu_s) \tag{5.21}$$

The *depolarization factor* is computed from equation (5.9):

$$d_\lambda = 6\frac{F_\lambda - 1}{3 + 7F_\lambda} \tag{5.22}$$

where the *King factor* (F_k) is obtained by an empirical formula derived from Bates data [*Bates, 1984*] by Chance:

$$F_\lambda = 1.0469541 + \beta^2 3.250315310^{-4} + \beta^4 3.862285110^{-5} \tag{5.23}$$

where $\beta = \frac{1}{\lambda}$

5.1.2 Aerosol

As in the case of molecules, the aerosol optical properties to introduce are:
aerosol extinction coefficient ($e^{Aer}_{p,\lambda}$):

$$e^{Aer}_{p,\lambda} = e^{Aer}_{p,550}\frac{k_\lambda}{k_{550}} \tag{5.24}$$

where:
$e^{Aer}_{p,550}$ $[km^{-1}]$ is the reference *aerosol extinction coefficient* profile at 550 nm wavelength;
k_{550} $[km^{-1}/cm^3]$ is the *specific aerosol extinction coefficients* at 550 nm;
k_λ $[km^{-1}/cm^3]$ is the *specific aerosol extinction coefficients* at wavelength λ.
aerosol single scattering albedo ($\omega^{Aer}_{p,\lambda}$):

$$\omega^{Aer}_{p,\lambda} = \frac{\sigma^{Aer}_{p,\lambda}}{e_{p,\lambda}} = \frac{e^{Aer}_{p,\lambda}\Omega^{Aer}_{\lambda}}{e_{p,\lambda}} \tag{5.25}$$

where:
$\sigma^{Aer}_{p,\lambda}$ $[km^{-1}]$ is the *aerosol scattering coefficient*;
Ω^{Aer}_{λ} is the *specific single scattering albedo.*
aerosol phase function (p^{Aer}_{p}).
In the model are been inserted 8 aerosol classes: *maritime, volcanic, desertic, biomass burning, background stratospheric, urban, average continental* and *rural*. The aerosol optical spectral properties (*specific extinction coefficient, specific single scattering albedo, asymmetry factor, phase function and Legendre moments*) for each class derive from Levoni [*Levoni* et. al 1997] database. In the model has been implemented also the aerosol stratification, giving the possibility, to select different class of aerosol at different altitudes.

5.1.2.1 Aerosol Phase Function

Two kinds of aerosol *phase functions* has been introduced: the analytic *Henyey-Greenstein phase function* and the *Mie phase function* that can be reconstructed from the *Legendre moments*. In latter case the equation (3.4) is directly applying and the *Legendre moments* are extract from the

aerosol database, computed considering the micro physical properties of aerosol classes and applying the Mie theory. The "*Mie*" *phase functions* represents the better approximation of the real phase function. In Figure (5.1) are shown some *Mie phase functions* for different aerosol classes at 500 *nm*, varying the *scattering angle*.

In the processing operation the use of the *Mie phase functions* involve greater processing time, but in many cases the use of a approximate description (as *Henyey-Greenstein phase function* is), should carry out a not negligible errors in the atmospheric representation and then in the retrieval. In Figure (5.2) are shown the comparison between the Mie phase function and the Henyey-Greenstein phase function for *maritime* aerosol at 500 *nm*, varying the scattering angle; as can be noted, in the scattering angle range for nadir sounding, the difference between the two is relevant.

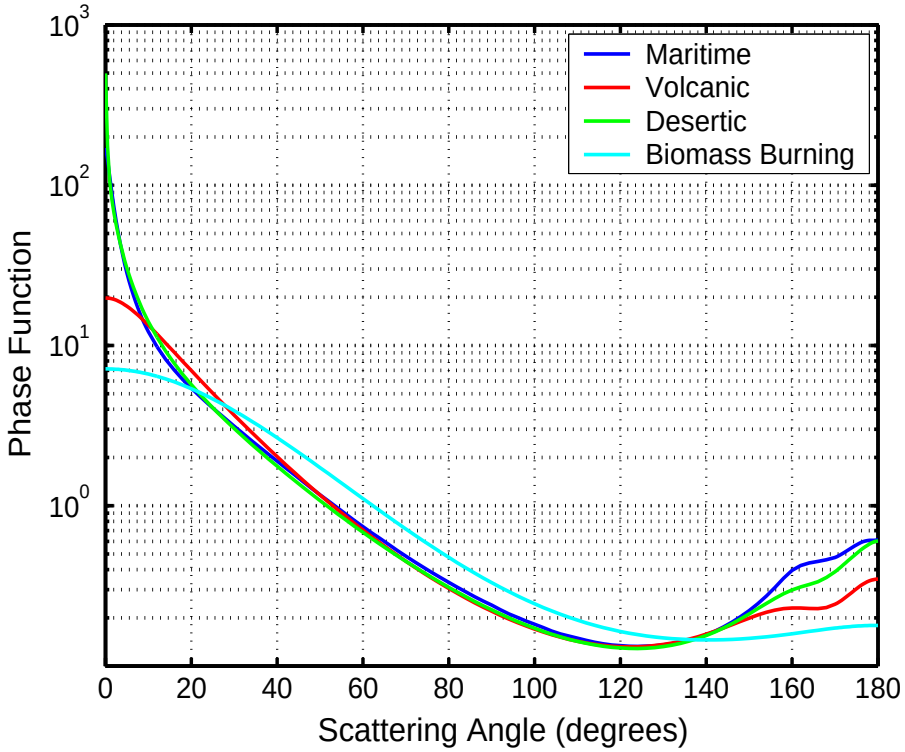

Figure 5.1: Comparison between Mie phase functions for different aerosol classes, at 500 *nm*.

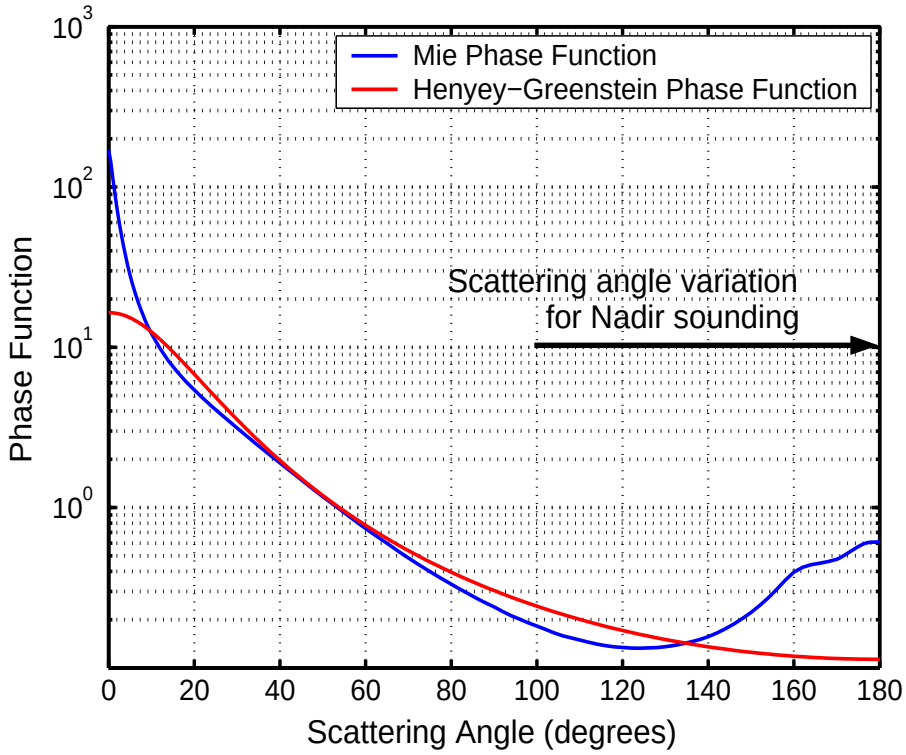

Figure 5.2: Comparison between Mie phase function and Henyey-Greenstein phase function, for maritime aerosol at 500 nm; in figure is also shown the scattering angle range for nadir sounding (100 - 180 degrees).

5.1.2.2 Henyey-Greenstein Phase Function

The Henyey-Greenstein $(H-G)$ *phase function* was proposed by L. Henyey and J. Greenstein in 1941; this function has no physical basis and should be considered as one-parameter analytic fit to an actual phase function:

$$p_{HG,s,\lambda}(\mu_s) = \frac{1 - g_{s,\lambda}^2}{(1 + g_{s,\lambda}^2 - 2g_{s,\lambda}\mu_s)^{3/2}} \tag{5.26}$$

where g_λ is called *asymmetry factor*.

If $g_\lambda = 1$ the *H-G phase function* yields complete forward scattering, isotropic scattering for $g_\lambda = 0$ and complete backward scattering for $g_\lambda = -1$. A remarkable feature of the *H-G function* is the fact that the *Legendre polynomial coefficients* are simply; applying the equation (3.5) it can be shown that:

$$\chi_l = (g_{s,\lambda})^l \tag{5.27}$$

Only the first moments of the *phase function* (i.e. the *asymmetry factor* g, see Paragraph (3.27)) must be specified to obtain the complete *phase function*. Considering the equation (3.4):

$$p_{HG,s,\lambda}(\mu_s) = 1 + 3g_{s,\lambda}P_1(\mu_s) + 5g^2_{s,\lambda}P_2(\mu_s) + 7g^3_{s,\lambda}P_3(\mu_s) + \dots \qquad (5.28)$$

The *asymmetry factor* is extract from aerosol database for each class and wavelength.

5.1.3 Surface Albedo

The *surface spectral albedo* can be set by the user or computed, making a linear interpolation, by the *spectral albedo* database extract from the *GOME Cloud and Aerosol DAta Products Algorithms development (CADAPA)* report [*Guzzi et al., 1998*]. The surfaces considered are: water, soil, sand, vegetation and snow. In Figure (5.3) and Figure (5.4) are shown, respectively, the CADAPA *spectral albedo* for different surfaces in a wide spectral range and in the oxygen $A - band$ spectral range.

5.1.4 AerLIDORT implementation subroutines

The principal subroutines has been implemented to introduce the Sun *irradiance* spectra, to take into account the different distance between Earth and Sun during the year and to compute the convolution with the instrumental slit function.
The solar *irradiance* database has been extract from SCIATRAN and is used to compute the *radiance spectra* (see Paragraph (3.2.1)).
The Earth-Sun correction ($d_{E,S}$) is obtain applying the following relation [from SCIATRAN RTM, *Rozanov et al., 1997*]:

$$\begin{aligned} d_{E,S} = 1.00011 + (0.034221 * cos(\gamma)) + (0.00128 * sin(\gamma)) + \qquad (5.29) \\ +(0.000719 * cos(2.0 * \gamma)) + (0.000077 * sin(2.0 * \gamma)) \end{aligned}$$

where:
$\gamma = 2.0\pi(d - 1.0)/365.0$ and d is the day of the year.

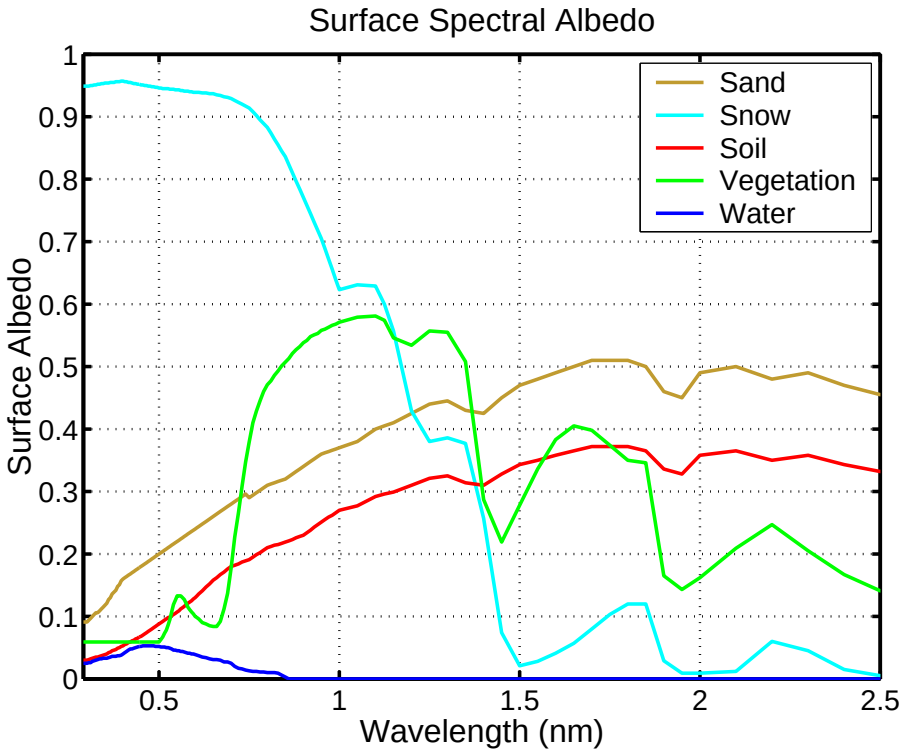

Figure 5.3: Spectral albedo for different surfaces (CADAPA reference).

For the slit function convolution a brief description is presented below.

5.1.4.1 SCIAMACHY slit function convolution

To reproduce the instrument TOA Intensity is necessary convolve the high resolution spectra with the normalized instrument *slit-function*:

$$I_i = \int_0^\infty d\lambda S(\lambda_i, \lambda) I(\lambda) \tag{5.30}$$

where:

I_i is the *i-channel* convoluted TOA Intensity;

$S(\lambda_i, \lambda)$ is the normalized instrument i^{th} channel *slit-function*;

$I(\lambda)$ is the high resolution TOA Intensity.

Considering the linearization of the Forward Model, the *i-channel* weighting function ($K_{i,j}$) become:

$$K_{i,j} = \frac{\partial I_i}{\xi_j} = \int_0^\infty d\lambda S(\lambda_i, \lambda) \frac{\partial I(\lambda)}{\partial \xi_j} \tag{5.31}$$

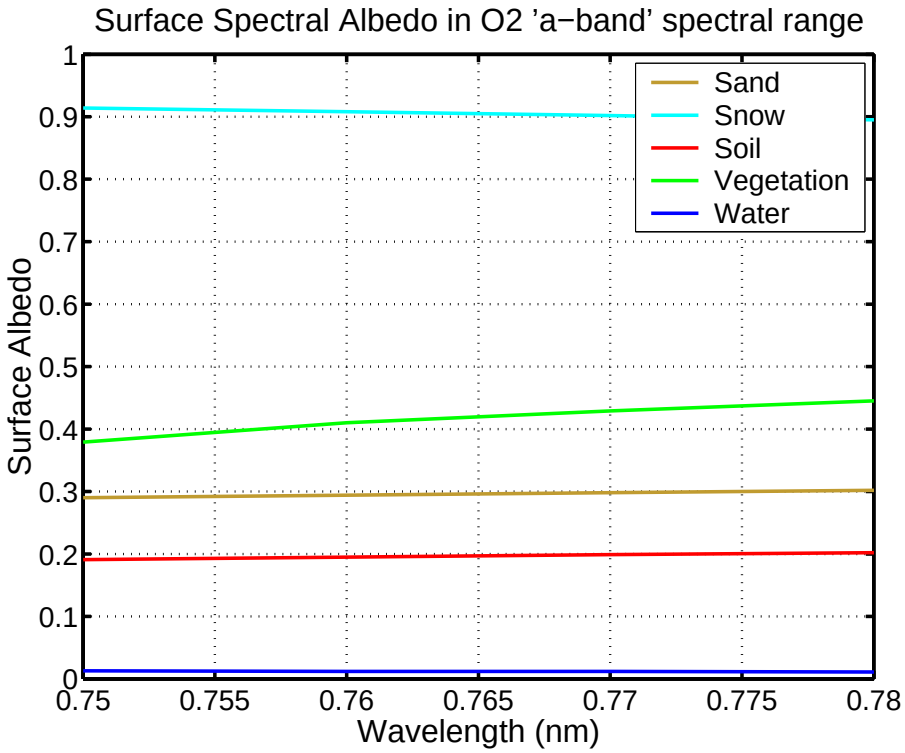

Figure 5.4: Spectral albedo for different surfaces in the oxygen $A-band$ spectral range.

where ξ_j is the j^{th} component of the state vector of parameters to be retrieved. The SCIAMACHY *slit-function* type and the associated Full Width Half Maximum (FWHM) parameter vary with wavelengths (see Paragraph (2.1)). In channel 4, for the oxygen A-band, the employed normalized slit function is a single hyperbolic:

$$S(\lambda_i, \lambda) = \frac{\sqrt{2}}{\pi} \frac{(\frac{FWHM}{2})^3}{(\lambda_i - \lambda)^4 + (\frac{FWHM}{2})^4} \tag{5.32}$$

with $FWHM = 0.4$.

As example, in Figure (5.5) are shown 10 SCIAMACHY single hyperbolic slit function in the oxygen A-*band*, around 762 nm.

5.1.5 Input for Weighting Function computation

As will be shown in the next Chapter, not only the *aerosol extinction coefficient* weighting functions, needed for the retrieval, must be computed. To

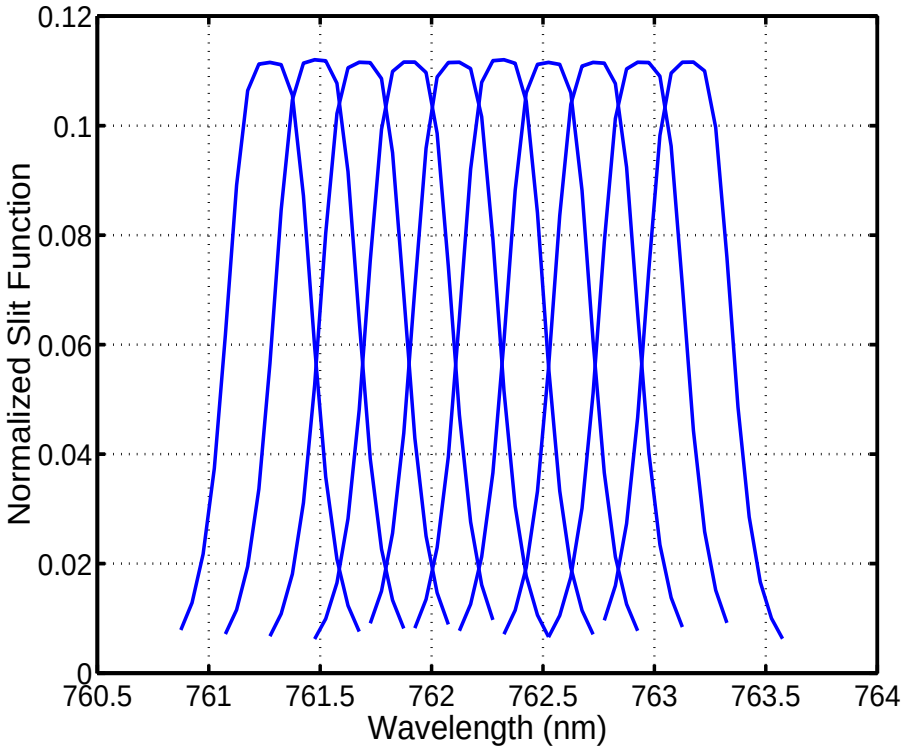

Figure 5.5: SCIAMACHY slit functions around 762 nm.

operate an exhaustive error assessment computation (see Paragraph (4.3)), the weighting functions of different atmospheric parameters, that influence the retrieval itself, has been computed. This parameters are the *aerosol single scattering albedo*, the *aerosol Mie phase function*, the *molecular absorbing coefficient*, the *Rayleigh scattering coefficient* and the *surface albedo*. Except for *surface albedo*, for which the weighting functions are computed automatically from the LIDORT code, for each atmospheric parameter the relative variations terms (see Paragraph (3.3)) must be computed.

Aerosol Extinction Coefficient

Variable: $\xi_p = e_p^{Aer}$

From equation (3.38):

$$u_p = u_p^{Ray} + u_p^{Aer} = \frac{e_p^{Aer}}{\omega_p^{Ray}} \frac{\partial \omega_p^{Ray}}{\partial e_p^{Aer}} + \frac{e_p^{Aer}}{\omega_p^{Aer}} \frac{\partial \omega_p^{Aer}}{\partial e_p^{Aer}} \tag{5.33}$$

Substituting the equation (5.1) and (5.25) into (5.33), after straightforward manipulation we obtain:

$$u_p = -\frac{e_p^{Aer}}{e_p} + \frac{e_p - e_p^{Aer}}{e_p} = \frac{e_p - 2e_p^{Aer}}{e_p} \tag{5.34}$$

From equation (3.39) and substituting the (5.1):

$$v_p = \frac{e_p^{Aer}}{e_p} \frac{\partial e_p}{\partial e_p^{Aer}} = \frac{e_p^{Aer}}{e_p} \tag{5.35}$$

From equation (3.41):

$$z_{l,p} = z_{l,p}^{Ray} + z_{l,p}^{Aer} = \frac{e_p^{Aer}}{\chi_{l,p}^{Ray}} \frac{\partial \chi_{l,p}^{Ray}}{\partial e_p^{Aer}} + \frac{e_p^{Aer}}{\chi_{l,p}^{Aer}} \frac{\partial \chi_{l,p}^{Aer}}{\partial e_p^{Aer}} = 0 \quad (\forall l) \tag{5.36}$$

Aerosol Single Scattering Albedo

Variable: $\xi_p = \omega_p^{Aer}$

$$u_p = u_p^{Ray} + u_p^{Aer} = \frac{\omega_p^{Aer}}{\omega_p^{Ray}} \frac{\partial \omega_p^{Ray}}{\partial \omega_p^{Aer}} + \frac{\omega_p^{Aer}}{\omega_p^{Aer}} \frac{\partial \omega_p^{Aer}}{\partial \omega_p^{Aer}} = 1 \tag{5.37}$$

$$v_p = \frac{\omega_p^{Aer}}{e_p} \frac{\partial e_p}{\partial \omega_p^{Aer}} = 0 \tag{5.38}$$

$$z_{p,l} = z_{p,l}^{Ray} + z_{l,p}^{Aer} = \frac{\omega_p^{Aer}}{\chi_{l,p}^{Ray}} \frac{\partial \chi_{l,p}^{Ray}}{\partial \omega_p^{Aer}} + \frac{\omega_p^{Aer}}{\chi_{l,p}^{Aer}} \frac{\partial \chi_{l,p}^{Aer}}{\partial \omega_p^{Aer}} = 0 \quad (\forall l) \tag{5.39}$$

Aerosol Phase Function

All the simulations for the aerosol extinction coefficient profile retrieval, has been done considering the aerosol Mie phase function. As shown in Paragraph (5.1.2.1), the Mie phase function has been computed from the *Legendre moments* extract from the aerosol database. So aerosol phase function variation has been computed varying its *Legendre moments*.

Variable: $\xi_p = \chi_{l,p}^{Aer}$

$$u_p = u_p^{Ray} + u_p^{Aer} = \frac{\chi_{l,p}^{Aer}}{\omega_p^{Ray}} \frac{\partial \omega_p^{Ray}}{\partial \chi_{l,p}^{Aer}} + \frac{\chi_{l,p}^{Aer}}{\omega_p^{Aer}} \frac{\partial \omega_p^{Aer}}{\partial \chi_{l,p}^{Aer}} = 0 \tag{5.40}$$

$$v_p = \frac{\chi_{l,p}^{Aer}}{e_p} \frac{\partial e_p}{\partial \chi_{l,p}^{Aer}} = 0 \tag{5.41}$$

$$z_{l,p} = z_{l,p}^{Ray} + z_{l,p}^{Aer} = \frac{\chi_{l,p}^{Aer}}{\chi_{l,p}^{Ray}} \frac{\partial \chi_{l,p}^{Ray}}{\partial \chi_{l,p}^{Aer}} + \frac{\chi_{l,p}^{Aer}}{\chi_{l,p}^{Aer}} \frac{\partial \chi_{l,p}^{Aer}}{\partial \chi_{l,p}^{Aer}} = 1 \quad (\forall l) \tag{5.42}$$

Rayleigh Scattering Coefficient

Variable: $\xi_p = \sigma_p^{Ray}$

$$u_p = u_p^{Ray} + u_p^{Aer} = \frac{\sigma_p^{Ray}}{\omega_p^{Ray}} \frac{\partial \omega_p^{Ray}}{\partial \sigma_p^{Ray}} + \frac{\sigma_p^{Ray}}{\omega_p^{Aer}} \frac{\partial \omega_p^{Aer}}{\partial \sigma_p^{Ray}} \tag{5.43}$$

Considering the equations (5.2) and (5.25) the (5.43) becomes:

$$u_p = \frac{e_p - \sigma_p^{Ray}}{e_p} - \frac{\sigma_p^{Ray}}{e_p} = \frac{e_p - 2\sigma_p^{s,Ray}}{e_p} \tag{5.44}$$

$$v_p = \frac{\sigma_p^{Ray}}{e_p} \frac{\partial e_p}{\partial \sigma_p^{Ray}} = \frac{\sigma_p^{Ray}}{e_p} \tag{5.45}$$

$$z_{l,p} = z_{p,l}^{Ray} + z_{l,p}^{Aer} = \frac{\sigma_p^{Ray}}{\chi_{l,p}^{Ray}} \frac{\partial \chi_{l,p}^{Ray}}{\partial \sigma_p^{Ray}} + \frac{\sigma_p^{Ray}}{\chi_{l,p}^{Aer}} \frac{\partial \chi_{l,p}^{Aer}}{\partial \sigma_p^{Ray}} = 0 \quad (\forall l) \tag{5.46}$$

Oxygen absorption Coefficient

Variable: $\xi_p = \alpha_p^{Ray}$

$$u_p = u_p^{Ray} + u_p^{Aer} = \frac{\alpha_p^{Ray}}{\omega_p^{Ray}} \frac{\partial \omega_p^{Ray}}{\partial \alpha_p^{Ray}} + \frac{\alpha_p^{Ray}}{\omega_p^{Aer}} \frac{\partial \omega_p^{Aer}}{\partial \alpha_p^{Ray}} \tag{5.47}$$

Considering the equations (5.2) and (5.25) the (5.43) becomes:

$$u_p = -\frac{\alpha_p^{Ray}}{e_p} - \frac{\alpha_p^{Ray}}{e_p} = -\frac{2\alpha_p^{Ray}}{e_p} \tag{5.48}$$

$$v_p = \frac{\alpha_p^{Ray}}{e_p} \frac{\partial e_p}{\partial \alpha_p^{Ray}} = \frac{\alpha_p^{Ray}}{e_p} \tag{5.49}$$

$$z_{l,p} = z_{p,l}^{Ray} + z_{l,p}^{Aer} = \frac{\alpha_p^{Ray}}{\chi_{l,p}^{Ray}} \frac{\partial \chi_{l,p}^{Ray}}{\partial \alpha_p^{Ray}} + \frac{\sigma_p^{Ray}}{\chi_{l,p}^{Aer}} \frac{\partial \chi_{l,p}^{Aer}}{\partial \alpha_p^{Ray}} = 0 \quad (\forall l) \tag{5.50}$$

5.2 AerLIDORT Validation

The comparison between the *forward model* developed and well known and validated RTM is a fundamental step to assure the goodness of the *forward model* itself. In general this operation is extremely critical because of the enormous number of variables and settings. For example different method for the solution of the radiative transfer equation, different databases of same molecular species or aerosol types, gives different results not easy to compare. In many cases is difficult understand how much a recognize difference between the *forward model* developed and reference RTM is due to a difference in the optical properties of molecules and aerosols, RTE solution method or due to a difference in the relashionship considered to compute the atmospheric parameters. The comparison has been made with RTM $SCIATRAN$ Version 1.2 [*Buchwitz et al., 1998*]; to avoid the uncertainty above briefly described, the molecular and aerosol databases are extract from *SCIATRAN* and insert in *AerLIDORT*. The same atmospheric stratification and the same characteristics for the radiative transfer equation solution (number of streams and Legendre polynomials) has been set.

5.2.1 SCIATRAN RTM

SCIATRAN (an extension of *GOMETRAN* radiative transfer model [*Rozanov et al.,* 1997]) is a radiative transfer program developed at the institute of Remote Sensing and Institute of Environmental Physics at University of Bremen (Germany), designed to allow fast and accurate simulation of radiance spectra as measured from space with the passive remote sensing UV-Vis-NIR spectrometers GOME (Global Ozone Monitoring Experiment) [*Burrows et al.,* 1999] and SCIAMACHY [*Bovesmann et al., 1999*]. *SCIATRAN* works on 240nm - 2400 nm spectral range, several spectral windows can be selected and can be used for the simulation of quantities like TOA radiance and related quantities, e.g., airmass factors and/or *weighting functions*. It consider 14 molecular species; the absorption cross-section of line-absorber depends strongly on wavelength, pressure and temperature and can be calculated from spectroscopic line parameters like line position, line intensity, air-broadened half-width etc. (obtained from, e.g., the HITRAN spectroscopic data base [*Rothman et al.,* 1998]). Two program modes are implemented in order to accurately considered line-absorptions: an accurate line-by-line and a significantly faster correlated-k mode [*Buchwitz et al.,* 1998]. Full multiple scattering treatment (intensity and *weighting functions*) and several single scattering options. Two aerosol parameterization are implemented: the widely used *LOWTRAN 7* aerosol scheme including Henyey-Greenstein phase functions or, alternatively, an aerosol parametrization developed for *GOMETRAN* which has been extended in order to cover the spectral range of SCIAMACHY.

5.2.2 Characteristics of simulations for TOA Intensity and Weighting Functions validations

- *Atmospheric stratification*: from 0 to 60 km, step 1 km, pressure and temperature for *midlatitude summer* standard profile;

- *Surface albedo*: 0 for each wavelength;
- *Reference aerosol extinction coefficient profile*: standard MODTRAN profile, referred to 550 nm, with surface visibility of 23 km (see figure (5.6)) and $AOT = 0.3315$;
- *Aerosol characteristics*: *water soluble* with 0% humidity from SCIATRAN database, Mie phase function;
- *Molecule characteristics*: ESFT for oxygen *A-band* from SCIATRAN database;
- *Characteristics of radiative transfer equation solution*: 20 streams, 40 Legendre polynomials, $Nakajima - Tanaka$ correction, $Delta - M$ method;
- *Geometry*: Solar Zenith Angle (SZA) = 30°, Line Of Sight (LOS) = 0°, Relative AZimuth Angle (RAZA) = 140°

5.2.2.1 TOA Intensity comparison

The TOA intensity comparison has been made by comparing the TOA reflectance in the atmospheric windows and in the oxygen A-band. The atmospheric windows wavelengths, select for the retrieval, are those for which the *transmittance* is greater than 0.996 and the difference between the reflectance considering and not considering the gas absorption is less than 1% i.e. the effect of the gaseous absorption is negligible (see Paragraph 2.2)). In Figure (5.7) is shown the SCIATRAN reflectance spectra without molecular absorption and the AerLIDORT reflectance for the atmospheric windows selected wavelengths. As it can be seen, the coincidence is very well; the percentage differences are always under 0.1 %.

As described in the Paragraph (5.1.1.1), the ESFT database, introduced in the forward model, give the high resolution molecular oxygen cross section

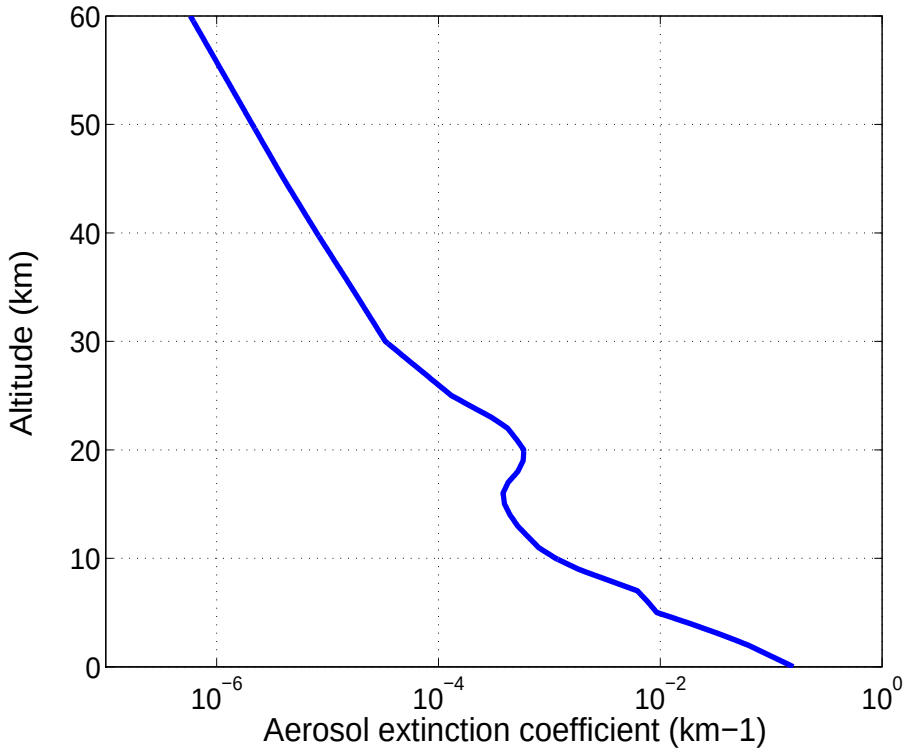

Figure 5.6: Standard MODTRAN aerosol extinction coefficient profile at 550 nm (surface visibility = 23 km, AOT = 0.3315).

every 0.05 nm from 755.025 to 775.025 nm. To obtain the SCIAMACHY simulated spectra, the high resolution spectra must be computed and the SCIAMACHY slit function applied (see Paragraph (5.1.4.1)). In Figure (5.8) and (5.9) are shown, respectively, the spectra computed before (high resolution spectra) and after (SCIAMACHY resolution) the slit function application for SCIATRAN and AerLIDORT. To give prominence the spectral difference between the simulations, the percentage difference between the spectra has been computed:

$$\Delta R = \frac{R_{sciatran} - R_{aerlidort}}{R_{sciatran}} 100 \tag{5.51}$$

where $R_{sciatran}$ and $R_{aerlidort}$ are, respectively, the TOA reflectance of SCIATRAN and AerLIDORT simulations. In Figure (5.10) are shown the percentage difference and the histograms of the differences between the high resolution spectra; as it can be seen the highest differences are relative to

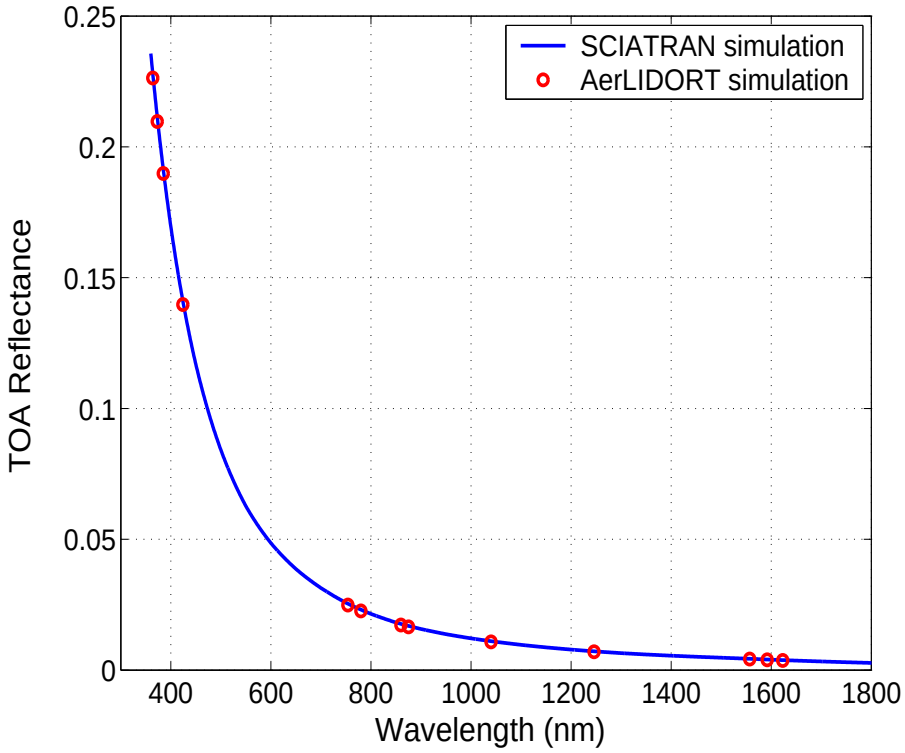

Figure 5.7: SCIATRAN TOA reflectance spectra and AerLIDORT reflectance for selected wavelengths in atmospheric windows.

low reflectance values, where the absorption coefficient is higher. In Figure and (5.11) are shown the percentage difference and the histograms of the differences, between the simulated spectra when the slit function is applied. Also in this case, as in the atmospheric window comparison, the coincidence is well, taking into account that almost the 95 % of differences ranges from $\pm 1\%$.

5.2.2.2 Weighting Functions comparison

The *weighting function* validation for a given atmospheric parameter ξ, is made by comparing the analytical *weighting function* computed by AerLIDORT and the finite-difference weighting function (K_{fd}) computation. The latter, based on the atmospheric parameter perturbation, is the most used

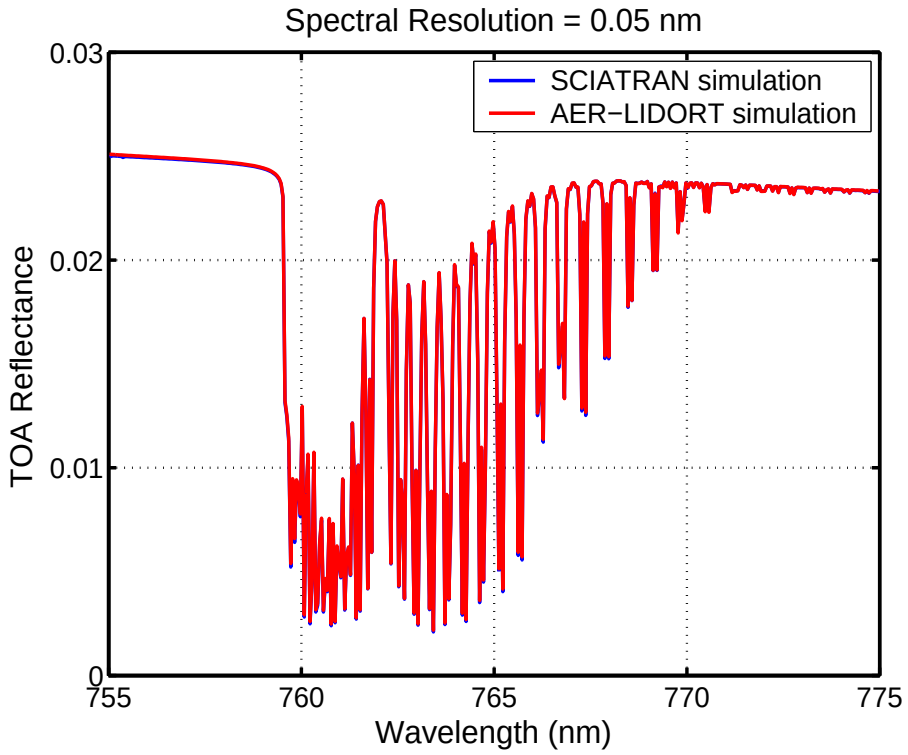

Figure 5.8: TOA Reflectance for oxygen $a-band$; spectral resolution = 0.05 nm.

method for the *weighting function* computation:

$$K_{fd} = \frac{I(\xi(1+\epsilon)) - I(\xi(1-\epsilon))}{2\epsilon} \tag{5.52}$$

where: ϵ is the relative value of the perturbation.

This requires two separate calls to the forward model, once to the atmospheric property ξ perturbed to $\xi(1+\epsilon)$ and then again with property ξ perturbed to $\xi(1-\epsilon)$. In the limit as ϵ tends to zero, the finite difference results should reproduce the analytical *weighting function*.

All the *weighting function* used in this work has been validated. In Table (5.1) and Table (5.2) are shown, respectively, the results for *aerosol extinction coefficients* (Aer_ext), *aerosol Mie phase function* (Mie_phase), *aerosol single scattering albedo* (Aer_ssalb), *oxygen absorption coefficient* (O_2_absco) and *Rayleigh scattering coefficient* (Ray_scatt) considering different levels (0.5, 5.5 and 11.5 km), for $\lambda = 550$ nm and $\lambda = 761$ nm (representatives for atmospheric window and strong absorption wavelengths). All the computa-

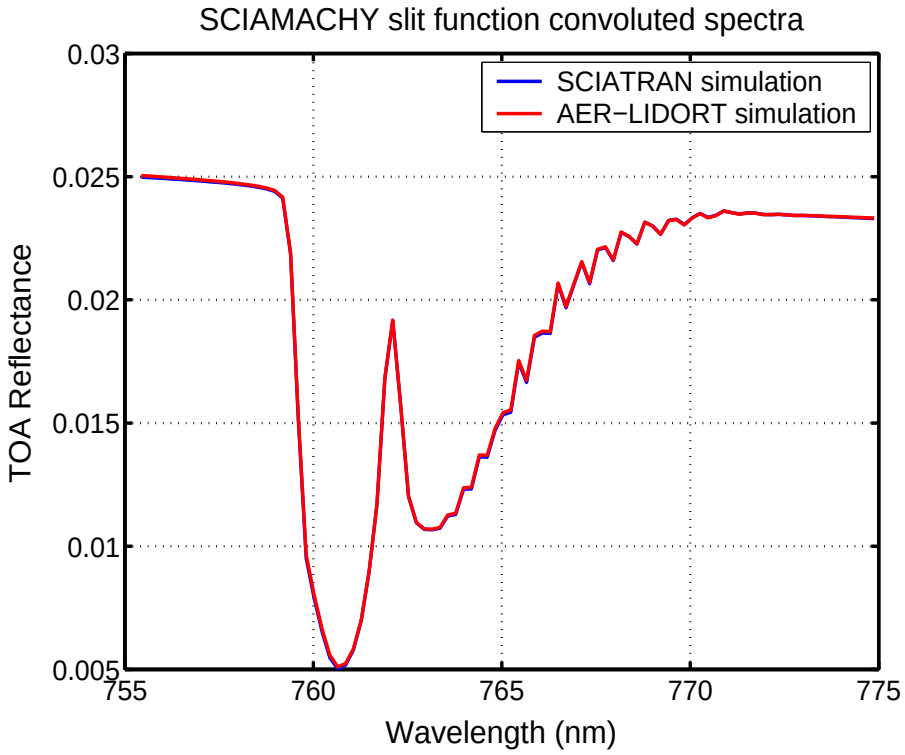

Figure 5.9: TOA Reflectance for oxygen $a-band$; convolution with SCIAMACHY slit function.

tions has been done considering a fixed 1% perturbation ($\epsilon = 0.01$).

In Figure (5.12) are shown the *weighting functions* for the atmospheric parameter described below, into the oxygen A-band.

The Tables (5.1) and (5.2) shows a very good agreement between the analytical and the finite difference weighting functions.

Note on the *weighting function* of the aerosol Mie phase function

As the Tables (5.1) and (5.2) shows, for 150 degrees scattering angle, the weighting functions of the aerosol Mie phase function are negative. Because is not intuitive understand why (differently from the other atmospheric parameters), a brief considerations will follow.

To compute an atmospheric parameter *weighting functions*, its perturbation must be done. The Mie phase function has been computed using the *Legendre moments*, so the Mie phase function perturbation regards the *Legendre*

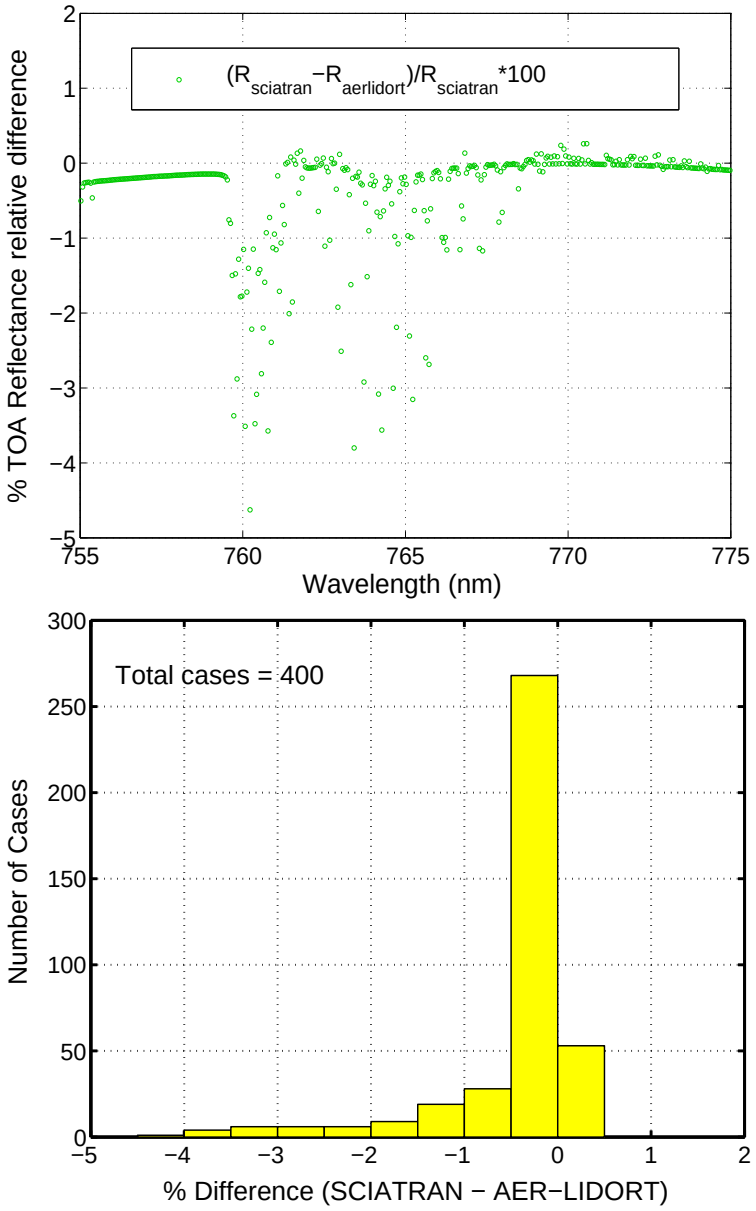

Figure 5.10: Percentage relative differences and histogram of the relative differences between SCIATRAN and AerLIDORT TOA Reflectance, considering a spectral resolution of 0.05 nm.

moments perturbation itself (see Paragraph (5.1.5)). The operation must be done carefully because the normalization property of the phase functions integral over solid angle, must be satisfied (see Paragraph (3.2)), i.e. the first *Legendre moment* must be one. Taking into account the previous considera-

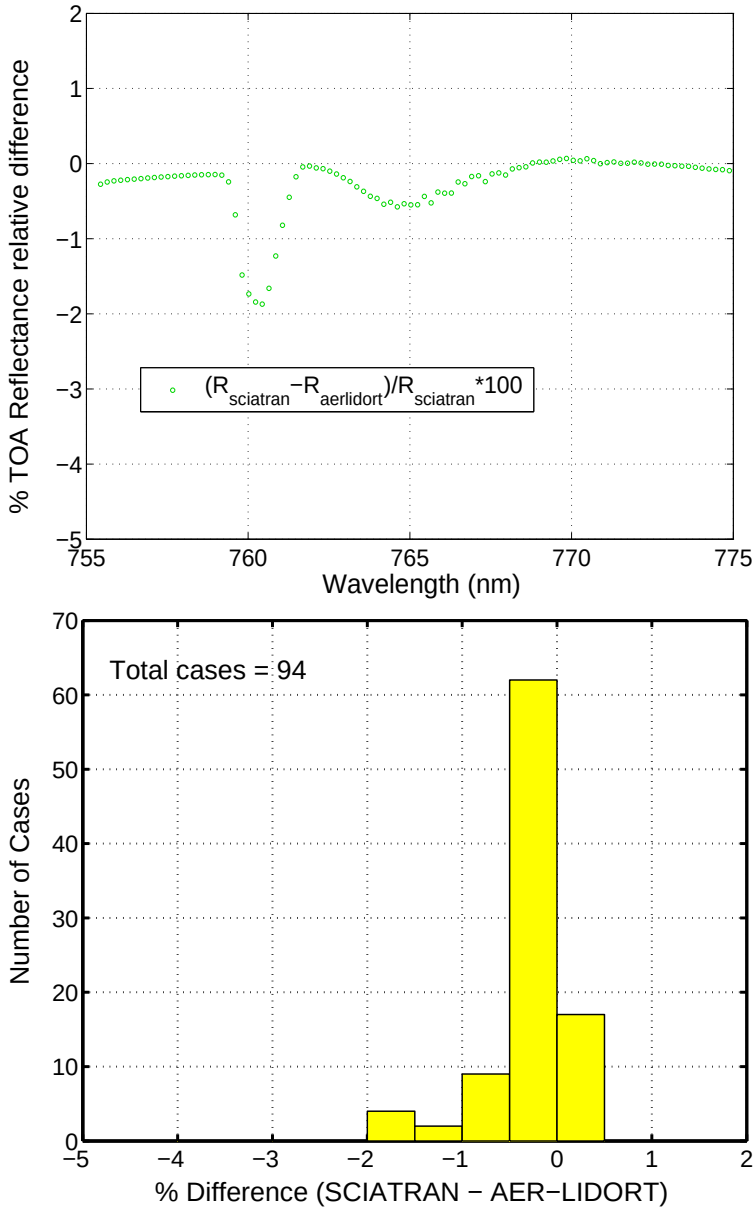

Figure 5.11: Percentage relative differences and histogram of the relative differences between SCIATRAN and AerLIDORT TOA Reflectance convoluted with SCIAMACHY slit function.

tions, the perturbed phase function becomes:

$$p_p^{'}(\mu_s) = \sum_{l=0}^{2N-1} (2l+1)\chi_{l,p}^{'} P_l(\mu_s) = \chi_{0,p} + \sum_{l=1}^{2N-1} (2l+1)\chi_{l,p}(1+\epsilon)P_l(\mu_s) \quad (5.53)$$

where:

$p_p^{'}(\mu_s)$ is the Mie phase function perturbed;

$\lambda = 550\ nm$				
parameter	*level* (km)	WF	WF_{fd}	$\%\ diff$
Aer_ext	0.5	$1.0600241 \cdot 10^{-2}$	$1.0600240 \cdot 10^{-2}$	$1.2971944 \cdot 10^{-5}$
Aer_ext	5.5	$7.1858846 \cdot 10^{-4}$	$7.1858845 \cdot 10^{-4}$	$1.0167287 \cdot 10^{-6}$
Aer_ext	11.5	$6.2497336 \cdot 10^{-5}$	$6.2497336 \cdot 10^{-5}$	$4.1840776 \cdot 10^{-8}$
Mie_phase	0.5	$-2.9935057 \cdot 10^{-2}$	$-2.9935052 \cdot 10^{-2}$	$1.5916237 \cdot 10^{-5}$
Mie_phase	5.5	$-1.8632406 \cdot 10^{-3}$	$-1.8632406 \cdot 10^{-3}$	$5.6549956 \cdot 10^{-7}$
Mie_phase	11.5	$-1.4851525 \cdot 10^{-4}$	$-1.4851525 \cdot 10^{-4}$	$2.1897358 \cdot 10^{-9}$
Aer_ssalb	0.5	$1.4806378 \cdot 10^{-2}$	$1.4806535 \cdot 10^{-2}$	$1.0554408 \cdot 10^{-3}$
Aer_ssalb	5.5	$1.7132780 \cdot 10^{-3}$	$1.7132781 \cdot 10^{-3}$	$8.4109889 \cdot 10^{-6}$
Aer_ssalb	11.5	$1.5841298 \cdot 10^{-4}$	$1.5841298 \cdot 10^{-4}$	$5.5566728 \cdot 10^{-8}$
Ray_scatt	0.5	$4.0760485 \cdot 10^{-3}$	$4.0760485 \cdot 10^{-3}$	$4.0717559 \cdot 10^{-7}$
Ray_scatt	5.5	$2.4718466 \cdot 10^{-3}$	$2.4718466 \cdot 10^{-3}$	$3.8346639 \cdot 10^{-7}$
Ray_scatt	11.5	$1.2511915 \cdot 10^{-3}$	$1.2511915 \cdot 10^{-3}$	$9.6310061 \cdot 10^{-8}$

Table 5.1: *weighting function* analytical and finite-difference comparison for different atmospheric quantity and levels, at $550nm$.

$\lambda = 761\ nm$				
parameter	*level* (km)	WF	WF_{fd}	$\%\ diff$
Aer_ext	0.5	$2.5976477 \cdot 10^{-4}$	$2.5976472 \cdot 10^{-4}$	$1.8265922 \cdot 10^{-5}$
Aer_ext	5.5	$7.5880962 \cdot 10^{-5}$	$7.5880962 \cdot 10^{-4}$	$3.1910055 \cdot 10^{-7}$
Aer_ext	11.5	$1.6313465 \cdot 10^{-5}$	$1.6313465 \cdot 10^{-5}$	$1.0846594 \cdot 10^{-9}$
Mie_phase	0.5	$-7.6383170 \cdot 10^{-4}$	$-7.6383172 \cdot 10^{-4}$	$2.2690353 \cdot 10^{-6}$
Mie_phase	5.5	$-2.3721920 \cdot 10^{-4}$	$-2.3721920 \cdot 10^{-4}$	$2.0686818 \cdot 10^{-8}$
Mie_phase	11.5	$-5.1579261 \cdot 10^{-5}$	$-5.1579261 \cdot 10^{-5}$	$1.5901720 \cdot 10^{-10}$
Aer_ssalb	0.5	$2.8609054 \cdot 10^{-4}$	$2.8609090 \cdot 10^{-4}$	$1.2616834 \cdot 10^{-4}$
Aer_ssalb	5.5	$9.1952917 \cdot 10^{-5}$	$9.1952918 \cdot 10^{-5}$	$7.7457555 \cdot 10^{-7}$
Aer_ssalb	11.5	$1.8906134 \cdot 10^{-5}$	$1.8906134 \cdot 10^{-5}$	$1.0548187 \cdot 10^{-8}$
Ray_scatt	0.5	$5.3278345 \cdot 10^{-5}$	$5.3278345 \cdot 10^{-5}$	$1.4154716 \cdot 10^{-8}$
Ray_scatt	5.5	$1.5172583 \cdot 10^{-4}$	$1.5172583 \cdot 10^{-4}$	$3.2349225 \cdot 10^{-8}$
Ray_scatt	11.5	$1.9880596 \cdot 10^{-4}$	$1.9880596 \cdot 10^{-4}$	$4.4276197 \cdot 10^{-8}$
O_2*_absco*	0.5	$-7.4405906 \cdot 10^{-5}$	$-7.4406391 \cdot 10^{-5}$	$6.5219177 \cdot 10^{-4}$
O_2*_absco*	5.5	$-3.4181367 \cdot 10^{-4}$	$-3.4181417 \cdot 10^{-4}$	$1.4781416 \cdot 10^{-4}$
O_2*_absco*	11.5	$-1.3186603 \cdot 10^{-4}$	$-1.3186606 \cdot 10^{-4}$	$2.5094795 \cdot 10^{-4}$

Table 5.2: *weighting function* analytical and finite-difference comparison for different atmospheric quantity and levels, at $761nm$.

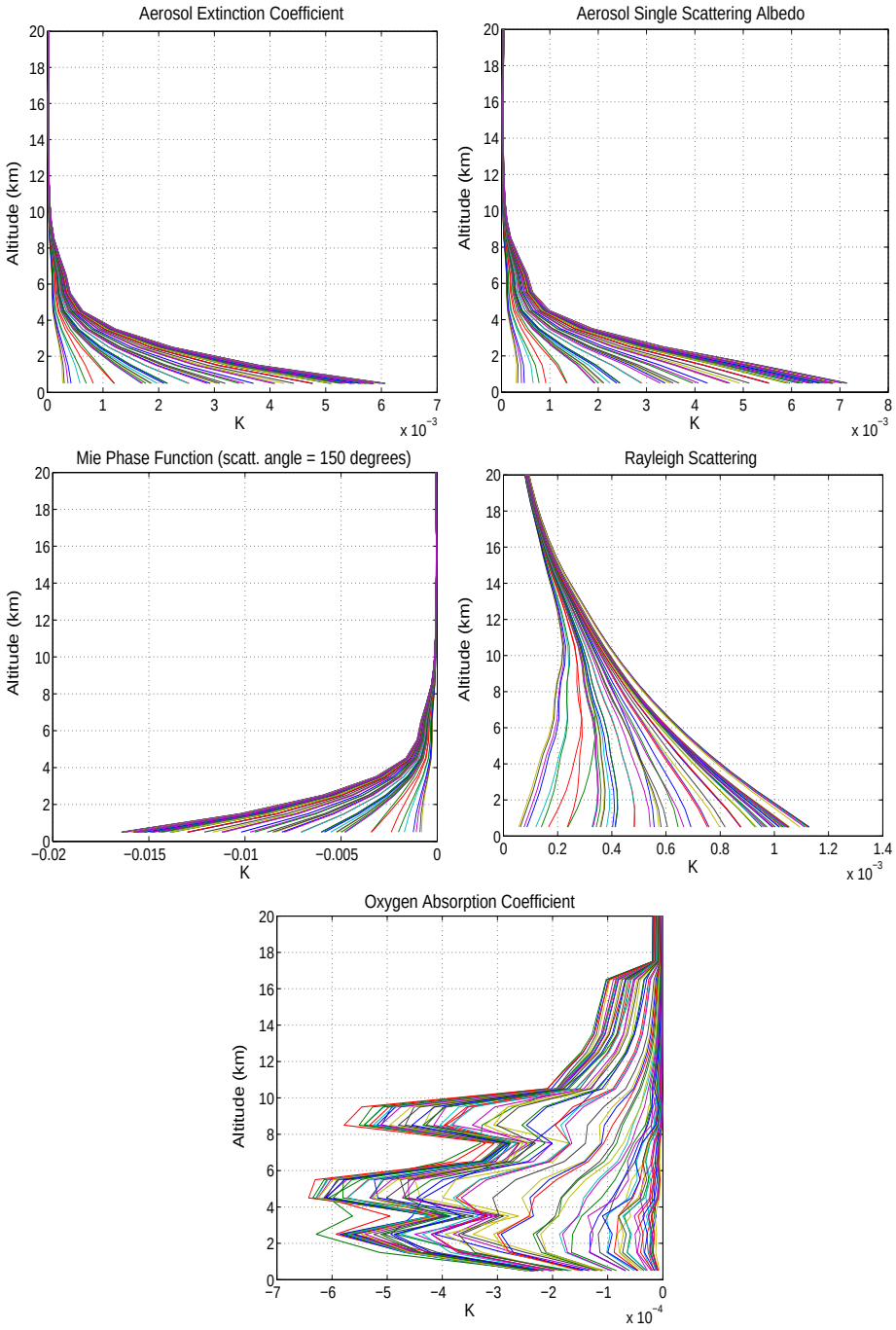

Figure 5.12: *weighting functions* computed by AerLIDORT for different atmospheric parameters.

$\chi^{'}_{l,p} = \chi_{l,p}(1+\epsilon)$ are the *Legendre moments* perturbed;

ϵ is the perturbation.

After straightforward manipulation the (5.13) becomes:

$$p_p^{'}(\mu_s) = p_p(\mu_s) + \epsilon(p_p(\mu_s) - 1) \tag{5.54}$$

The Figure (5.13) shows the phase functions original and perturbed for scattering angles between 100 and 180 degrees (scattering angle range for nadir sounding); the Figure shown, considering the scattering angle of the simulations (150 degrees), that the consequence of the *Legendre polynomials* perturbation (ϵ) is the lessening of the phase function. Considering that the TOA intensity is proportional to the phase function (in first approximation, considering the single scattering relationship ($I \propto \omega p \tau$)), if the phase function decrease, the TOA intensity also decrease. This is the reason why the weighting functions are negative.

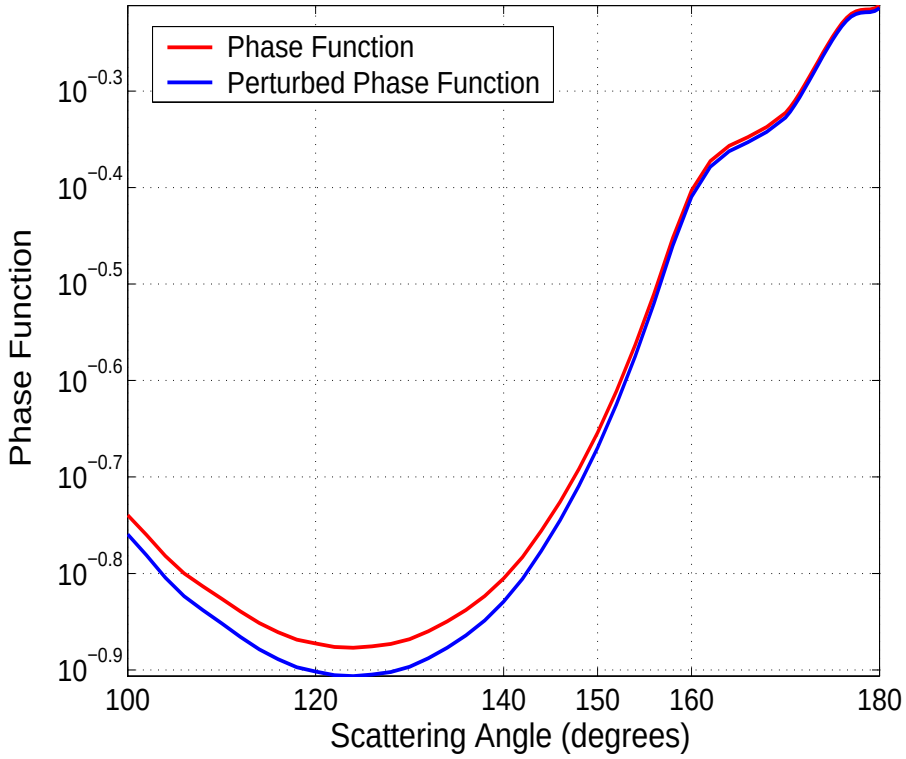

Figure 5.13: 550 nm phase function before and after the Legendre Polynomials perturbation.

5.3 Implementation of iterative inversion procedure

After the *forward model* validation, the last step for the inversion procedure development is the inversion scheme implementation (see Figure (5.14)).

As the Figure shows, at the first step ($i = 0$) the initialization profile

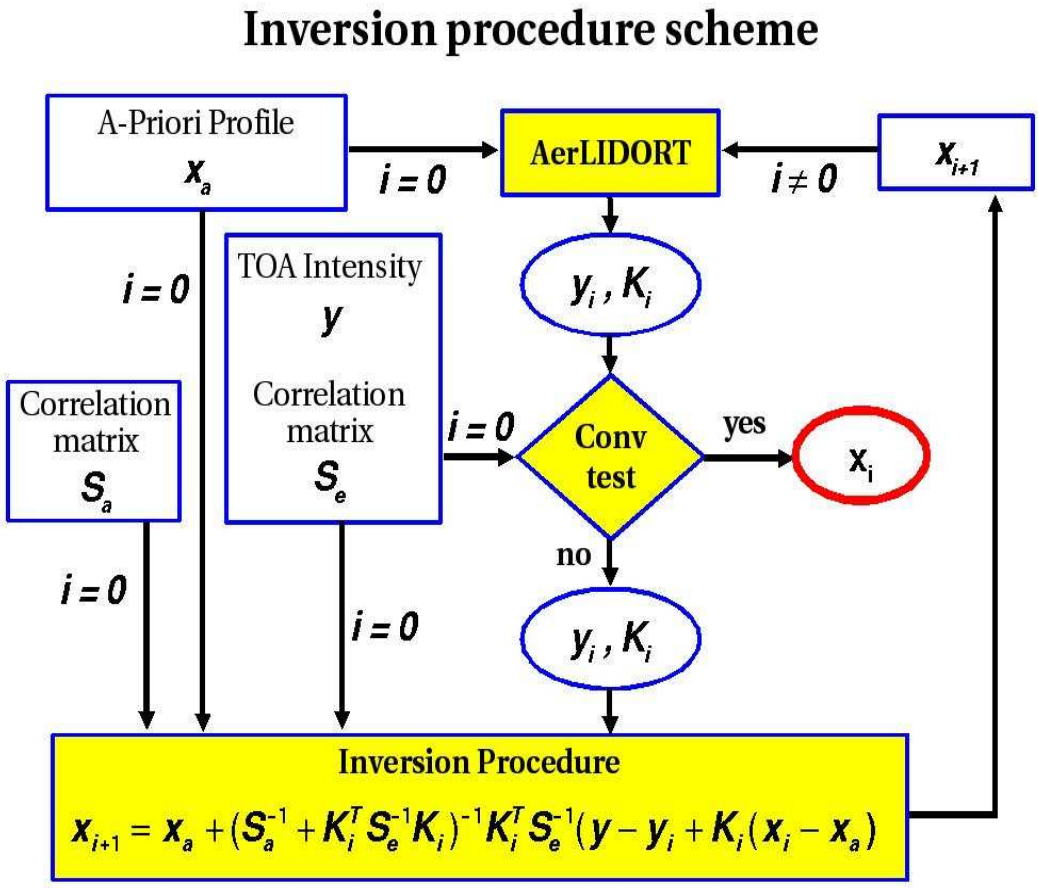

Figure 5.14: Inversion iterative procedure scheme.

(a-priori) (the *aerosol extinction coefficient* profile) is giving in input to AerLIDORT. The *forward model* gives in output the relatives TOA intensity and *weighting function*. The TOA intensity computed ($\mathbf{y_i}$) with the simulated TOA intensity ($\mathbf{y}$) and the measurement covariance matrix ($\mathbf{S}_\epsilon$) are the input for the convergence criteria subroutine. Every iterative procedure need a convergence analysis to determine the correct criterion for stopping

the iteration. The convergence criteria here considered regards the difference between the TOA reflectance computed during the iterations (relatives to the a-priori profile for the first step and to the computed profile for the following steps) ($\mathbf{y_i}$) and the simulated TOA intensity ($\mathbf{y}$) (simulated from the "true" aerosol profile taken as reference (see Chapter 6)):

$$| \mathbf{y} - \mathbf{y_i} | < (\mathbf{S}_\epsilon)^{\mathbf{1/2}} \tag{5.55}$$

When the difference between the TOA intensities is less than the measurement uncertainty, the iteration is stopped and the results is giving in output. If the convergence criteria is not satisfied, the Gauss-Newton inverse method (described in Paragraph (4.5.1)) is applied, the new iterative profile ($\mathbf{x_{i+1}}$) is computed and the iterative process restart.
For the retrievals considered in this work the iterations stopped after 3-4 iterations.

Chapter 6

Test case: SCIAMACHY nadir measurements. Setting Parameters

Since *aerosol extinction coefficient* stratospheric profiles retrieval may be obtained from SCIAMACHY limb measurements (see Chapter (2)), the possibility to retrieve the aerosol profile in troposphere from nadir measurements has been investigated. The iterative inversion procedure in multiple scattering atmosphere, developed and described in the previous Chapter, has been applied to nadir SCIAMACHY measurements to understand the effectiveness of tropospheric *aerosol extinction coefficient* profile retrieval and to carry out a complete error analysis (see Chapter (7)). In this Chapter the characteristics of the simulations and the parameters setting for the Optimal Estimation inversion technique and error analysis will be described.

6.1 Input for Optimal Estimation inversion procedure and Error Assessment

6.1.1 *State Vector* and *A-priori correlation* matrix

The aim of the work is the retrieval of the *aerosol extinction coefficient* profile at 550 nm ($\mathbf{e_{550}}$). Taking into account that e_{550} ranges over order of magnitude with height in the atmosphere (see Figure (5.6)), it is more con-

venient, from the computational point of view, to deal with the logarithm of such quantity. Therefore the *state vector* choice is the logarithm of the *aerosol extinction coefficient* profile at $550nm$:

$$\mathbf{x} = ln(\mathbf{e_{550}}) \tag{6.1}$$

Consequently the associated weighting functions are the *PNWF* (see Paragraph (3.3)).

From the *a-priori correlation* matrix definition (see Paragraph (4.2.3.2)), the diagonal elements are the square of the *state vector* standard deviation. Being the *state vector* the logarithm of the *aerosol extinction coefficient* it's trivial to demonstrate that such elements becomes the square of the ratio between the *aerosol extinction coefficient* standard deviation and the *aerosol extinction coefficient* itself:

$$\left[\sigma_{\mathbf{ln(e_{550})}}\right]^{\mathbf{2}} = \left[\frac{\sigma_{\mathbf{e_{550}}}}{\mathbf{e_{550}}}\right]^{\mathbf{2}} \tag{6.2}$$

where:

$\sigma_{\mathbf{ln(e_{550})}}$ is the standard deviation of the $ln(\mathbf{e_{550}})$;

$\sigma_{\mathbf{e_{550}}}$ is the standard deviation of $\mathbf{e_{550}}$.

For the *a-priori correlation* matrix also the interlevel correlation has been considered [*Rodgers, 1990, 2001*]:

$$\mathbf{S_{a_{i,j}}} = (\sigma_{\mathbf{a_{i,j}}})^{\mathbf{2}}\mathbf{exp}\left\{- \mid \mathbf{i} - \mathbf{j} \mid \frac{\delta \mathbf{z_{i,j}}}{\mathbf{h}}\right\}, \forall(\mathbf{i} \neq \mathbf{j}) \tag{6.3}$$

where:

$\delta z_{i,j}$ is the level distance between the i and j layers mid-altitudes;

h is the aerosol *scale height* set equal to 2 [*Smirnov et al., 2000, Gerasopoulos et al., 2003*].

Both the a-priori *aerosol extinction coefficient* profile and its standard deviation are the most critic parameters to set due to the *aerosol extinction coefficient* profile large variability over small temporal and spatial scales and the lack of the experimental source of data.

One of the few yearly records of aerosol vertical profiles available in the literature has been described by *Gobbi and Barnaba* [2003]. One year (from 15 February 2001 and 14 February 2002) of Lidar aerosol profile over Rome has been collected and analyzed. The cloudless portion of the observations, which includes planetary boundary layer aerosol, Saharan dust and cirrus cloud conditions, has been discussed. The statistical analysis of the observation has been done by both averaging over the whole dataset (yearly average) and over seasonal periods (for example June to August (JJA)). In each case, four average profiles has been provided, referring to total set of observations (TOT), observation collected in no-dust conditions (ND), observation collected in no-cirrus conditions (NC) and Saharan dust affected observations (SD). For each averaged profile also the standard deviation is given.
In this work, two tropospheric aerosol profile variation cases has been considered:
1) lower tropospheric variation considering maritime aerosol (called "*maritime test*") as representative of oceanic aerosol variation;
2) entire tropospheric variation considering desertic aerosol (called "*desertic test*") as representative of Saharan dust transport over Mediterranean. In the example selected cases the cloud effect is not considered and the retrieval and error assessment are carrying out in a midlatitude summer atmosphere, therefore the aerosol profile choice as reference are the NC and SD averaged profiles for JJA. Figure (6.1) shows the a-priori profiles considered (scaled from 532 nm (Lidar reference wavelength) to 550 nm (retrieval reference wavelength)) and the standard deviations respectively

6.1.1.1 *Aerosol extinction coefficient* profile parametrization

The *aerosol extinction coefficient* altitude parametrization considers that the region where most of the atmospheric aerosol mass is located is the planetary boundary layer (PBL), that vary, approximately, from $1-2$ to $3-4$ km respectively from winter to summer. When no tropospheric aerosol transport

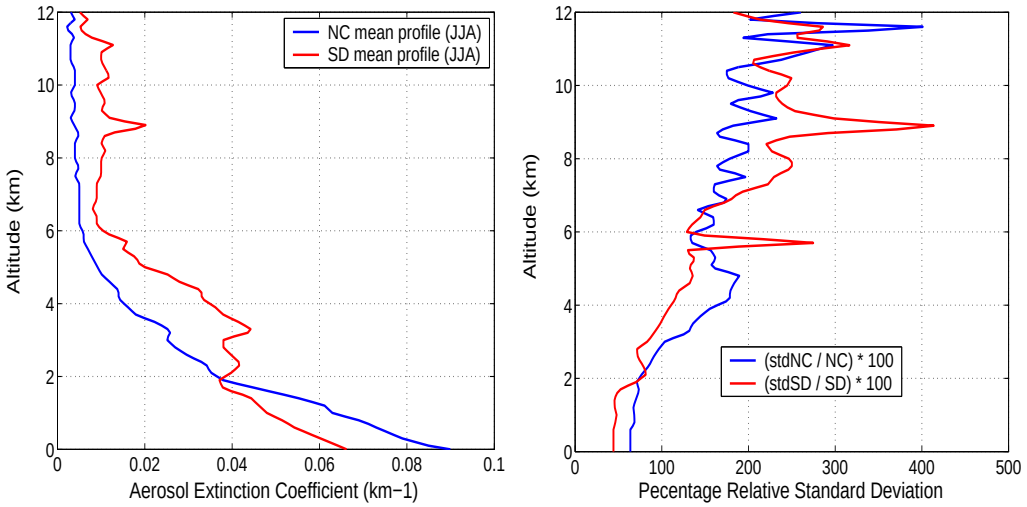

Figure 6.1: June, July and August (JJA) mean aerosol extinction coefficient profiles and percentage standard deviation for cloudless atmosphere in no-cirrus (NC) and Saharan dust (SD) conditions [*Gobbi et al., 2003*].

occurs (for example desert dust or biomass burning) the aerosol variation is limited to 3 km altitude (neglecting the stratospheric variation). Otherwise if aerosol transport occurs, as for example Saharan dust transport [*Gobbi et al., 2000,2003, Di Sarra et al., 2001*], a significative increasing of *aerosol extinction coefficient* is observed until 6 km (during dust event in the lower troposphere ($z < 6\ km$) aerosol optical thickness gets almost doubled). Thus the lower and middle troposphere have been parameterized in three layers: $0-1$, $1-3$ and $3-6$ km. The upper troposphere is composed of two layers: from $6-9$ km, to take into account very high transport phenomena and from $9-12$ km. The profile is completed adding three stratospheric layers ($12-25$, $25-40$ and $40-60$ km). The tropospheric parameterized profiles are obtained from NC and SD profile (the characteristic value for a given layer is computed as mean values of the layers computed from the original profiles) described above, while the lack of experimental profile in stratosphere (the NC and SD experimental profile is retrieved in the $0-13$ km range) is substituted by the stratospheric aerosol derived from MODTRAN standard profiles (see Figure (5.6)).

For the retrieval procedure only the first 5 layers has been considered (we are not interested in stratospheric aerosol variation). In Figures (6.2) has been shown the parametrization described for the aerosol profile. As for the a-priori profiles, the a-priori standard deviation, for the different parametrized layer, has been computed as mean from the original standard deviation profiles from $0-12$ (see Figure (6.3)). Note that the e_{550} ranges from about 0.1 to about 0.01 (see Figures (6.2)) nevertheless the state vector used is still the logarithm of e_{550} in order not to lose generality.

The "true" profiles used to simulate the SCIAMACHY TOA reflectances for

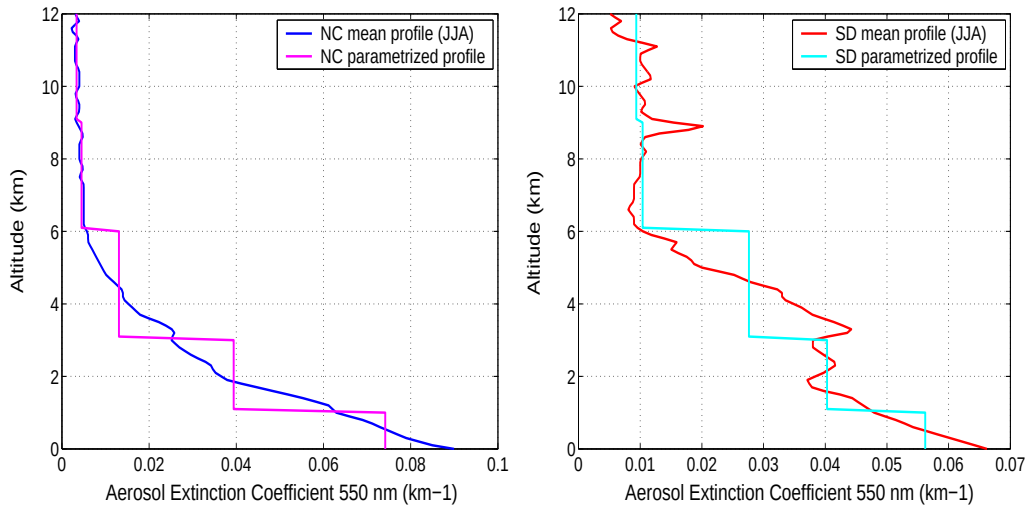

Figure 6.2: Aerosol extinction coefficient profile parametrization for *maritime case* and *desertic case*.

the two case considered, are, respectively, the MODTRAN standard profile with 23 km surface visibility and a desertic dust profile referred to a high Saharan dust event over the Mediterranean collected by Gobbi et al., [*2000*] during the spring 1999 Crete field campaign. In Figure (6.4) are shown the "true" profiles considered considering the 5 layers parametrization described.

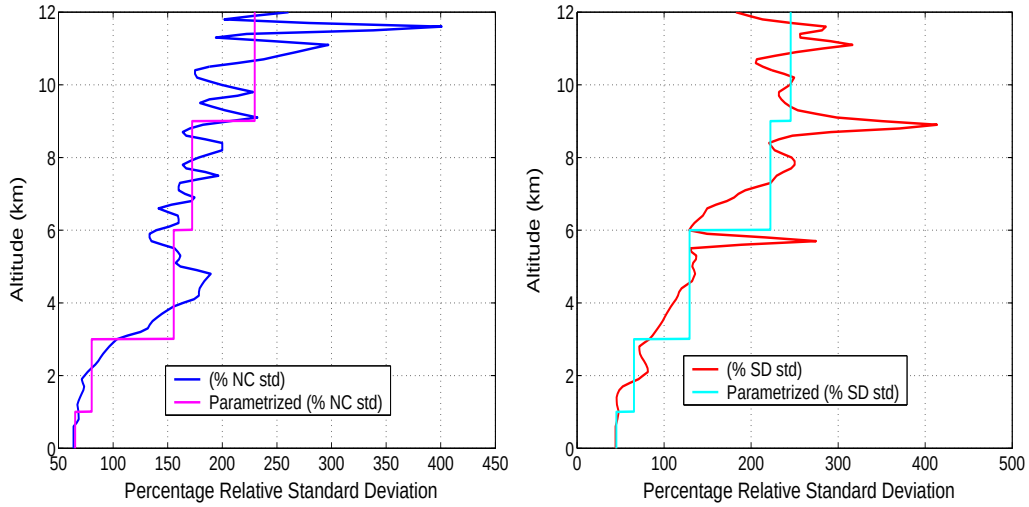

Figure 6.3: Aerosol extinction coefficient profile standard deviation parametrization for textitmaritime case and *desertic case*.

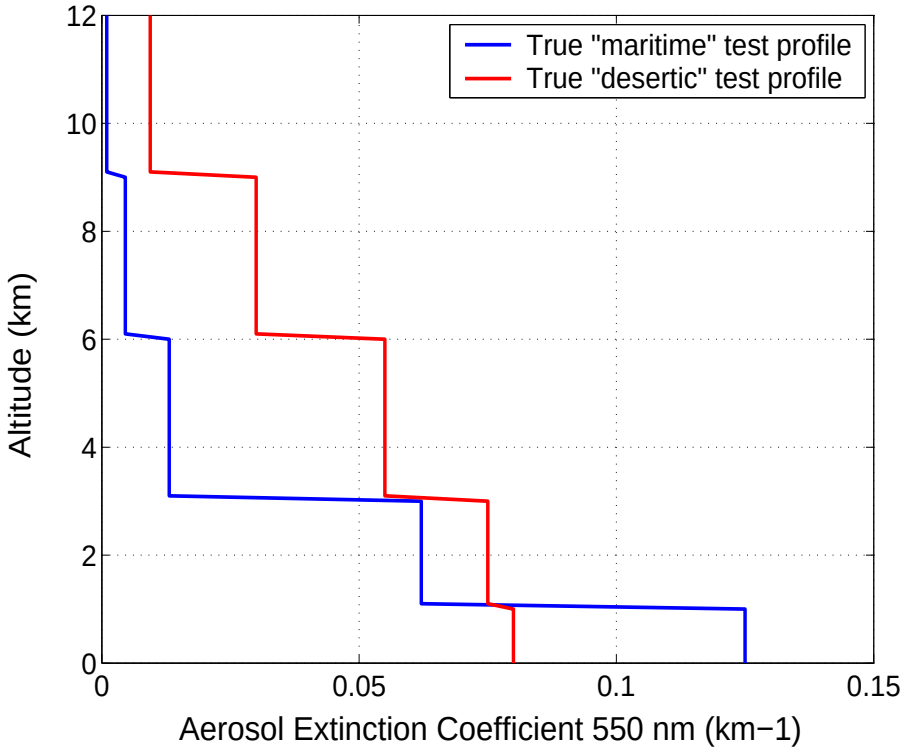

Figure 6.4: True *Aerosol extinction coefficient* profiles for *maritime* and *desert* cases.

6.1.2 *Measurement Vector* and *Measurement correlation* matrix

The *measurements vector* $\mathbf{y}$ is the SCIAMACHY simulated spectrum and the elements are the SCIAMACHY TOA simulated reflectance at different

wavelengths.

As shown in Chapter (3) the diagonal elements of the *measurement correlation* matrix are the variance of the *measurement noise*. Until now the TOA intensity uncertainty is not known because SCIAMACHY data presents calibration problem. For this reason a reasonable 1 % TOA intensity uncertainty (considered as sum among *calibration error*, *photon shot* error and *electron noise*) has been considered for every wavelength:

$$\epsilon = (\mathbf{y}\delta) \tag{6.4}$$

where: $\delta = 1\%$.

The *measurement noise correlation* matrix become:

$$\mathbf{S}_{\epsilon_{\mathbf{i,j}}} = (\mathbf{y}\delta)^{\mathbf{2}} \tag{6.5}$$

for $i = j$.

By assumption that error in each channel is uncorrelated with errors in other channels i.e. $\mathbf{S}_{\epsilon_{\mathbf{i,j}}} = \mathbf{0}$ for $i \neq j$.

6.1.3 Forward model parameters error (S_b) setting

The atmospheric parameters considered here are those quantities which influence the measurement, are known with some accuracy, but are not intended as quantity to be retrieved. The aim of the *forward model* parameters error calculation is to understand the effect of the atmospheric parameters uncertainty in the retrieval. The atmospheric parameters considered are:

1) *aerosol single scattering albedo*

2) *aerosol phase function*

3) *Rayleigh scattering coefficient*

4) *oxygen absorption coefficient*

5) *surface albedo.*

All the systematic and random errors has been computed from the equations (4.25) and (4.26) respectively. For each parameter the weighting function

has been computed (see Paragraph (5.1.5)) and the uncertainty must be set. In the following the *forward model* parameters uncertainties considered will be described.

1) 2) 5) For the *aerosol single scattering albedo*, *aerosol phase function* and *surface albedo*, has been assumed that the errors are uncorrelated and the same at all levels. If the uncertainty is Δb at all levels, then the error covariance S_b is simply $(\Delta b)^2$ times the identity matrix. 4 values for Δb has been considered:

$$\Delta b_{\omega,p,a} = 1\%, 5\%, 10\%, 30\% \tag{6.6}$$

3) As seen in Paragraph (5.1.1.2) the *Rayleigh scattering coefficient* is giving by:

$$\sigma_{p,\lambda}^{Ray} = \sigma_{\lambda}^{scatt*} \rho_p^{air} 10^5 \tag{6.7}$$

where:

σ^{scatt*} is the *Rayleigh cross section*;

$\rho^{air} = (P_p A)/(RT_p)$ is the *air density*.

From the propagation error law and considering Gaussian distribution for the different terms in equation (6.7), the $\sigma_{p,\lambda}^{Ray}$ uncertainty is giving by:

$$\left[\frac{\sigma_R}{\sigma_{p,\lambda}^{Ray}}\right]^2 = \left[\frac{1}{\sigma_{p,\lambda}^{Ray}} \frac{\partial \sigma_{p,\lambda}^{Ray}}{\partial \sigma^{scatt*}}\right]^2 \sigma_s^2 + \left[\frac{1}{\sigma_{p,\lambda}^{Ray}} \frac{\partial \sigma_{p,\lambda}^{Ray}}{\partial P}\right]^2 \sigma_P^2 + \left[\frac{1}{\sigma_{p,\lambda}^{Ray}} \frac{\partial \sigma_{p,\lambda}^{Ray}}{\partial T}\right]^2 \sigma_T^2 \tag{6.8}$$

where:

σ_R is the *Rayleigh scattering* standard deviation;

σ_s is the *Rayleigh cross section* standard deviation;

σ_P is the *pressure* standard deviation;

σ_T is the *temperature* standard deviation.

Substituting the equation (6.7) in (6.8):

$$\left[\frac{\sigma_R}{\sigma_{p,\lambda}^{Ray}}\right]^2 = \left[\frac{\sigma_s}{\sigma^{scatt*}}\right]^2 + \left[\frac{\sigma_p}{P}\right]^2 + \left[\frac{\sigma_t}{T}\right]^2 \tag{6.9}$$

Considering negligible the *Rayleigh cross section* uncertainty the (6.9) becomes:

$$\Delta b_R = \left[\frac{\sigma_R}{\sigma_{p,\lambda}^{Ray}}\right]^2 \simeq \left[\frac{\sigma_p}{P}\right]^2 + \left[\frac{\sigma_t}{T}\right]^2 \tag{6.10}$$

The pressure and temperature standard deviation has been taken from a statistical study made from Pugnaghi and Gangale of the University of Modena and Reggio Emilia (private communication), that elaborates 14 years (from 1989 to 2003) of daily radio-sounding of Trapani (north-west of Sicily (Italy)). The standard deviations considered are the mean values from June, July and August of the cited data and are shown in Figure (6.5).

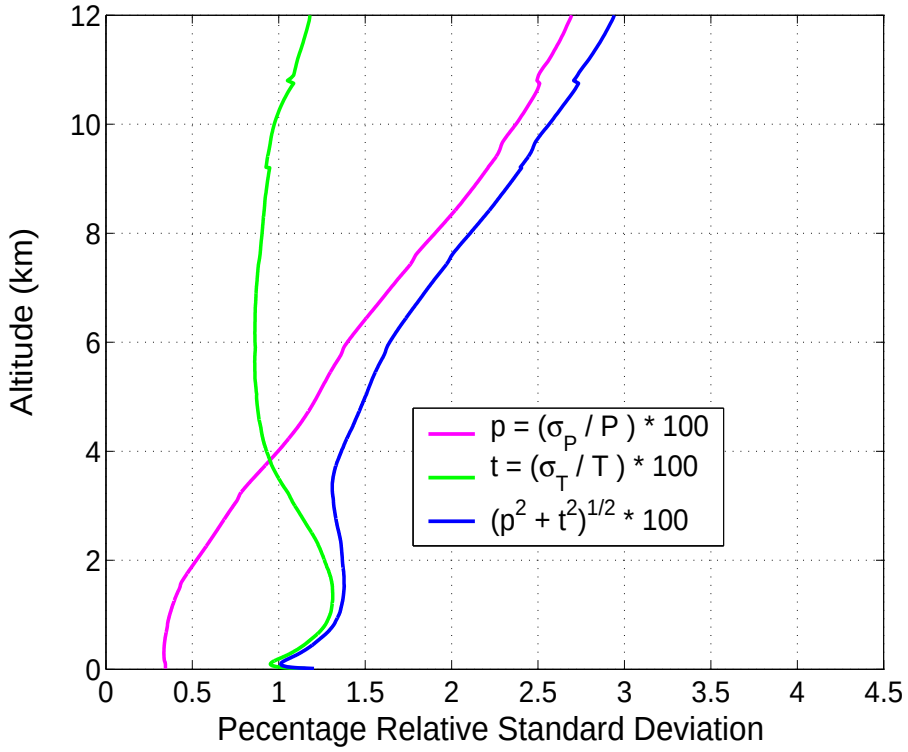

Figure 6.5: Percentage relative standard deviation for P, T and Rayleigh scattering.

4) As seen in Paragraph (5.1.1.1) the oxygen absorption coefficient ($\alpha_{p,\lambda}$

is giving by:

$$\alpha_{p,\lambda} = \alpha_{p,\lambda}^{abs} \rho_p \tag{6.11}$$

where:

$\alpha_{p,\lambda}^{abs}$ is the *specific absorption cross sections*;

$\rho_p = 0.1[(ppm_p P_p A)/(RT_p)]$ is the oxygen molecular density and ppm_p the oxygen part per million (see equation (5.7)).

Considering negligible the *specific absorption cross sections* uncertainty, the oxygen absorption coefficient uncertainty becomes:

$$\Delta b_\alpha = \left[\frac{\sigma_\alpha}{\alpha_{p,\lambda}^{abs}}\right]^2 \simeq \left[\frac{\sigma_p}{P}\right]^2 + \left[\frac{\sigma_t}{T}\right]^2 \tag{6.12}$$

as in the case of the *Rayleigh scattering coefficient*.

6.1.4 Forward model error setting

An additional source of error arises from approximations made in the *forward model* due to the use of a low number of streams in the discrete ordinate radiative transfer model. For the reference atmosphere the *forward model* is running with 20 streams to get an accurate simulation of the radiance; the computation is repeated with 4, 6, 8 and 12 streams. The *forward model* errors are then $\Delta F_4 = R_{20} - R_4$, $\Delta F_6 = R_{20} - R_6$, $\Delta F_8 = R_{20} - R_8$ and $\Delta F_{12} = R_{20} - R_{12}$ where R_N are the radiance for the N-stream approximation. This error source will be treated as systematic because its effect will be manifest as an offset on the retrieved state. This error assessment is very important for the time computation resource, because the higher number of stream is the best simulation results, but with computation time higher cost.

6.2 Sensitivity Study

The sensitivity study has been performed by varying the Solar Zenith Angle and the surface albedo. For the SZA sensitivity a range from 15 to 75 degrees (step 15 degrees) has been considered. Two different surfaces has been

considered: Sea surface (as example of low albedo) and Vegetation surface (as example of high albedo).

6.3 Characteristics of simulations

All the simulations made for the *aerosol extinction coefficient* profile retrieval and error assessment has been done considering fixed geometry (LOS = 0° and SZA = 60°) and Sea surface. The "true" profiles TOA reflectance simulations has been made considering the maximum number of streams selectable. The inversion processing has been done considering 8 streams to reduce the processing times; in Paragraph (7.3.2) will be shown the error due to the using of a low number of streams.

The pressure and temperature considered are referred to midlatitude summer standard atmosphere.

The retrieval and error assessment has been analyzed using both the atmospheric windows and the oxygen A-band wavelengths. The atmospheric windows wavelengths selected (13 wavelengths) are those for which the molecular absorption is negligible (see Chapter 2); the oxygen A-band wavelengths considered (68 wavelengths) are included between 758 and 772 nm, step 0.2 nm.

For the error assessment and sensitivity issues addressed in this study, we carry out a single inversion step by linearizing the forward model by the a-priori reference state vector.

Chapter 7

Test case: SCIAMACHY nadir measurements. *Aerosol extinction coefficient* profile retrieval Atmospheric windows wavelengths and Oxygen A-band comparison

A complete a-priori analysis has been execute for the *aerosol extinction coefficient* profile retrieval and error assessment for SCIAMACHY nadir configuration, considering atmospheric windows (hereinafter *AtmWin* test) and oxygen A-band wavelengths (hereinafter *Oxygen* test). For each test, the two aerosol profile configuration ("*maritime case*" and "*desert case*), described in Chapter 5, has been considered.

7.1 A-priori analysis

7.1.1 *Maritime* test

From equations (4.31) and (4.34) the *Degrees of Freedom for Signal* (DFS) and the *entropy variation* (H) has been computed; results are respectively 1.21 and 7.04 for *AtmWin* retrieval and 3.18 and 14.9 for the *Oxygen* retrieval.

In Figure (7.1) are shown, for both cases, the a-priori profile *weighting functions*, the *averaging kernel* matrix and the *retrieval errors components* when the *forward model* and *forward model parameter* error are neglected (see Paragraph (4.3)). The *averaging kernel* matrix (A) has been computed multiplying the *gain matrix* (G) for the *aerosol extinction coefficient weighting function* (K), (see Paragraph (4.3.2)), and its rows has been plotted. *Measurement errors*, *smoothing errors* and *total errors* are plotted as the square root of the covariance matrix diagonal elements computed using, respectively, equations (4.21), (4.23) and (4.24).

For the different scenario the information content changes meaningfully. Differently from the *AtmWin*, in the *Oxygen* more information comes from the measurements than from the a-priori. Increase in measurements information is manifested as increased precision in profile elements. This consideration can be proved looking at the *averaging kernel* plotted in Figure (7.1). Considering the atmospheric windows wavelengths (middle left plate), the *averaging kernels* presents a poorly defined peak and it is impossible assign any Full Width Half Maximum (FWHM) values to get an idea of the retrieval vertical resolution. *Averaging kernel* is more sharply defined for the *Oxygen* case (middle right plate) in the three bottom layers, where it is possible assign a rough FWHM of 1, 2 and 3 *km* (see the curves labeled with 0.5, 2 and 4.5). The same considerations can be extended looking at the altitude peak of the averaging kernels labeled. As the middle plates shows, the peaks of the averaging kernels are more distributed in altitude and located at the right level for the first three layers and for the fifth layer only for the *Oxygen* case.

Looking at the error components of the same Figure (bottom plates), it can be noted that the bigger error component in both cases is due to the *smoothing error*, i.e. the error due to the system capability to resolve the altitude profile resolution is always bigger than the retrieval error induced by the measurements errors. But, if for the *AtmWin* the total error is close

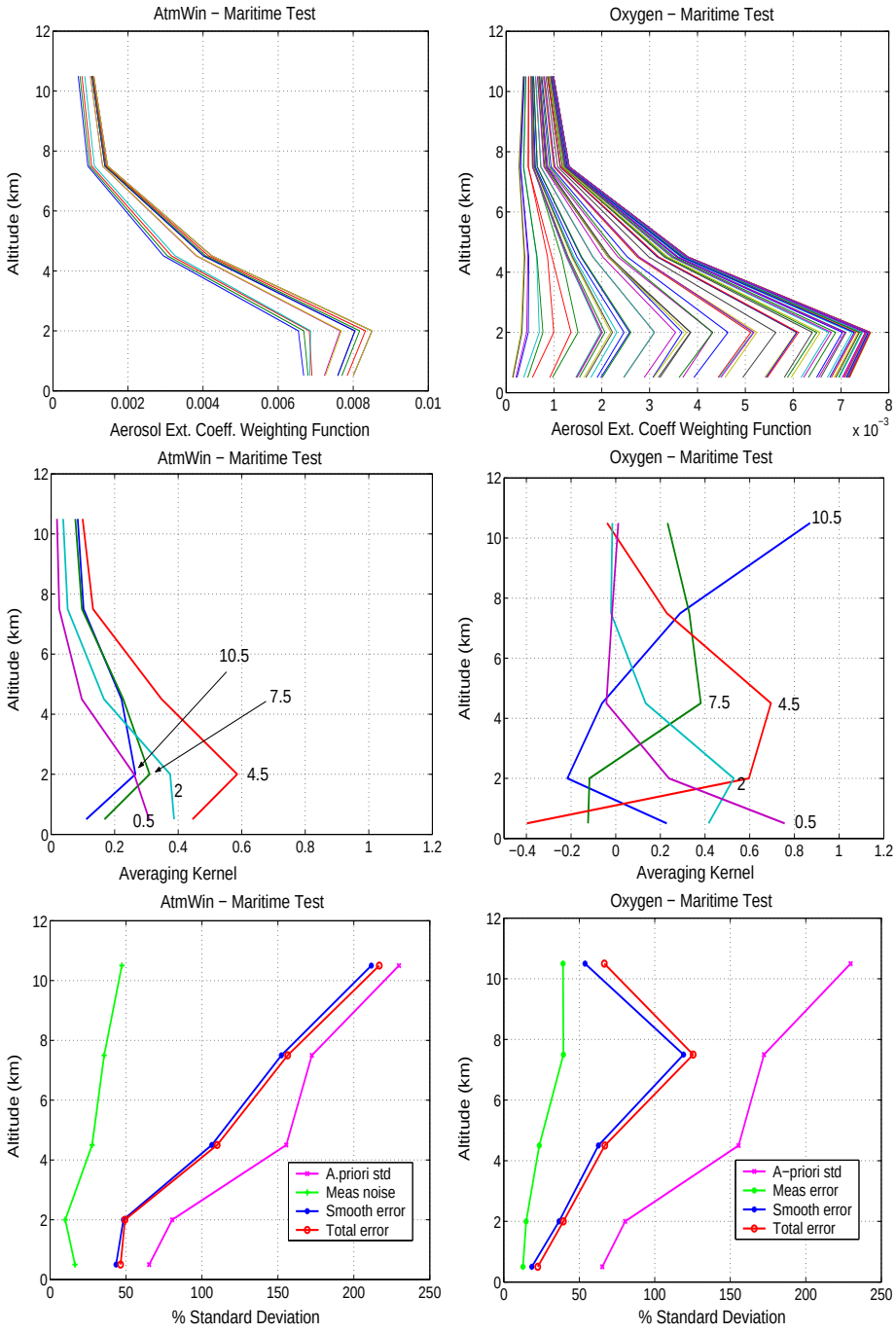

Figure 7.1: *Weighting functions*, *averaging kernels* and *retrieval error* for atmospheric windows and oxygen A-band *maritime* case retrieval. The averaging kernel curves are labeled with the middle layers altitude in kilometers.

to the a-priori error, so the greater part of the information about the retrieved profile coming from the a-priori instead of the measurements, for the

Oxygen the total retrieval standard deviation is significantly lesser than the a-priori standard deviation; this means that there is an important quantity of information coming from the measurements.

7.1.2 *Desertic* test

DFS and H are respectively 1.95 and 8.67 for *AtmWin* retrieval and 3.20 and 15.4 for the *Oxygen* retrieval. As in the previous case, in Figure (7.2) has been shows the *weighting functions*, the *averaging kernels* and the *measurements*, *smoothing* and *total* errors components for the *desertic* test.
Comparing the information content values with *maritime* test, can be seen that there is a meaningful increasing of information for *AtmWin* while the information content for *Oxygen* remain almost constant. The expected improvement of information content for *desertic* test respect to the *maritime* test in *AtmWin* is due to a more different aerosol optical properties between UV and NIR wavelengths for the desertic aerosol class respect to the maritime class.

The Figure (7.3) shows the single scattering albedo for *maritime* and *desertic* aerosols all over the spectrum range from UV to NIR and focused in the oxygen A-band spectral range. Looking to the left picture of Figure (7.3) it can be noted that if *maritime* aerosol presents, approximately, the same behavior over all spectral range, the *desertic* aerosols is more absorbing in the range $300 - 500$ nm than elsewhere. It is just this peculiar physical characteristic of the *desertic* aerosol class that produce the improving of the information content found. Looking at the right picture of the same Figure it can be understood why the information content of the oxygen doesn't change in a significant way.
This behavior can be noted also looking at the top left picture of Figure (7.2), where the *AtmWin weighting functions* has been plotted. The curves relatives to the first four wavelengths (364, 373, 385 and 414 nm) are very different from the others, and in particular presents negative values up to

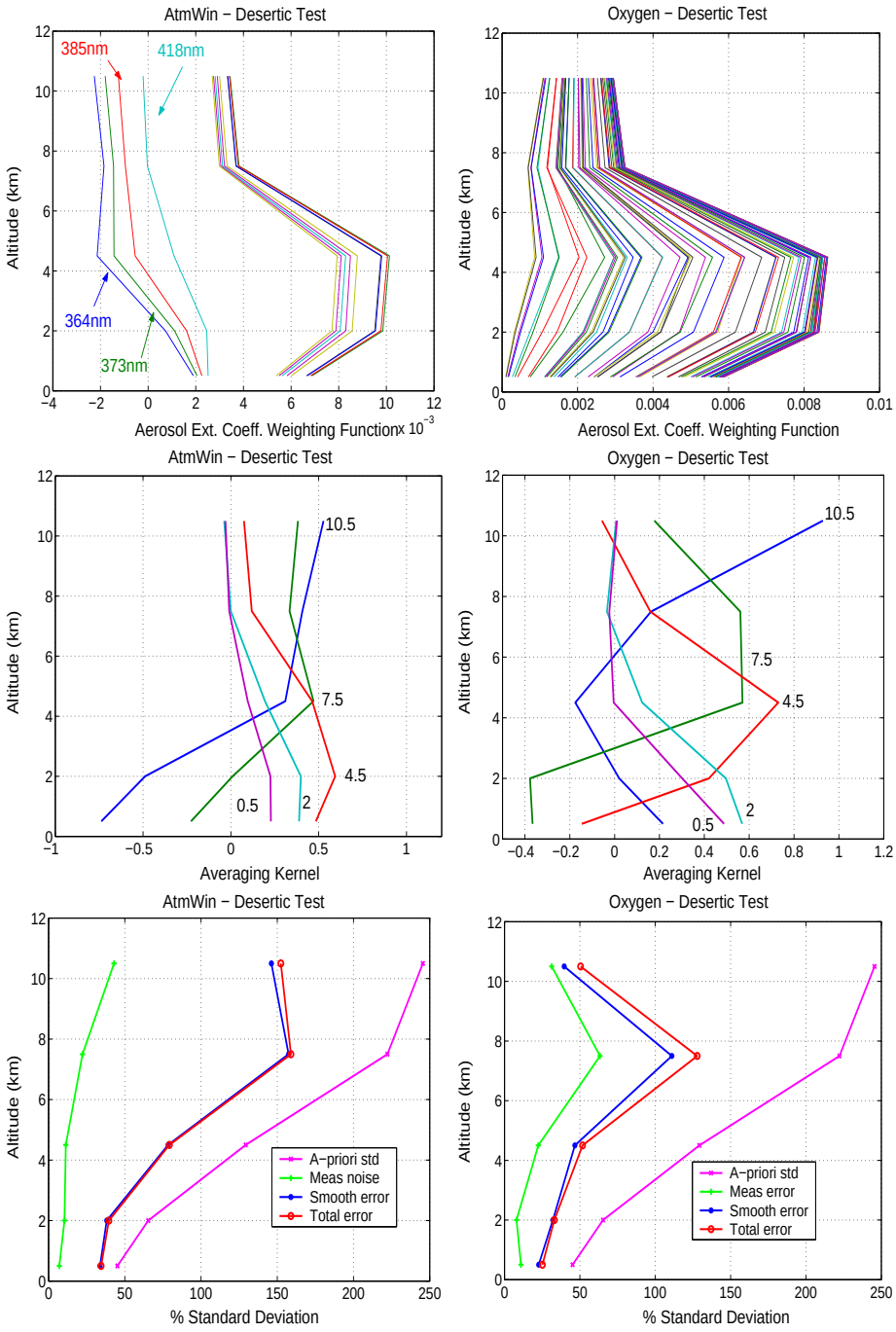

Figure 7.2: A-priori profile weighting function and averaging kernel for *desertic* test retrieval, using atmospheric windows and oxygen wavelengths. The averaging kernel curves are labeled with the middle layers altitude in kilometers.

the first layer. This behavior is very interesting from the "radiative effects" point of view, because shows that, in the UV spectral range, an absorbing

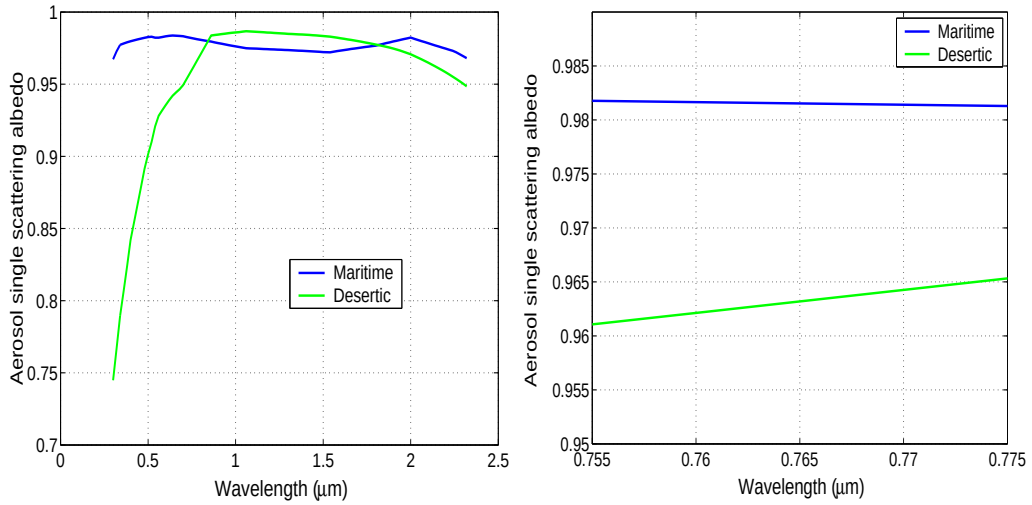

Figure 7.3: Aerosol single scattering albedo for the *maritime* and *desertic* classes in UV-VIS-NIR spectral range and focused into oxygen A-band.

aerosol presents opposite radiative effects, at top of the atmosphere, when an aerosol variation occurs at different altitude. In particular an absorbing aerosol increase at the bottom of the atmosphere increases TOA reflectance, while an aerosol increase at the upper tropospheric layers decreases TOA reflectance.

Even if the absorbing aerosol class improve the information content of the problem, looking at *AtmWin averaging kernel* and *retrieval errors* (see middle and bottom left picture of Figure (7.2)) this behavior isn't sufficient to resolve the altitude uncertainty. Also in this case the use of the oxygen A-band spectral wavelengths gives the best results, the *averaging kernel* is better characterized and the errors are lower.

7.1.3 Information content of higher spectral resolution in the Oxygen A-band

As shortly described in Chapter (1) the rationale of retrieving vertical aerosol profile by using measurements at oxygen absorption wavelengths, is to exploit the different penetration depth of solar incoming radiation into the atmosphere, observed by the uniformly mixed gas [*O'Brien, 1997; Heidinger*

et al., 1999]. This physical phenomenon is the main drive of the oxygen transmittivity averaging kernel vertical shape relationship that permits the vertical profile retrieval. In the following will be show that the higher the spectral resolution of measurements is considered (i.e. greater the oxygen absorption coefficient is) the better the vertical resolution accuracy becomes. In Figure (7.4) has been plotted the a-priori profile *weighting functions*, the *averaging kernel* matrix and the *retrieval errors components* (as in the cases considered before) for the *maritime* and *desertic* tests, considering the maximum spectral resolution introduced in the *forward model* (0.05 nm). Comparing the averaging kernels shape of Figures (7.1) and (7.2) with averaging kernels of Figure (7.4) an improved characterization arises. Each averaging kernel curve peak is located at right retrieval level and the FWHM make the retrieval suitable. Similar consideration can be done looking at bottom plates of Figure (7.4); the lower impact (compared with *AtmWin* and *Oxygen* cases) of the smoothing error shows the system ability to reach the altitude profile resolution request. Since the same Figure shows the smoothing error and the measurements errors have the same order of magnitude, the retrieval accuracy become strongly dependent on measurements errors. The difference between the a-priori and *total error* shows that the measurements are able to improve meaningfully the knowledge of the system.

7.1.4 A-priori analysis using both atmospheric windows and Oxygen A-band wavelengths

An information content study is also been done considering together the atmospheric windows and oxygen A-band wavelengths, trying to mix the information due to the absorbing characteristics of oxygen a-band and the previous described spectral characteristics of aerosol in a wide UV-VIS-NIR spectral range. DFS and H results respectively 3.20 and 15.2 for *maritime* test and 3.22 and 15.8 for *desertic* test. There isn't a significant increase in accuracy for the aerosol tropospheric variation using both atmospheric

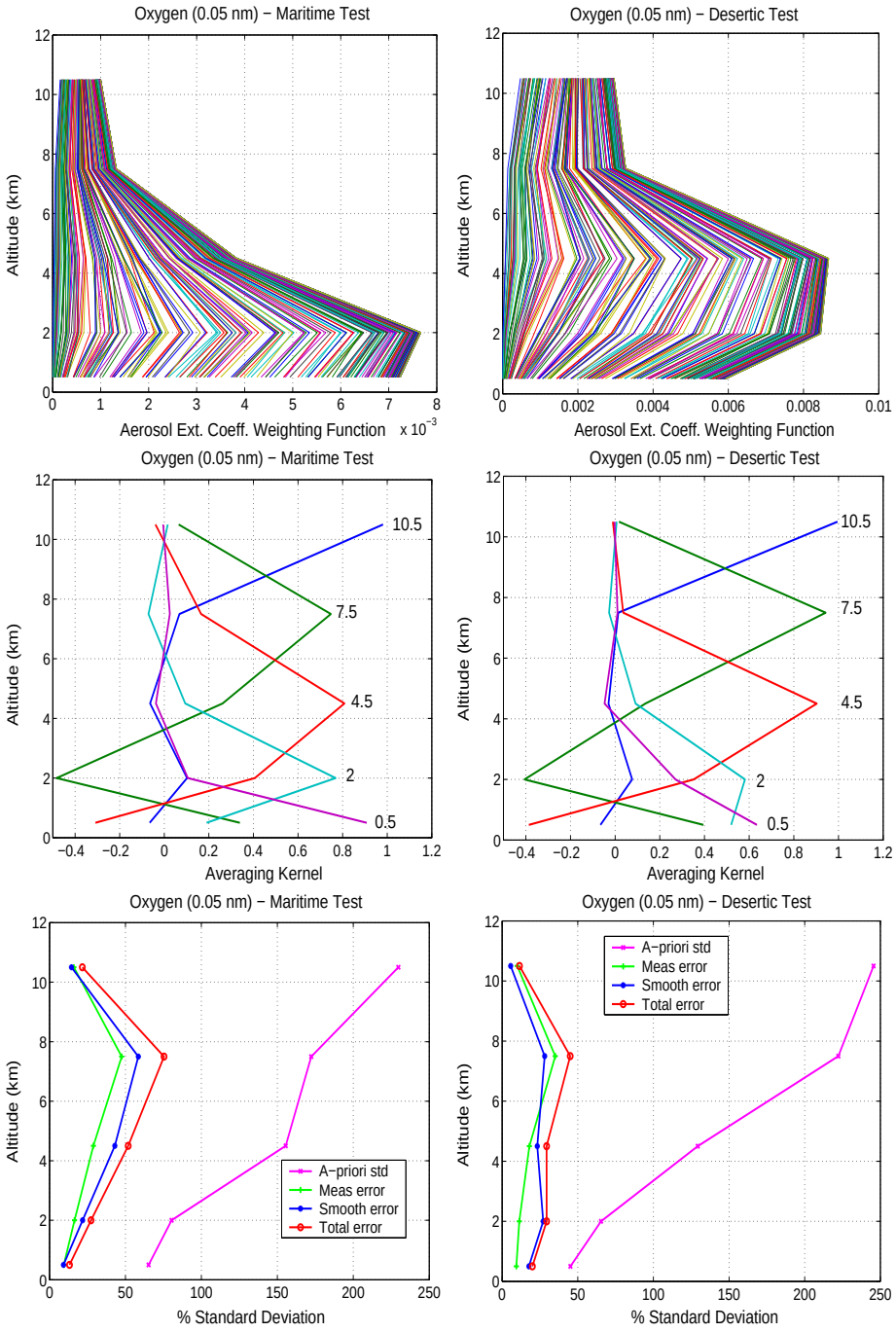

Figure 7.4: Weighting functions, averaging kernels and retrieval error for 0.05nm spectral resolution in oxygen A-band for *maritime* and *desertic* tests. The averaging kernel curves are labeled with the middle layers altitude in kilometers.

windows and oxygen A-band wavelengths.

7.2 *Maritime* and *Desertic* test retrieval for Oxygen A-band

The previous analysis shows that the best results occurs when the oxygen A-band spectral range is considered. The retrieval test has been therefore execute considering the oxygen A-band wavelengths for both *maritime* and *desertic* tests.

The inversion procedure converge rapidly after $3-4$ iterations. The Figure (7.5) shows the a-priori, true, retrieved aerosol profile for the two cases considered and the error bars relatives to the *total errors* plotted in Figures (7.1) and (7.2), not considering the *forward model* and *forward model parameter* errors. In Table (7.1) are shown the total AOT retrieved. Analyzing the

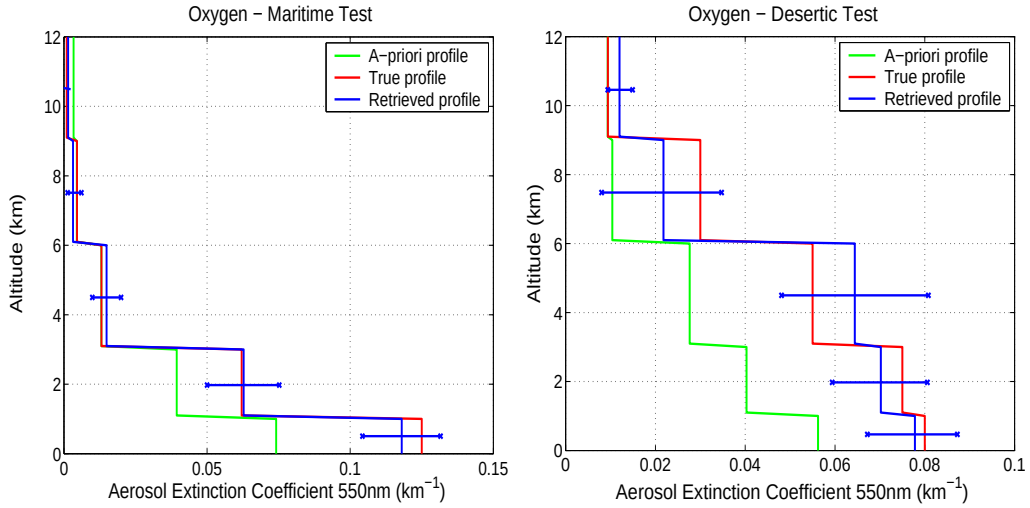

Figure 7.5: Aerosol extinction coefficient profile retrieval for *maritime* and *desertic* tests in oxygen A-band.

Test	$A-priori\ AOT$	*True AOT*	*Retrieved AOT*
Maritime	0.26	0.32	0.31
Desertic	0.21	0.49	0.52

Table 7.1: Aerosol Optical Thickness at 550nm a-priori, true and retrieved for *maritime* and *desertic* tests.

Figure (7.5) it can be seen that the retrieval shows a good agreement with

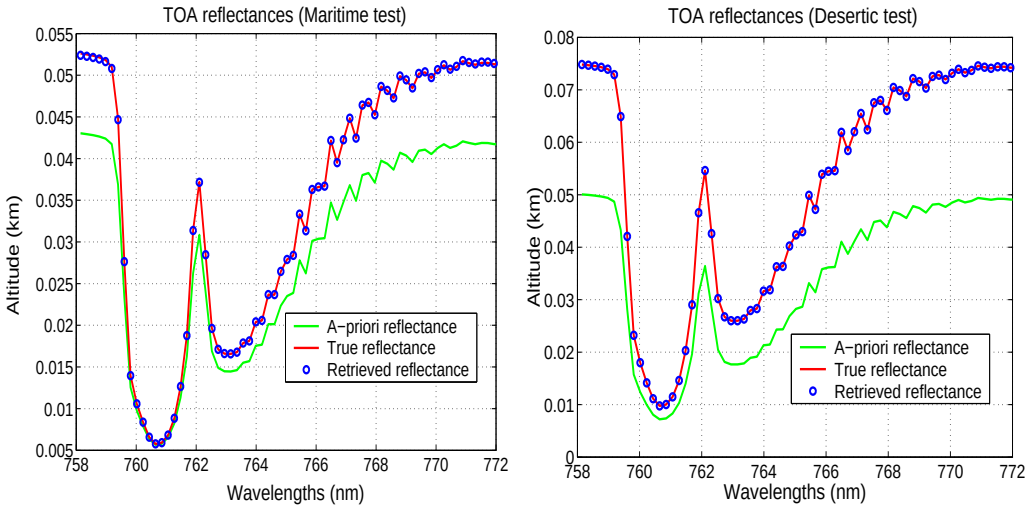

Figure 7.6: TOA reflectance retrieved for *maritime* and *desertic* test in oxygen A-band.

the true profile that is comprised into the error bars range. Also the retrieved and true total AOT shows good agreement.

In Figure (7.6) has been show the TOA reflectance intensity referred to the a-priori, true and retrieved profile, for the two cases considered. The very close match between true and retrieved spectrum shows the goodness of the inversion procedure.

7.3 Sensitivity and error assessment in Oxygen A-band for *maritime* test

As shows in the last Paragraphs the use of the measurements in the oxygen A-band gives the best results regard the possibility to retrieve the tropospheric *aerosol extinction coefficient* profile. The previous a-priori analysis also shows that the differences between the cases considered (*maritime* and *desertic*) are not meaningful. For these reasons the sensitivity study and the complete error assessment has be done considering the oxygen A-band and the *maritime* test case.

Even if the large fraction of the naturally occurring tropospheric aerosol are represented by *maritime* and *desertic* particles [*Charlson and Heintzenberg,*

1995], the results obtained are relative to the cases considered. To extrapolate general considerations about the aerosol extinction coefficient profile retrieval errors using SCIAMACHY nadir measurements in the oxygen A-band, more test should be done, for different aerosol class, optical thickness and stratification.

7.3.1 Solar Zenith Angle and Surface albedo sensitivity

The retrieval sensitivity has been computed by varying the Solar Zenith Angle and the surface albedo. In Figure (7.7) has been shown the degrees of freedom and the entropy variation by varying SZA. It can be seen that the information content increase when the SZA increase (then when the scattering angle decrease), i.e. when the solar zenith angle increase also the the measurements contribution to the profile accuracy is improved.

The albedo sensitivity has been analyzed comparing the information con-

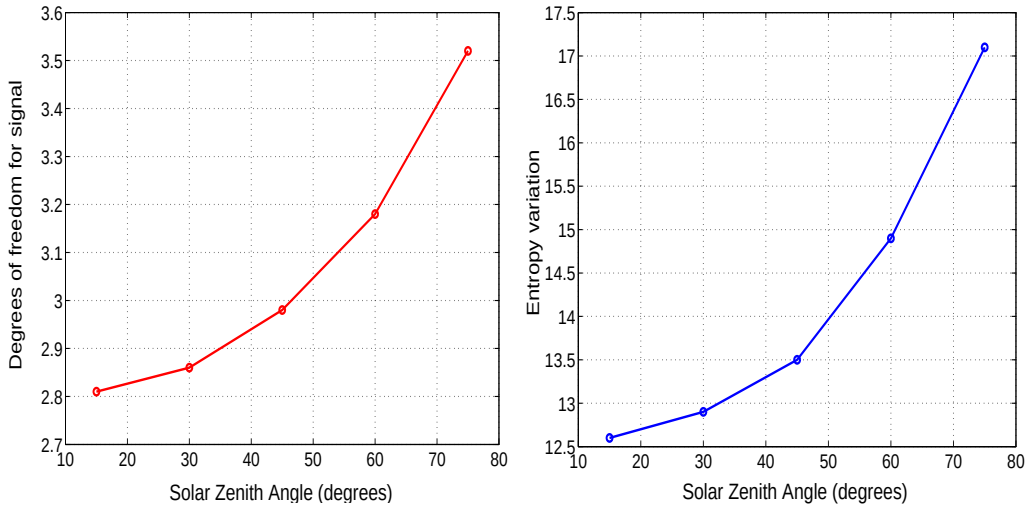

Figure 7.7: Degrees of freedom and Entropy variation varying the solar zenith angle, for *maritime* test in oxygen A-band. The averaging kernel curves are labeled with the middle layers altitude in kilometers.

tent and averaging kernel considering Sea surface (i.e. considering a quasi-black surface) and Vegetation surface (i.e. considering a relative high surface

albedo). In Table (7.2) are summarize the DFS and H resulting by the simulations, while in Figure (7.8) has been plotted the averaging kernels. As Table (7.2) shows, the information content decrease meaningfully when the albedo surface increases and (Figure (7.8)), the averaging kernel results worse characterized for relative high surface albedo. The reason is that when the surface reflection is significative, the system is not able to distinguish the information comes from the ground from which coming from the aerosol in the lower atmospheric layers.

$Surface$	DFS	H
Sea	3.18	14.9
$Vegetation$	2.24	7.61

Table 7.2: Information content considering Sea and Vegetation surface.

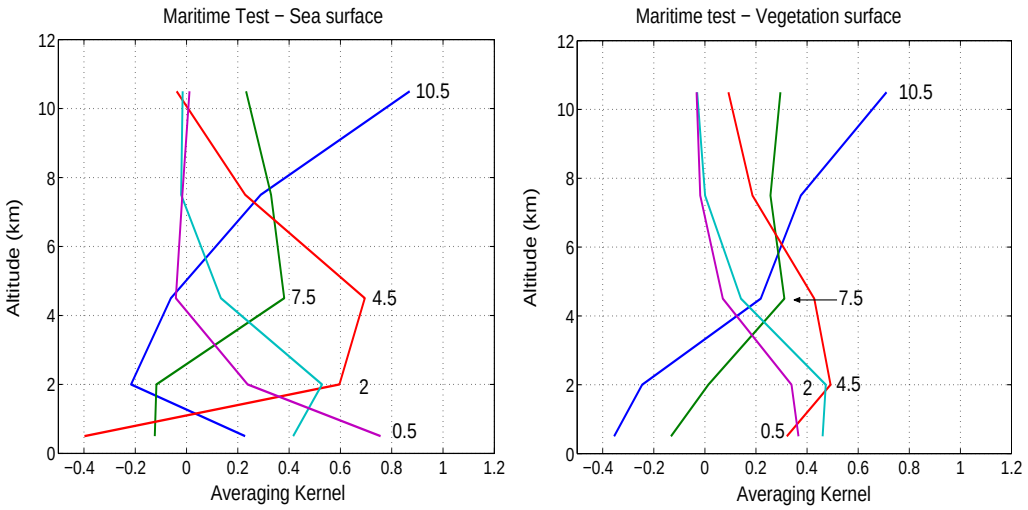

Figure 7.8: Averaging kernels considering Sea and Vegetation surface.

7.3.2 Forward Model errors and Forward Model parameters errors

Figure (7.9) shows the relative change $\Delta x_i/x_i$ in aerosol extinction coefficient profile elements obtained by multiplying the differences by the accurate simulation of the radiance (20 stream) and the simulations made considering

a low number of stream (ΔF) (see Paragraph (6.1.4)) by the contribution function according to (4.27). The Figure (7.9) shows only the lower stream

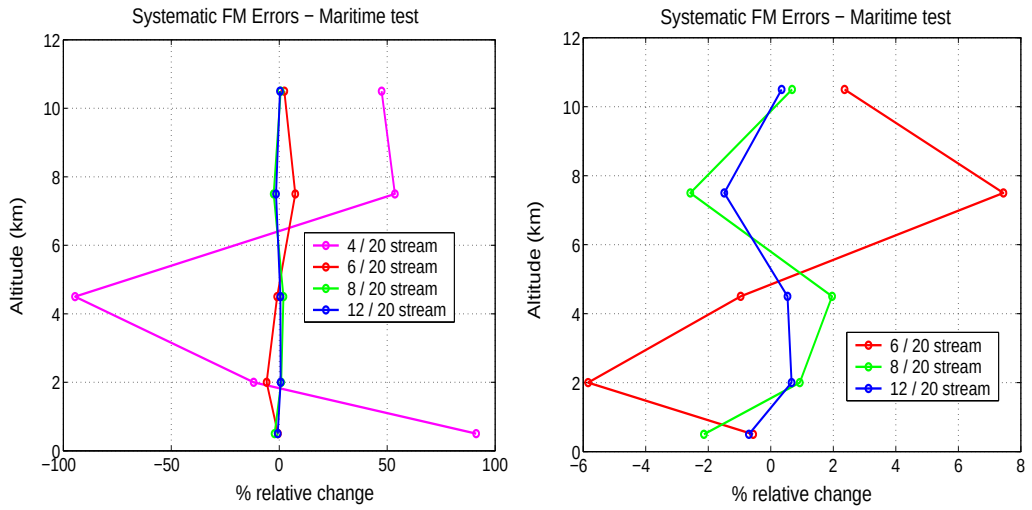

Figure 7.9: Forward model errors on aerosol extinction coefficient profile accuracy (the left picture is the same as right and has been plotted to evidentiate the errors induced by 6, 8 and 12 stream approximations).

approximation (4 stream) generate unacceptable levels of errors, i.e. the 4 stream approximation is not able to represent, with the request accuracy, the behavior of the multiple scattering atmosphere. The *forward model* errors induced by a number of stream greater that 6 is negligible.

The *forward model parameters* errors, computed for *aerosol single scattering albedo*, *aerosol phase function*, *Rayleigh scattering*, *oxygen absorption coefficient* and *surface albedo* and plotted in Figure (7.10), are the square root of the covariances matrix diagonal elements computed using equation (4.26). As Figure (7.10) shows the biggest errors are associated to the uncertainty of the *aerosol phase function* and *aerosol single scattering albedo*. Negligible errors are associated to *Rayleigh scattering*, *oxygen absorption coefficient* and *surface albedo*. In particular the Figure shows that for *aerosol phase function* and *aerosol single scattering albedo*, uncertainties grater than 10% produce errors in the retrieved profile (at some altitudes) bigger than that induce by the sum of the measurement and smoothing error see before (cfr Figure

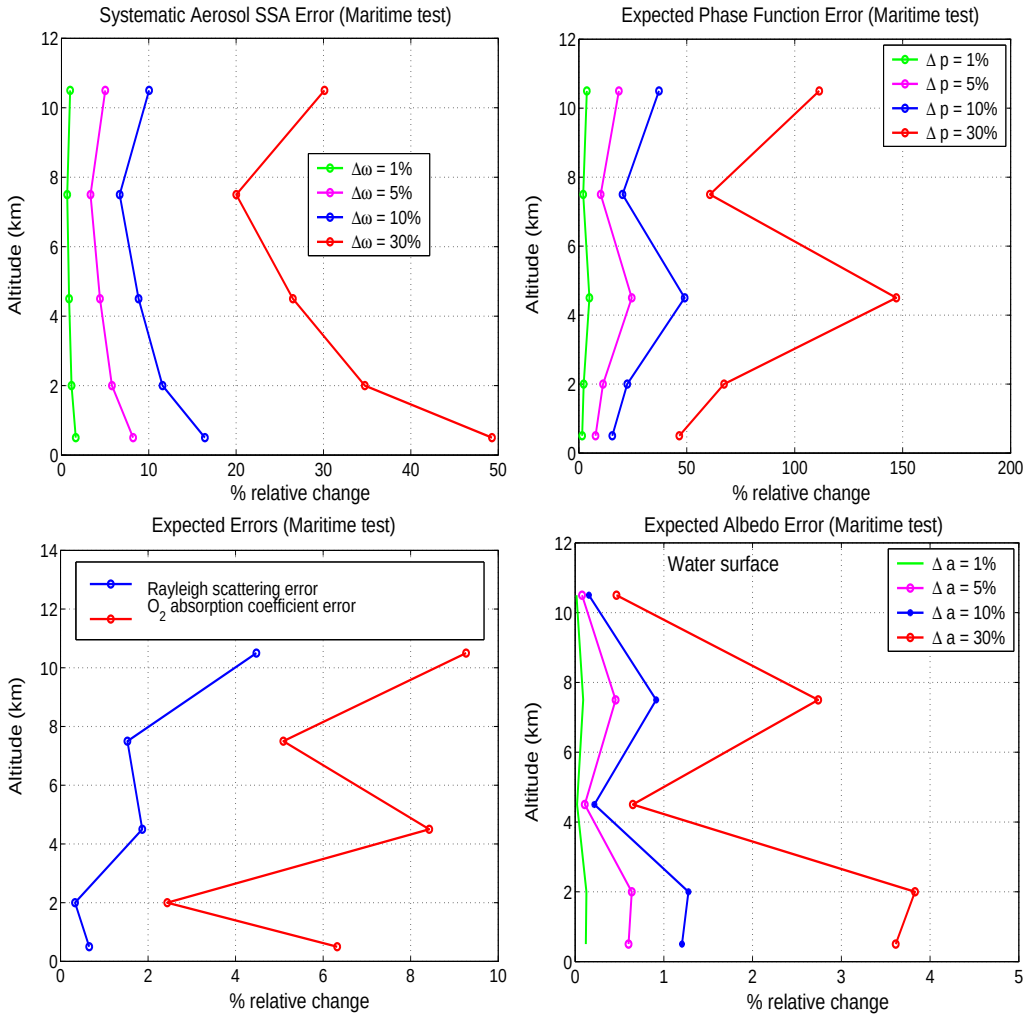

Figure 7.10: Forward model parameters error on aerosol extinction coefficient profile accuracy

(7.1)). The *aerosol phase function* errors, means that the use of the Henyey-Greenstein phase function is greatly advice against, because the difference with the Mie phase function results too high in nearly all the nadir-viewing scattering angle range (see Figure (7.11)). Aerosol optical properties uncertainty greater than 10% makes the retrieval very critic. Thus, a good a-priori optical properties knowledge of the aerosol to be retrieved is needed.

This problem could be resolved introducing a pre-processing phase where the atmospheric window wavelengths will be used to retrieve the aerosol class taking advantage of the different spectral behavior of the different aerosol

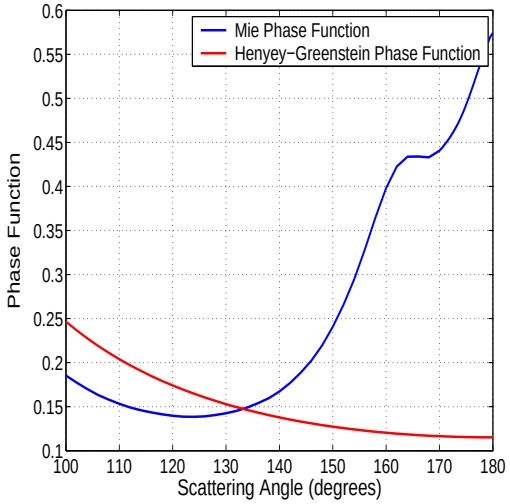

Figure 7.11: Mie and Henyey-Greenstein phase functions plotted in satellite nadir viewing scattering angles range.

class (as seen before). An alghoritm able not only to distinguish the aerosol class but also to give the aerosol optical thickness has been already developed for GOME data [*Guzzi et al.,* 1998, 1999]. Being SCIAMACHY an evolution of GOME with an extended spectral range, the same alghoritm could be used. Thus the a-priori profile AOT could be optimized: it could be scaled in order to match the independently measured AOT or, better saying, the tropospheric aerosol optical depth obtained by differencing the AOT and the aerosol stratospheric optical depth (from limb SCIAMACHY measurements).

Chapter 8

Conclusion

8.1 Problem and Procedure

Aerosols represent one of the greatest areas of uncertainty regarding climate change, both on global and regional scales. The atmospheric aerosol profile retrieval represents one of the main task for the comprehension of its radiative effects. In this work a multiple scattering inversion procedure for the study of the effectiveness of the *aerosol extinction coefficient* profile retrieval and error assessment, considering passive remote sensing instruments, has been developed. The procedure has been applied to the SCIAMACHY nadir simulated measurements considering tropospheric aerosol variation.

The inversion procedure is composed by a *forward model* (AerLIDORT) and an inversion method.
In AerLIDORT (see Chapter (5)), based on LIDORT code for the solution of the radiative transfer equation, the possibility to set a user defined numbers of layers and thickness has been implemented. For each layer, temperature, pressure, molecular and aerosol optical properties has been introduced; the spectral albedo is considered lambertian and different surfaces has been introduced. The aerosol has been described in a precise fashion using the optical properties derived from Levoni [1997] database considering different aerosol class (see Paragraph (5.1.2)). In the model also the aerosol stratification, giving the possibility to select different class of aerosol at different altitudes,

has been implemented. AerLIDORT is able not only to compute the TOA reflectance but also to give the *weighting functions* for many atmospheric parameters essential for the *aerosol extinction coefficient* profile retrieval, sensitivity study and error assessment; so, besides to the *aerosol extinction coefficient weighting functions*, also the *aerosol Mie phase function*, *aerosol single scattering albedo*, *oxygen absorption coefficient* and *Rayleigh scattering coefficient* has been computed.

The *forward model* TOA intensity and *weighting functions* has been validated in both atmospheric windows and oxygen A-band wavelengths, using, respectively, the SCIATRAN RTM (see Paragraph (5.2.2.1)) and the finite-difference *weighting functions* computation (see Paragraph (5.2.2.2)). The validation gives good results either for the TOA intensity comparison than *weighting functions*. The differences with SCIATRAN TOA intensity are less than 0.1% for all the atmospheric windows wavelengths considered and less than 1% for the 95% of wavelengths considered into the oxygen A-band. The percentage difference between the analytical *weighting functions* computed by AerLIDORT and the finite-difference computation are always less than 0.001% for all the altitude considered.

For the iterative inversion scheme, the Gauss-Newton method (see Paragraph (4.5.1)) has been implemented (see Paragraph (5.3)). The iterative inversion procedure is provided by a convergence criterion able to stop the iterations when a particular condition has been satisfied.

8.2 Results

The procedure has been applied to SCIAMACHY nadir simulated measurements considering tropospheric *aerosol extinction coefficient* profile variations. SCIAMACHY has been considered because its wide spectral range gives the possibility to use both the atmospheric windows and oxygen A-band wavelengths and because it has the peculiarity to match limb and nadir measurements. Unfortunately because many problems occur with the SCIA-

MACHY real data calibration, the analysis has been done considering only simulated measurements.

Two cases has been taken as example: a lower and entire tropospheric variation for, respectively, maritime and desertic aerosol. For the two cases the a-priori analysis has been conducted, considering both the atmospheric windows and oxygen A-band wavelengths.

The results shows that in both cases the use of the atmospheric windows wavelengths is not sufficient to resolve the altitude aerosol profile uncertainty. Even if there is an expected improvement of the information content, from the maritime to desertic case, due to the absorption characteristics of the desertic aerosol in the $0.3 - 0.5\ nm$ spectral range, this is not sufficient. The *averaging kernel* is bad characterized (the peaks are poorly defined and no FWHM can be assigned to get an idea of the vertical resolution). The *total retrieval error* (retrieval error considered when the *forward model* and *forward model parameter* error are neglected (see Paragraph (4.3))) is dominated by the *smoothing error* and it's very close to the *a-priori error*, so greater part of the information about the retrieved profile coming from the a-priori instead of the measurements.

The oxygen A-band case is different: the *averaging kernel* curves are more sharply defined, peaks are more distribuited in altitude and it is possible to assign a rough FWHM of 1, 2 and 3 km at the lowest three layer. Also in this case the *total retrieval error* is dominated by the *smoothing error* but it's significantly lesser than the a-priori standard deviation so there is an important quantity of information coming from the measurements. Even if the improvement respect to the *a-priori error* is meaningful, looking at the values of the total percentage errors for the different altitudes, it can be noted that they results quite large. This result shows the need to have an a-priori profile with lesser uncertainty.

The retrieval has been execute for the oxygen A-band for both maritime and desertic case: the retrieved profiles shows a good agreement with the true

profiles and the analysis of the retrieved TOA reflectance reveal the goodness of the inversion procedure.

The same analysis has been applyed by considering higher, than that of SCIAMACHY instrument, spectral resolution in the oxygen A-band to understand its importance in the *aerosol extinction coefficient* profile retrieval. The 0.05 *nm* resolution of the ESFT oxygen database introduced in the *forward model* (see Paragraph (5.1.1.1)) has been considered. The results show a big improvement of the averaging kernel characterization and total errors, so, higher the spectral resolution of measurements is, better the vertical resolution accuracy becomes. The system is now able to resolve in altitude all the layer request.

Another test has been conducted also considering together the atmospheric windows and oxygen A-band wavelengths: the results shows a negligible improvement respect to the only use of oxygen A-band wavelengths.

The sensitivity study reveals the improvement of information content increasing the solar zenith angle (i.e. decresing the scattering angle) and the worsening of the information content increasing the surface albedo. When the surface reflection is significative, the system is not able to distinguish the information comes from the ground from which coming from the aerosol in the lower atmospheric layers.

Finally the complete error assessment has been done. The *forward model* error analysis indicates that the errors induced by a number of stream greater than 6 is negligible. The *forward model parameters* error analysis shows that the main retrieval error comes from the *aerosol phase function* and *aerosol single scattering albedo* uncertainty. The last results indicate that a good a-priori optical properties knowledge of the aerosol to be retrieved is needed. The problem of the improvement of the a-priori profile uncertainty and the knowledge of the aerosol class could be resolved introducing a pre-processing phase based an alghoritm developed for GOME data [*Guzzi et al.,* 1998*,* 2001*; Torricella et al., 1999*] able to istinguish the aerosol class and also to

give the aerosol optical thickness. Thus the a-priori profile AOT could be optimized: it could be scaled in order to match the independently measured AOT or, better saying, the tropospheric aerosol optical depth obtained by differencing the AOT and the aerosol stratospheric optical depth (from limb SCIAMACHY measurements).

This work's improvements and limitations of the aerosol profile retrieval, considering tropospheric aerosol variation for SCIAMACHY nadir simulated measurements, may be summarized as follows:

- the atmospheric windows wavelengths are not able to resolve the aerosol altitude profile uncertainty;

- the use of the oxygen A-band wavelengths (spectral resolution about 0.2 *nm*) gives encouraging results for both cases analyzed (*maritime* and *desertic*). Even if meaningfully quantity of information comes from the measurements a better a-priori profile uncertainty is needed;

- the profile retrieval accuracy is strongly dependent on oxygen A-band spectral resolution. The accuracy improve when the spectral resolution increase;

- the contemporary use of both atmospheric windows and oxygen A-band wavelengths don't give appreciable improvements respect to the only oxygen A-band wavelengths use;

- the sensitivity study conducted into the oxygen A-band reveals the improvement of accuracy increasing SZA, and a worsening accuracy increasing surface albedo;

- the *forward model* errors analysis indicates that the multi-scattering atmosphere could be described with an acceptable degree of accuracy considering 6 or more streams;

- the *forward model parameters* errors analysis shows that the greater error comes from the uncertainty on aerosol optical properties as single scattering albedo and Mie phase function. To reduce such retrieval errors there is the clear need to know the aerosol class before the retrieval will execute.

8.3 Outlook and future work

To generalize the previous considerations for SCIAMACHY nadir measurements, more tests should be done; different aerosol class, stratification and optical thickness must be considered.
When the SCIAMACHY real data will be available, the procedure described will be applyed and tested.
The procedure developed will be also used to define the instrument configuration (view angles, oxygen A-band resolution, mesurement error) able to retrieve with the better accuracy as possible the *aerosol extinction coefficient* profile in the atmosphere.

References

- Ackerman M., Brogniez C., Diallo B.S., Fiocco G., Gobbi P., Herman M., Jager M., Lenoble J., Lippens C., Megie G., Pelon J., Reiter R., Santer R., " *European Validation of SAGE II aerosol profile*", Journal of Geophysical Research Vol. 94, pp. 8399-8411, 1989.

- Anderson G. P., Kneizys F. X., Chetwynd J. H., Wang J., Hoke M. L., Rithman L. S., Kimball L. M., McClatchey R. A., Shettle E. P., Clought S. A., Gallery W. O., Abreu L. W., Selby J. E. A., "*FASCODE/MODTRAN/LOWTRAN: Past/Present/Future*", 18^{th} Annual Review Conference on Atmospheric Transimission Models, 6-8 June, 1995.

- Andreae, M. O. et al. "*External mixture of sea salt, silicates, and excess sulfate in marine aerosols.*", Science Vol. 232, pp 1620-1623, 1986.

- Balis, D., Papayannis, A., Galani, E., Marenco, F., Santacesaria, V., Hamonou, E., Chazette, P., Ziomas, I., and Zerefos, C.: " *Tropospheric Lidar aerosol measurements and sun photometric observations at Thessaloniki, Greece*", Atmospheric Environment, Vol. 34, pp. 925-932, 2000.

- Bates D. R., "*Rayleigh scattering by air*", Planetary Space Science, Vol.32, No.6, pp. 785-790, 1984.

- Bingen C., Fussen D., Vanhellemont F., " *A global climatology of stratospheric aerosol size distribution parameters derived from SAGE II data*

over the period 1984-2000: 2. Reference data ", Journal of Geophysical Research, Vol. 109, No. D6, D06202, 2004 (1).

- Bingen C., Fussen D., Vanhellemont F., " *A global climatology of stratospheric aerosol size distribution parameters derived from SAGE II data over the period 1984-2000: 1. Methodology and climatological observations* ", Journal of Geophysical Research, Vol. 109, No. D6, D06201, 2004 (2).

- Bodaine B. A., Wood N. B., Dutton E. G., Slusser J. R., "*On Rayleigh Optical Depth Calculation*", Journal of Atmospheric and Oceanic Technology, Vol.16, pp. 1854-1861, 1999.

- Bovesmann, H., Burrows, J. P., Buchwitz, M., Frerik, J., Noe, S., Rozanov, V. V., Chance, K. V., and Goede, A., "*SCIAMACHY - mission objectives and measurement modes*", Journal of Atmospheric Science, Vol. 56(2), pp. 127-150, 1999.

- Buchwitz M., Rozanov V., Burrows J. P., "*Development of a correleted-k distribution band model scheme for the radiative transfer program GOMETRAN/SCIATRAN for retrieval of atmospheric costituents from SCIAMACHY/ENVISAT-1 data*", In satellite remote sensing of clouds and the atmosphere III, J. E. Russell, Ed., Vol. 3495, pp 171-186, European Symposium on remote sensing, 21-24 Sept. 1998, Barcelona, Spain.

- Buckwitz M., Rozanov V. V., Burrows J. P., "*A correlated-k distribution scheme for overlapping gases suitable for retrieval of atmospheric constituents from moderate resolution radiance measurements in the visible/near-infrared spectral region*"; Jornal of Geophysical Research, Vol. 105, pp. 15247-15261, 2000.

- Burrows, J. P., Weber, M., Buchwitz, M., Rozanov, V., Ladstatter-Weisenmayer, A., Richter, A., De Beek, R., Hoogen, R., Bramsted,

K., Eichmann, K.-U., Eisinger, M., and Perner, D., "*The Global Ozone Monitoring Experiment (GOME): Mission concept and first scientific results*". Journal of Atmospheric Science Vol. 56(2), pp. 151-175, 1999.

- Cabannes J., "*Sur la diffusion de la lumiéreper les molécules des gaz trasparents*", Ann. Phys., Vol. 15, pp. 5-150, 1921.

- Caudill T. R., Flittner D. E., Herman B. M., Torres O., McPeters R. D., "*Evaluation of the pseudo-spherical approximation for backscattered ultraviolet radiances and ozone retrievals*", Journal of Geophysical Research, Vol. 102, pp. 3881-3890, 1997.

- Chance K. V., Spurr R. J. D., "*Ring effect studies: Rayleigh scattering, including molecular parameters for rotational Raman scattering, and the Fraunhofer spectrum*", Applied Optics, Vol.36, No.21, pp. 5224-5230, 1997.

- Chandrasekhar S., "*Radiative Transfer*", Dover Publications Inc., New York, 1960.

- Charlson R. J., Schwartz S. E., Hales J. M., Cess R. D., Coakley Jr A. J., Hansen J. E., Hofmann D. J., "*Climate forcing by antropogenic aerosol*", Science, Vol. 255, pp. 423-430, 1992.

- Charlson R.J. and Heintzenberg J., "*Aerosol forcing of climate*". John Wiley & Sons, 1995.

- Christopher, S. A., D. V. Kliche, J. Chou, and R. M. Welch: "*First estimates of the radiative forcing of aerosols generated from biomass burning using satellite data*", Journal of Geophysical Research, Vol. 101, pp. 21265 21273, 1996.

- Corradini S., De Smedt I., Soebiyanta V., and Frankenberg C., "*Sensibility Study and Error Assessment of Aerosol Extinction Coefficient*

Profile retrieval from Simulated Limb VIS/IR SCIAMACHY-like data", final presentation Oxford/RAL Spring School in Quantitative Earth Observation, March 2003.

- Dahlback A., Stamnes K., "*A new spherical mode for computing the radiation field available for photolysis and heating at twilight*", Planet Space Science, Vol 39, pp. 671-683, 1991.

- Del Guasta, M.: *Daily cicles in urban aerosols observed in Florence (Italy) by means of an automatic 5321064nm Lidar*, Atmospheric Environment, Vol. 36, pp. 2853-2865, 2002.

- De Tomasi, F. and Perrone, M. R.: "*Lidar measurements of tropospheric water vapor and aerosol profiles over southeastern Italy*", Journal of Geophysical Research, Vol. 108, D9, pp. 10.1029/2002JD002781, 2003.

- Diner, D.J., Beckert, J.C., Bothwell, G.W. and Rodriguez, J.I.: "*Performance of the MISR Instrument During Its First 20 Months in Earth Orbit.*" IEEE Transaction Geoscience and Remote Sensing. Vol. 40 (7), pp. 1449-1466, July, 2002.

- Di Sarra A., Di Iorio T., Cacciani M., Fiocco G., Fu D., "*Saharan dust profiles measured by LIDAR at Lampedusa*", Journal of Geophysical Research, Vol. 106, n. D10, pp. 10335-10347, 2001.

- Duce, R. A., Unni, C. K., Ray, B. J., Prospero, J. M., and Merrill, J. T.: "*Long range transport of soil dust from Asia to tropical North Pacific: Temporal variability*", Science, 209, 15221524, 15, 1980.

- Gabella M., Guzzi R., Kisselev V., Perona G., "*Retrieval of aerosol profile variation in the visible and near infrared: theory and application of the single-scattering approach*", Applied Optics, Vol. 36, n. 6, pp. 1328-1336, 1997.

- Gabella M., Kisselev V., Perona G., "*Retrieval of aerosol profile variation from reflected radiation in the oxygen absorption A band*", Applied Optics, Vol. 38, n. 15, pp. 3190-3195, 1999.

- Gasso, S., Hegg, D. A., Covert, D. S., Collins, D., Noone, K. J., Ostrom, E., Schmid, B., Russell, P. B., Livingston, J. M., Durkee, P. A., and Jonsson, H.: "*Influence of humidity on the aerosol scattering coefficient and its effect on the upwelling radiance during ACE 2*", Tellus, Vol. 52B, pp. 546-567, 2000.

- Gerasopoulos E., Andreae M. O., Zerefos C. S., Andreae T. W., Balis D., Formenti P., Merlet P., Amiridis V., and Papastefanou C., *Climatological aspects of aerosol optical properties in Northern Greece* , Atmospheric Chemisty and Physics, Vol. 3, pp. 20252041, 2003

- Gobbi G. P., "*Lidar estimation of stratospheric aerosol properties: surface, volume and extinction to backscatter ratio*", Journal of Geophysical Research, Vol. 100, pp. 11219-11235, 1995.

- Gobbi G. P., *Polarization lidar returns from aerosols and thin clouds:a framework of the analysis*, Applyed Optics, Vol. 37, pp. 5505-5508, 1998.

- Gobbi G. P., Barnaba F., Giorgi R., Santacasa A., "*Altitude-resolved properties of a Saharan dust event over the Mediterranean*", Atmospheric Environment, Vol. 34, pp. 5119-5127, 2000.

- Gobbi G. P. and Barnaba F., "*The vertical distribution of aerosols, Saharan dust and cirrus clouds at Rome (Italy) in the tear 2001*", Atmospheric Chemistry and Physics Discussions, Vol. 3, pp. 5755-5775, 2003.

- Guzzi R., Burrows J., Cervino M., Levoni., Cattani E., Kurosu T., Torricella T., "*GOME Claud and Aerosol DAta Products Algorithms*

development", ESA Contract 11572/95/NL/CN, 1998.

- Guzzi R., Ballista G., Di Nicolantonio W., "*Retrieval of aerosol profile by the mathematics of inversion in the remote sensing applied to atmosphere where multiple scattering occurs*", IGARSS, 1999.

- Guzzi R., Ballista G., Di Nicolantonio W., Carboni E., "*Aerosol maps from GOME data*", Atmospheric Environment, Vol. 35, pp. 5079-5091, 2001.

- Hansen J., Lacis A., Ruedy R., Sato M., "*Potential climate impact of Mount Pinatubo eruption*", Geophysical Research Letters, Vol. 19, pp. 215-218, 1992.

- Hansen, J., Sato, M. and Ruedy, R. "*Radiative forcing and climate response.*" Journal of Geophysical Research, Vol. 102, pp. 6831-6864, 1997.

- Haywood J. and Shine K.P., "*The effect of anthropogenic sulfate and soot aerosol on the clear sky planetary radiation budget*", Geophysical Research Letteers, Vol. 22, 5, pp. 603-606, 1995.

- Haywood J.M., Ramaswamy V. and Soden B.J., "*Tropospheric aerosol climate forcing in clear-sky satellite observations over the oceans*". Science, Vol. 283, pp. 1299-1303, 1999.

- Haywood J., Boucher O., "*Estimates of the direct and indirect radiative forcing due to tropospheric aerosol: a review*". Reviews of Geophysics, Vol. 38, pp. 513-543, 2000.

- Heidinger A., Stephens G.L., "*Molecular line absorption in a scattering atmosphere. Part II: Application to remote sensing in the O_2 A band*", Journal of the Atmospheric Science, Vol. 57, pp. 1615-1634, 2000.

- Hofmann, D. J.: *Twenty years of balloon-borne tropospheric aerosol measurements at Laramie, Wyoming*, Journal of Geophysical Research, Vol. 98, pp. 12753-12766, 1993.

- Holben B.N., Eck T.F., Slutsker I., Tanre D., Buis J.P., Setzer A., Vermote E., Reagan J.A., Kaufman Y., Nakajima T., Lavenu F., Jankowiak I., Smirnov A., "*AERONET - A federated instrument network and data archive for aerosol characterization*", Remote Sensing Environment, Vol. 66, pp. 1-16, 1998.

- Holben, B. N. et al. *An emerging ground based aerosol climatology: aerosol optical depth from AERONET*, Journal of Geophysical Research, Vol. 106, pp. 12067 12097, 2001.

- IPCC (Intergovernmental Panel on Climate Change) 2001, Ramaswamy,V., Boucher,O., Haigh,J. , Hauglustaine,D., Haywood,J., Myhre,G., Nakajima, T., Shi, G. Y. and Solomon,S., Chapter 6, " *Radiative Forcing of Climate Change*", In: Climate Change 2001, The Scientific Basis, Contribution of Working Group I to the Third Assessment Report of the International Panel on Climate Change, J.T. Houghton et al. (Eds.), pp. 349-416, Cambridge University Press, 2001.

- Jaenicke, R.: " *Nucleation and atmospheric aerosol*", edited by Fukuta, N. and Wagner, P. E., Deepak Publ., Hampton, Virginia, 417, 1992.

- Kaiser J.W., "*Atmospheric Parameter Retrieval from UV-vis-NIR Limb Scattering Measurements*, PhD Thesis, 2001.

- Kaiser J.W., "*Atmospheric Parameter Retrieval from UV-vis-NIR Limb Scattering Measurements*. Logos Verlag, Berlin, Germany. ISBN 3-89722-820-3, 2002.

- Kaiser J.W. and Burrows J.P., "*Fast Weighting Functions for Retrievals from Limb Scattering Measurements.* Journal of Quantitative Spectroscopy and Radiative Transfer, Vol. 77, no. 3, pp. 273-283, 2003.

- Kaufman Y. J., Tanre' D., Remer L. A., Vermote e. f., Chu a., Holben B. N., "*Operational remote sensing of tropospheric aerosol over land from EOS-Moderate Resolution Imaging Spectroradiometer*", Journal of Geophysical Research, Vol. 102, pp. 17051-17067, 1997.

- Kaufman, Y. J. et al. "*The Smoke, Clouds and Radiation experiment in Brazil (SCAR-B).*" Journal of Geophysical Research, Vol. 103, pp. 31783-31808, 1998.

- Kaufman Y.J., Tanre' D., Boucher O., " *A satellite viewe of aerosols in the climate system*", Nature, Vol. 419, pp. 215-223, 2002.

- Kent, G. S., McCormick, M. P., and Schaffner, S. K.: "*Global optical climatology of the free tropospheric aerosol from 1.0 m satellite occultation measurements*", Journal of Geophysical Research, Vol. 96, D3, pp. 5249-5267, 1991.

- Kiehl J. T., Briegleb B.P., " *The relative roles of sulfate and greenhouse gases in climate forcing*", Science, Vol. 260, pp. 311-314, 1993.

- King L. V., "*On the complex anisotropyc molecule in relation to dispersion and scattering of light*", Proceeding Royal Society London, A104, pp. 333-357, 1923.

- King M.D., Kaufman Y., Menzel W. P., Tanre' D., "*Remote sensing of cloud, aerosol and water vapour properties frm the Moderate Resolution Imaging Spectroradiometer (MODIS)*", IEEE Trans. Geoscience Remote Sensing, Vol. 30, pp. 2-27, 1992.

- King M.D., Kaufman Y., Tanre' D., Nakajima T., "*Remote sensing of tropospheric aerosol from space: past, present and future*", Bullettin of the American Meteorological Society, pp. 2229-2259, 1999.

- Kondratyev K., "*Radiation in the atmosphere*", International Geophysics Series, Academic Press, New York and London, 1969.

- Kopper G.A.A., Murtagh D.P., Janson J., "*Aerosol optical Thickness retrieval from GOME data in the Oxygen A-band*", 3rd ERS SYMPOSIUM, Florence, 1997.

- Levoni C., Cattani E., Cervino M., Guzzi R., Di Nicolantonio W., "*Effectiveness of the MS-method for computation of the intensity field reflected by a multi-layer plane parallel atmosphere*", Journal of Quantitative Spectroscopy & Radiative Transfer, Vol. 69, pp. 635-650, 1999.

- Levoni C., Cervino M., Guzzi R., Torricella F., "*Determination of aerosol optical properties: a data base of radiative characteristics for different components and classes*", Applied Optics, Vol.36 (30), pp. 8031-8041, 1997.

- Liao H., Seinfeld J.H., "*Radiative forcing by mineral dust aerosol: sensitivity to key variabiles.*" Journal of Geophysical Research, Vol. 103, pp. 31637-31645, 1998.

- Martonchik, J. V., " *Determination of aerosol optical depth and land surface directional reflectances using multiangle imagery*", Journal of Geophysical Research, Vol. 102, pp. 17015-17022, 1997.

- Martonchik J. V., Diner D. J., Crean K. A., Bull M. A., "*Regional Aerosol Retrieval Result From MISR*", IEEE Transaction on Geoscience and Remote Sensing, Vol. 40, No. 7, pp. 1520-1531, 2002.

- Matthias, V. and Bosenberg, J.: *Aerosol climatology for the planetary boundary layer derived from regular lidar measurements*, Atmospheric

Research, 63, 221245, 2002.

- Mishchenko M.I., Geogdzhayev I.V., Cairns B., Rossow W.B. and Lancis A.A, "*Aerosol retrievals over the ocean by use of channels 1 and 2 AVHRR data: sensitivity analysis and preliminary results*", Applied Optics, Vol 38, No. 36, pp 7325-7341, 1999.

- Moulin, C., Lambert, C. E., Dayan, U., Masson, V., Ramonet, M., Bousquet, P., Legrand, M., Balkanski, Y. J., Guelle, W., Marticorena, B., Bergametti, G., and Dulac, F.: "*Satellite climatology of African dust transport in the Mediterranean atmosphere*", Journal of Geophysical Research, Vol. 103, 13137-13144, 1998.

- Muller, D., Mattis, I., Wandinger, U., Ansmann, A., and Althausen, D.: "*Saharan dust over a central European EARLINET-AERONET site: Combined observations with Raman lidar and sun photometer*", Journal of Geophysical Research, Vol. 108, D12, 4345, 10.1029/2002JD002918, 2003.

- Murayama, T., Sugimoto, N., Uno, I., Kinoshita, K., Aoki, K., Hagiwara, N., Liu, Z., Matsui, I., Sakai, T., Shibata, T., Arao, K., Sohn, B., Won, J., Yoon, S., Li, T., Zhou, J., Hu, H., Abo, M., Iokibe, K., Koga, R., and Iwasaka, Y.: "*Ground-based network observation of Asian dust 30 events of April 1998 in east Asia*", Journal of Geophysical Research, Vol. 106, D16, pp. 18345-18360, 2001.

- Nakajima T., Tanaka M., "*Alghoritms for radiative transfer intensity calculations im moderately thick atmospheres using a truncation approximation*", Journal of Quantitative Spectroscopy & Radiative Transfer, Vol. 40, pp. 51-69, 1988.

- O'Brien D.M., English S.A., Da Costa G., "*High-precision, high-resolution measurements of absorption in the oxygen A-band*", Journal of Atmo-

spheric and Oceanic Technology, Boston, vol. 14, no. 1, pp. 105-119, 1997.

- Penner, J. E., Andreae, M., Annegarn, H., Barrie, L., Feichter, J., Hegg, D., Jayaraman, A., Leaitch, R., Murphy, D., Nganga, J., and Pitari, G.: *Aerosols, their Direct and Indirect Effects, 5768 in Climate Change 2001: The Scientific Basis*, Cambridge University Press, Cambridge, UK, 2001.

- Prospero, J. M., Glaccum, R. A., and Nees, R. T.: "*Atmospheric transport of soil dust from Africa to South America*", Nature, Vol. 289, pp. 570-572, 1983.

- Prospero, J. M. and Nees, R. T. "*Impact of the North African drought and El Nio on mineral dust in the Barbados trade wind*", Nature, Vol., 320, pp. 735-738, 1986.

- Prospero, J. M. "*Long term measurements of the transport of African mineral dust to the Southern US: implications for regional air quality.*" Journal of Geophysical Research, Vol. 104, pp. 15917-15927, 1999.

- Prospero, J. M., Ginoux, P., Torres, O., Nicholson, S. E., and Gill, T. E.: "*Environmental char- 5 acterization of global sources of atmospheric soil dust identified with the Nimbus 7 total ozone mapping spectrometer (TOMS) absorbing aerosol product*", Rev. Geophys., 40, 1, 1002, doi:10.1029/2000RG000095, 2002.

- Ramanathan, V. et al.: "*Aerosol, climate, and the hydrological cycle*", Science, Vol. 294, pp. 2119-2124, 2001 (1).

- Ramanathan, V. et al. "*The Indian Ocean Experiment: an integrated analysis of the climate forcing and effects of the great Indo-Asian haze*", Journal of Geophysical Research, Vol. 106, pp. 28371-28398, 2001 (2).

- Rizzi R., Guzzi R., Legnani R., "*Aerosol size spectra from spectral extinction data: the use of a linear inversion method*", Applied Optics, Vol. 21, pp. 1578-1587, 1982.

- Rodgers C.D., "*Characterization and error analysis of profiles retrieved from remote sounding experiments*", Journal of Geophysical Research, Vol. 95, 5587, 1990.

- Rodgers C.D., "*Inverse methods for atmospheric sounding*", World Scientific Publishing Pte LTd, New York, 2000.

- Rothman, L. S., Rinsland, C. P., Goldman, A., Massie, S. T., Edwards, D. P., Flaud, J.-M., Perrin, A., Camy-Peyret, C., Dana, V., Mandin, J.-Y., Schroeder, J., Mccann, A., Gamache, R. R., Wattson, R. B., Yoshino, K., Chance, K. V., Jucks, K. W., Brown, L. R., Nemtchinov, V., and Varanasi, P., "*The HITRAN molecular spectroscopic database and HAWKS (HITRAN atmospheric workstation): 1996 edition*", Journal of Quantitatuve Spectroscopy and Radiative Transfer, Vol. 60(5), pp. 665-710, 1998.

- Rozanov V. V., Diebel D., Spurr R.J.D., Burrows J.P., "*GOMETRAN: A radiative transfer model for the satellite project GOME - the plane parallel version*", Journal of Geophysical Research, Vol. 102, pp. 16683-16695, 1997.

- Rozanov V. V., Kurosu T., Burrows J., "*Retrieval of atmospheric constituents in the UV/visible: A new quasi- analytical approach for the calculation of weighting functions*", Journal of Quantitative Spectroscopy & Radiative Transfer, Vol. 60, pp. 277-299, 1998.

- Rozanov A. V., Rozanov V. V., Burrows J., "*Combined differential-integral approach for the radiation field computation in a spherical shell atmosphere: Nonlimb geometry*", Journal of Geophysical Research, Vol. 105, pp. 22937-22942, 2000.

- Russell P.B. and Heintzenberg J., "*An overview of the ACE-2 Clear Sky Column Closure Experiment (CLEARCOLUMN)*", Tellus,B, Vol. 52, pp. 463-483, 2000.

- Sakai, T., Shibata, T., Kwon, S., Kim, Y., Tamura, K., and Iwasaka, Y.: "*Free tropospheric aerosol backscatter, depolarization ratio, and relative humidity measured with the Raman lidar at Nagoya in 1994-1997: contributions of aerosols from the Asian continent and the Pacific ocean*", Atmospheric Environment, Vol. 34, pp. 431-442, 2000.

- Sassen, K: "*Indirect climate forcing over the western US from Asian dust storms*", Geophysical Research Letters, 29, 10, 10.1029/2001GL014051, 2002.

- Schimpf B., Schreier F., "*Robust and efficient inversion of vertical sounding atmospheric high-resolution spectra by means of regularization*", Journal of Geophysical Research, Vol. 102, No. D13, pp. 16037-16055, 1997.

- Schneider, J. and Eixmann, R.: "*Three years of routine Raman lidar measurements of tropospheric aerosols: Backscattering, extinction and residual layer height*", Atmospheric Chemistry and Physics, Vol. 2, pp. 313-323, 2002.

- Schwartz S. E. and Co-authors, "*Connection between aerosol properties and climate*", R. J. Charlson and J. Heintzenberg, Eds., John Wiley and Sons, 251-280, 1995.

- Shannon C. E. and Weaver W., (1949) "*The Mathemtical Theory of Communication*" Paperback edition, University of Illinois Press, Urbana, 1962

- Smirnov A., Holben B.N., Savoie D., Prospero J.M., Kaufman Y.J., Tanre D., "*Relationship between column aerosol optical thickness and*

in situ ground based dust concentrations over Barbados, Geophysical Research Letters, Vol. 27, no. 11, pp. 1643-1646, 2000.

- Spurr R.J.D., "*Linearized radiative transfer theory*", PhD Thesis, 2001.

- Stamnes K., Tsay S. C., Wiscombe W., Jayaweera K, "*Numerically stable algorithm for discrete ordinate method radiative transfer in multiple scattering and emitting layered media*", Applied Optics, Vol. 27, pp. 2502-2509,1988.

- Thomas G. E. and Stamnes K., "*Radiative Transfer in the Atmosphere and Ocean*", Cambridge University Press, 1999.

- Thomas G. E., Stamnes K., "*Radiative Transfer in the Atmosphere and Ocean*", Cambridge University Press, 1st edition, 1999.

- Thomason, LW, Taha, G, "*SAGE III aerosol extinction measurements: Initial results*" Geophys. Res. Lett., Vol. 30, no. 12, 2003.

- Torres O., P.K. Bhartia, J.R. Herman and Z. Ahmad, "*Derivation of aerosol properties from satellite measurements of backscattered ultraviolet radiation. Theoretical Basis*", Journal of Geophysical Research, Vol. 103, pp.17099-17110, 1998.

- Torres, O., P.K. Bhartia ,J.R. Herman, A. Sinyuk and B. Holben, "*A long term record of aerosol optical thickness from TOMS observations and comparison to AERONET measurements*", Journal of Atmospheric Science, Vol. 59, pp. 398-413, 2002.

- Torricella F., Cattani E., Cervino M., Guzzi R., Levoni C., "*Retrieval of aerosol properties over ocean using GOME measurements: method and applications to test cases*", Journal of Geophysical Research, Vol. 104, pp. 12085-12098, 1999.

- Von Hoyningen-Huene W., Freitag M., Burrows J.B. "*Retrieval of aerosol optical thickness over land surfaces from top-of-atmosphere radiance*", Journal of Geophysical Research, Vol. D9 108, p. 4260, 2003.

- Wiscombe W.J., "*The delta-M method: rapid yet accurate radiative flux calculations for strongly asymmetric phase functions*", Journal of Atmospheric Science, Vol. 34, pp. 1408-1422, 1977.

Acknowledgement

I would like to thank Prof. Renato Santangelo (University of Modena), Prof. Rodolfo Guzzi (ASI), Dott. Walter Di Nicolantonio (ISAC-CNR Bologna) and the ISAC-CNR ARS team (Giovanni, Stefano, Carole and Enrico) that gives me the opportunity to realize this work.

Prof. Massimo Carlotti (University of Bologna) and Dr. Bianca Dinelli (ISAC-CNR Bologna) for the basic scientific discussions about Optimal Estimation. Dr. Chiara Piccolo (Oxford University) for her friendship and the explanatory discussions about inversion methods and life.

Dr. Gian Paolo Gobbi (ISAC-CNR Rome) and Dr. Pugnaghi Sergio (University of Modena) for the provided input data used in this thesis and Luigi Liberti (ISAC-CNR Rome) for the very useful scientific discussions about aerosols.

A particular thank to Simone Cristofori and Elisa Carboni, PhD companions and promising young physicists, with which I shared joins and pains of the period spent at CNR.

A very special thank to Dr. Marco Cervino (ISAC-CNR Bologna) for his great scientific support and friendship, basic for the thesis realization.

Another special thank to "*Scienziate/i Responsabili*" [1] group with which I shared a different way of thinking and making science.

Last but not least a great thank to Federica, my lifemate, that is still able to support and belive in me.

[1] *http://www.bo.cnr.it/www-sciresp*